LOCATION PERFORMANCE OF SEISMIC NETWORKS BY A NUMERICAL SIMULATION: APPLICATION TO BU-KOERI (TURKEY)

by

Pelin Pündük

B.S., Geophysics Engineering, Çanakkale Onsekiz Mart University, 2007

Submitted to the Kandilli Observatory and Earthquake Research Institute in partial fulfillment of the requirements for the degree of Master of Science

Graduate Program in Geophysics

Boğaziçi University

2011

LOCATION PERFORMANCE OF SEISMIC NETWORKS BY A NUMERICAL SIMULATION: APPLICATION TO BU-KOERI (TURKEY)

APPROVED BY:

Assoc. Prof. Nurcan Meral Özel (Thesis Supervisor)	……...……
Prof. Hayrullah Karabulut	……
Prof. Ali Pınar (Istanbul University)	……

DATE OF APPROVAL: 13.06.2011

ACKNOWLEDGEMENTS

I would like to express my sincere gratitude to my dear advisor, Prof. Dr. Nurcan Meral Özel who accepted me to prepare this M. Sc. Thesis, supported, encouraged, showed patience and gave valuable comments to construct this thesis. I also stated my sincere thanks to Prof. Dr. Hayrullah Karabulut for his precious advices to my thesis.

I am very grateful to Antonino D'Alessandro for introducing me the scientific aspects of the study.

I would like to extend my sincere thanks to Ayşegül Küsmezer and Musavver Didem Samut Cambaz for providing me scientific information about this study and to Doğan Kalafat, Kıvanç Kekovalı, Selda Altuncu and Mustafa Çomoğlu for data collection.

I would like to thank my dear friends Yasemin Korkusuz, Öcal Necmioğlu and Melis Cevatoğlu for their technical supports.

I thank to my special colleague Nilay Başarır and to all friends at Geophysics Department in Kandilli Observatory and Earthquake Research Institute. I would also like to extend my deepest and sincere thanks to Can Seran Ayana for his supports, encouragements and motivations.

Finally, i am grateful to my parents for their endless patience and supports during my thesis and my life.

ABSTRACT

LOCATION PERFORMANCE OF SEISMIC NETWORKS BY NUMERICAL A SIMULATION: APPLICATION TO BU-KOERI (Turkey)

The main function of a seismic network is to provide high quality data for monitoring seismic zones and seismic hazard analysis. In this study, a numerical simulation (SNES, Seismic Network Evaluation through Simulation) technique is utilized for the evaluation of hypocenter location performance of a seismic network. The SNES method gives, as a function of magnitude, hypocentral depth and confidence level, the spatial distribution of the number of active stations in the location routine and their relative azimuthal gaps along with confidence intervals in hypocentral parameters concerning both the geometry of the seismic network and the use of an insufficient velocity model. The application of the SNES method also permits the evaluation of the magnitude of completeness (Mc), the background noise levels at the stations and assessment of appropriateness of the velocity model used in location routine. The SNES method does not take into account location due to systematic model error, so it allows estimating only the precision of the hypocentral location.

In this study, SNES method is applied to the BU-KOERI (Boğaziçi University - Kandilli Observatory Earthquake Research Institute) seismic network to evaluate and quantify its performance for locating local and regional seismicity. This application has allowed to identify the background noise levels of the KOERI seismic stations and to evaluate the goodness of the velocity model used in the location routine. Furthermore, the SNES method has allowed identifying some seismogenic areas on the national territory that are currently not enough covered instrumentally. The upgrading of the network in these areas could be optimized using the SNES technique.

For each station, a large number of three-hour waveform segments during a 6 year period were selected from continuous digital seismic data. Each year was divided into four seasons and one month represents each season (Winter, Spring, Summer and Fall were represented by January, April, July and October, respectively). Five different days and nights were also picked in each month (day times were preferred from 5 a.m. to 5 p.m. and night times from 5 p.m. to 5 a.m.). For each five nights and five days of a month, the acceleration PSD curves of the vertical component of the noise were generated, related to the period 2005-2010. Then the Turkish territory was gridded with 5 km distances and the mean PSD values (in the frequency range between 1-12 Hz) were assigned to the intersection points of each 5 km distances. The variance and the residual times of P and S phases were determined to evaluate the appropriateness of the velocity model used by BU-KOERI. Hereafter, seismic spectra calculation was obtained to evaluate the detection capability of the seismic network.

Finally, the earthquake simulation was made by constructing the SNES maps for magnitudes of 2.5, 3.0, 3.5, fixing the hypocentral depth at 10 km and the confidence level at 95 per cent. Through the application of the SNES method, it is showed that the KOERI provides the best monitoring coverage in the southeast of Marmara Sea and Gulf of Gökova with maximum number of twelve stations, for M_L 2.5, with errors that are 3 km and 5.5 km for epicenter and hypocentral depth, respectively. At M_L 3.0, BU-KOERI seismic network gives the best quality of the epicentral estimate with a maximum number of twenty stations in Marmara Region with errors that are 2 and 4 km for epicenter and hypocentral depth, respectively. At M_L 3.5, the seismic network provides the best monitoring coverage in the mid part of Marmara Sea and some south parts of it where the errors in epicentral and hypocentral estimate are 2 km and 3 km, respectively, with at least 28 seismic stations. This seismic network also provides a threshold of completeness down to M_L 3.0 for almost all Turkish territory.

As a result, location performance of BU-KOERI seismic network should be improved by installing more seismic stations on the Turkish territory where the coverage of the stations is insufficient. In addition, with the construction of OBSs, the location performance of the network is expected to be enhanced.

ÖZET

SAYISAL SİMÜLASYON YÖNTEMİ İLE BU-KRDAE (BOĞAZİÇİ ÜNİVERSİTESİ KANDİLLİ RASATHANESİ DEPREM ARAŞTIRMA ENSTİTÜSÜ) SİSMİK AĞININ PERFORMANS DEĞERLENDİRMESİ

Deprem bölgelerinin belirlenmesi ve deprem tehlike analizlerinin yapılabilmesi için, bir sismik ağın temel işlevi, yüksek kalitede veri sağlamaktır. Bu çalışmada, bir sismik ağın hangi kalitede deprem lokasyonlarını belirlediğini saptayabilmek için SNES (Simülasyon yolu ile bir sismik ağın değerlendirilmesi) metodu kullanılmıştır. Bu metotta depremin büyüklüğü, derinliği ve güven aralığı belirlendikten sonra sismik istasyonların dağılımına ve kullanılan kabuk hız modeline bağlı olarak lokasyon işleminde aktif olan istasyonların sayısı, dağılımı ve azimut açıları belirlenmektedir. SNES metodu aynı zamanda, istasyonların ölçebileceği en küçük deprem büyüklüklerini, istasyonların gürültü seviyelerini ve lokasyon işleminde kullanılan kabuk hız modelinin uygunluğunu da ortaya çıkararak hiposantr lokasyonlarının doğruluğunu saptmaktadır.

BU-KRDAE sismik istasyonlarına uygulanan bu yöntem, sismik ağın, yerel ve bölgesel depremlerin yerlerinin belirlenmesindeki performansını, sismik istasyonların gürültü seviyelerini ve lokasyon işleminde kullanılan kabuk hız modelinin uygunluğunu değerlendirmektedir. Ayrıca, bu yöntem, istasyonlar tarafından yeterli ölçüde kapsanamayan depremsel alanların belirlenmesini sağlar.

Bu çalışmada, 2005-2010 yılları arasındaki sismik kayıtlar kullanılmıştır. Her yıl dört mevsime, her mevsimi bir ay temsil edecek şekilde, her bir istasyon için, gece ve gündüz saatleri olmak üzere (gündüz saatleri için 05:00-17:00, gece saatleri için 17:00-05.00) beş günlük üç saatlik gürültü verileri tespit edilmiştir (Kış, İlkbahar, Yaz ve Sonbahar mevsimleri için Ocak, Nisan, Temmuz ve Ekim ayları seçilmiştir). Her istasyonun gece ve gündüz saatleri için ise, ivme gürültü spektrumları oluşturulmuştur.

Daha sonra, Türkiye enine ve boyuna 5 km aralıklarla bölünerek, her bir aralığın kesişme noktasına 1-12 Hz frekans aralığındaki gürültü spektrumları atanmıştır. BU-KRDAE tarafından kullanılan kabuk hız modelinin uygunluğunu saptayabilmek için P ve S fazlarının varyansları ve residüelleri hesaplanmıştır. Sismik ağın depremleri ölçme kapasitesini değerlendirmek için ise sismik spektrumlar hesaplanmıştır.

Son olarak, hiposantr derinliği 10 km, güven aralığı yüzde 95 alınarak 2.5, 3.0 ve 3.5 büyüklüğünde deprem simülasyonu yapılmıştır ve SNES haritaları oluşturulmuştur. SNES metodunun uygulanmasıyla, BU-KRDAE sismik ağının, deprem izlemelerini en iyi Marmara Bölgesi'nde, en çok on iki tane istasyon ile yaptığı tespit edilmiştir. M_L 2.5 büyüklüğündeki depremler için, minimum episantr hatası 3 km ve minimum hiposantr hatası 5.5 km olarak belirlenmiştir. Bu sismik ağın, M_L 3.0 büyüklüğündeki depremler için, yine en iyi Marmara Bölgesi'nde, en çok yirmi istasyonla, episantr tahminlerini en az 2 km hata ile ve hiposantr derinliğini en az 4 km hata ile belirlediği gözlemlenmiştir. M_L 3.5 büyüklüğündeki depremler için ise BU-KRDAE, deprem izlemelerini en iyi Marmara Denizi'nin orta kısımlarında ve bazı güney bölgelerinde, en az 28 istasyonla, minimum 2 km episantr ve minimum 3 km hipsantr hatasıyla yürüttüğü gözlemlenmiştir.

Sonuç olarak, BU-KRDAE sismik ağının lokasyon performansı, istasyonların yetersiz olduğu alanlara, daha çok istasyon kurarak geliştirilebilir. Bununla birlikte, deniz dibi istasyonlarının kurulması sismik ağın performansının geliştirilmesine katkı sağlaması beklenmektedir.

TABLE OF CONTENTS

LIST OF FIGURES

LIST OF TABLES

LIST OF SYMBOLS / ABBREVIATIONS

α	Radius of the source
Δ	Epicentral distance
γ	Damping constant for high frequencies
ω	Angular frequency
ω_o	Corner frequency
ρ	Density of the medium
δ	Near surface attenuation
λ_1	Angle of reflected S wave
λ_2	Angle of refracted S wave
$\Delta\sigma$	Stress drop
ΔT	Residual travel times of the seismic phases
$\varphi(\omega)$	Phase spectrum
θ_1	Angle of reflected P wave
θ_2	Angle of refracted P wave
σ^2_P	Variance in the residual times of the P phases
σ^2_S	Variance in the residual times of the S phase
$\sigma^2_{\Delta T}$	Variance of the residual times
σ^2_{par}	Variance of the generic focal parameter
σ^2_{MOD}	Variance of the velocity model used
σ_T, σ_x, σ_y, σ_z	Associated uncertainties of the hypocenter parameters
A_0	Amplitude of the seismic wave
A_1	Amplitude of reflected P wave
A_2	Amplitude of refracted P wave
b	Exponent that displays the variation of the frequencies in attenuation phenomena
B_1	Amplitude of reflected S wave
B_2	Amplitude of refracted S wave
c	Velocity of the body wave
c_i	Velocity of the seismic wave in the layer
C_d	Covariance matrix

G^{-g}	Generalized inverse matrix
i	Incidence angle of the body wave
p	Ray parameter
Q_0	Quality factor
Q_p	P wave attenuation
r	Hypocentral distance
r_1, r_2, r_3	Semiaxes of the confidence ellipsoid
r_{par}	Generic focal parameter
R_p	Mean square value of the directivity function of the source
t_k	Travel time of the ray
T_{cal}	The calculated travel time
T_{obs}	The time read on the seismogram
x_k	Length of the ray
x_0, y_0, z_0	Hypocentral coordinates of an earthquake

1D	One dimensional
2D	Two dimensional
ADC	Analog-to-digital converter
BB	Broadband seismometer
BTZ	Bitlis Thrust Zone
BU	Boğaziçi University
cm	centimeter
cos	cosinus
dB	decibel
deg	degree
EAFZ	East Anatolian Fault Zone
f	Frequency
FFT	Fast Fourier transform
g	Acceleration due to Earth's gravity
GMT	Greenwich Mean Time
H	Hypocentral depth
Hz	hertz

NMSOP	New Manual of Seismological Observatory Practice
IRIS	Incorporated Research Institutions for Seismology
km	kilometer
KOERI	Kandilli Observatory and Earthquake Research Institute
Lat	Latitude
Log	Logarithm
Lon	Longitude
LTA	Long-term average
m	meter
M_0	Scalar seismic moment
Mc	Magnitude of completeness
MD	Duration magnitude
M_L	Local magnitude
M_s	Surface wave magnitude
MHz	megahertz
MPa	megapascal
NAFZ	North Anatolian Fault Zone
NEAFZ	North East Anatolian Fault Zone
NEMC	National Earthquake Monitoring Center
OBS	Ocean-bottom seismometer
ORFEUS	Observations and Research Facilities for European Seismology
PGA	Peak ground acceleration
PSD	Power spectral density
PSD_E	Power spectra of the theoretical P phase
PMC	Probability-based Magnitude of Completeness method
rad	radian
RES	Radius of equivalent sphere
s	second
SP	Short-periodseismometer
sin	sinus
SNR	Signal to noise ratio
STA	Short-term average

SNES	Seismic network evaluation through simulation method
t	time
T_0	Origin time of an earthquake
USGS	United States Geological Survey
Vp	P wave velocity
Vs	S wave velocity
VBB	Very broadband seismometer
WSR	Wideband spectral ratio
WAGC	West Anatolian Graben Complexes

1. INTRODUCTION

Seismic networks are important tools for understanding active tectonic processes in a monitored region. Their numerous applications from monitoring seismicity to characterizing seismogenic volumes make seismic networks essential tools for assessing seismic hazard in active regions. An appropriately configured seismic network is also a valuable tool for the study of deep geological structures using seismic tomography. The ability to detect small and medium size events requires a seismic network with a sufficient number of optimally distributed low-noise stations. It is important to assess existing network capabilities, to identify seismogenic areas that are not adequately covered, and to quantify measures that will allow network improvement (D'Alessonrdo *et al.,* 2001).

Turkey is one of the most seismically active regions in the world and lies within the Mediterranean part of Alpine-Himalayan Orogenic system. This system reaches out for east-west direction from Asia to the Mediterranean. The Alpine Orogeny was produced by the Europe-Africa collision, while the Himalayan Orogeny has emerged from the compressional motion between India and Asia. Turkey is surrounded by three major plates which are African, Eurasian, and Arabian Plates. The most substantial tectonic environments in Turkey are the Aegean Arc, the West Anatolian Graben Complexes (WAGC), the North Anatolian Fault Zone (NAFZ), the East Anatolian Fault Zone (EAFZ), the North East Anatolian Fault Zone (NEAFZ) the Bitlis Thrust Zone (BTZ) and the Caucasus (Bayrak *et al.,* 2008). The Aegean arc system plays an important role in the geodynamical evolution of the Aegean region. Convergence between the African and Anatolian Plates in the Eastern Mediterranean takes place by subduction along the Aegean and Cyprus arcs (McKenzie, 1978; Papazachos and Comninakis, 1971). The African Plate is descending northward beneath the Anatolian Plate. NAFZ is one of the best known strike-slip faults in the world because of its extraordinary seismic activity, unusually well developed surface expression and significance for the tectonics of eastern Mediterranean region (Şengör *et al.,* 1985). EAFZ is a transform fault forming parts of boundaries between the Anatolian and the Arabian Plates (Tüysüz, 2005). It is regarded as a conjunction of the NAFZ. The Bitlis Thrust Zone is a complex continent-continent and continent-ocean collision boundary which lies north of fold-and-thrust belt of the Arabian

Plate and stretches from southeastern Turkey to the Zagros Mountains in Iran (Şengör, 1979; Hempton, 1985). The northeast part of the Turkish Plate, the movement is hold by thrust faults connected with the Caucasus. The result of this motion is the thickening of the continent which means the elevation of the Caucasus (Bayrak *et al.,* 2008).

Because of the multiple plate boundaries, large magnitude events are common in Turkey. Turkey rates high among the countries which have suffered many losses of life and property due to the earthquakes. In the last century, many destructive earthquakes have occurred in Turkey: Murefte M_s = 7.3, 1912 (216 deaths), Erzincan M_s = 7.9, 1939 (32968 deaths), Gediz M_s = 7.2, 1970 (1086 deaths), Kocaeli M_s = 7.8, 1999 (17480 deaths), Düzce M_s = 7.5, 1999 (763 deaths) (BU-KOERI-National Earthquake Monitoring Center).

In order to resolve the earthquakes, Turkey is monitored by BU-KOERI seismic stations. Kandilli Observatory has been serving since 1863. In the 1970s, the observatory organized with Space Science Department and Earth Science Department. After the destructive Istanbul Earthquake of 1894, KOERI (formerly known as Rasathane-i Amire-i Alaimül-cev) purchased its first two seismographs from Italy (KOERI, 2011). In recent years, KOERI has been technologically renovated and seismic stations are controlled by NEMC (National Earthquake Monitoring Center). KOERI has now reached a configuration of 158 seismic stations with 117 three-component wideband frequency sensors.

Satake (1985) investigated that the station coverage causes many effects on focal mechanism on moment tensor inversion. For this reason, he indicated a uniform station distribution of the global seismograph network was desirable.

Rabinowitz and Steinberg (1990) provided a statistical approach to the station siting problem to find out the optimal configuration of a seismograph network.

Kristekova and Skacikova (1997) used some cluster of stations from Central Europe to determine their detection capabilities for four intervals of epicentral distances.

The difference in magnitude between the detection thresholds showed the accuracy of seismic stations with their detection capabilities.

Wüster *et al.* (2000), studied on evaluation of the detection and location capabilities of an experimental global seismic monitoring system. They evaluated seismological performance by statistically and then used network simulation codes which allowed to interpolate system capabilities over aseismic regions and to extrapolate them for the capabilities of the future seismic network.

Seggern (2004) analyzed the seismic background noise and detection threshold in a seismic network by comparing predicted seismic thresholds to actual thresholds. He used statistical properties of noise and related them to the long-term average (LTA) and short-term average (STA) which are used in algorithms, and then he combined these attributes with a random earthquake simulator for predicting the seismic threshold of the network for a given area.

McNamara and Buland (2003), characterized the background seismic noise across the continental United States, by estimating power spectral densities (PSDs) at broadband seismic stations for evaluating performance or those seismic stations. They explained that it should be relevant to the future siting of the national seismic network and that the noise maps at body wave frequencies should be useful for estimating magnitude threshold for the backbone and regional networks or for optimizing the distribution of regional network stations.

Gentili *et al.* (2011), examined detection probabilities and recording completeness of the seismic network in northern Italy, using the Probability-based Magnitude of Completeness (PMC) method by Schorlemmer and Woessner (2008). They showed that the completeness maps are useful for considering the seismicity studies.

In this study, seismic network evaluation through simulation (SNES) method was applied to the KOERI seismic stations to assess background noise levels and velocity model appropriateness, to evaluate the hypocenter location uncertainty, and to determine the magnitude of completeness (Mc) with the actual seismic network configuration. Not

only allows the technique quantifying the location performance of the KOERI stations but also it identifies some seismogenic areas in Turkey that are covered inadequately. It should also be convenient for the future siting of KOERI backbone stations. Moreover, KOERI also planned an offshore extension of the seismic network with the deployment of a group of ocean-bottom seismometers with hydrophones. These upgraded monitoring capabilities will meet the performance goals established by KOERI.

First chapter gives briefly information about the importance of seismic networks, tectonics of and seismicity in Turkey, history of BU-KOERI, the method used in the study and its importance on seismic stations, on their performance and their capability of performing qualified hypocenter locations. The descriptions of seismic networks, seismic signals, seismic noise and M_c (magnitude of completeness) are explained in second chapter. The SNES method and its sub-methods are described in third part. Data collection is given fourth part. Data analysis is explained in details in the fifth chapter of the thesis. Finally, the results and conclusion parts are given in last two chapters.

2. DEFINITIONS OF SEISMIC NETWORKS, SEISMIC SIGNALS, SEISMIC NOISE AND MAGNITUDE OF COMPLETENESS (M_c)

2.1. Seismic Networks

There were only single seismic station before 1960. Each station made its own survey that sent to a central location. If many stations operate in a country, all of them can be called a "network". Seismic networks started to operate in the 1960s. These were recording microearthquake activity and the distances between stations were few kilometers. The signals were sent in real time by wire or radio link to a central recording station. All data was recorded with central timing so there was an exact relative timing between stations and thus, locations of local earthquakes could be made accurately. At the beginning, recording was analog and, over the years, it has developed to be nearly only digital. Now, seismic monitoring is done by using global, regional and local seismograph networks has been automated so that event locations and magnitude determinations are often available and distributed online within minutes (Braile, 2009). There are no differences between networks such as data transfer, accuracy of timing, or time lag between data acquisition and analysis, but the differences in scope of investigation, spatial resolution, and quality of data in terms of frequency content and dynamic range are encountered (Bormann, 2002).

2.1.1. The Function of Seismic Networks

There are three main goals of seismic networks: for seismic alarm early warning, seismic monitoring, and research of the interior of the Earth. Nevertheless, the basic purpose is to obtain the accurate earthquake locations. For that reason, at least three stations are needed (Bormann, 2002).

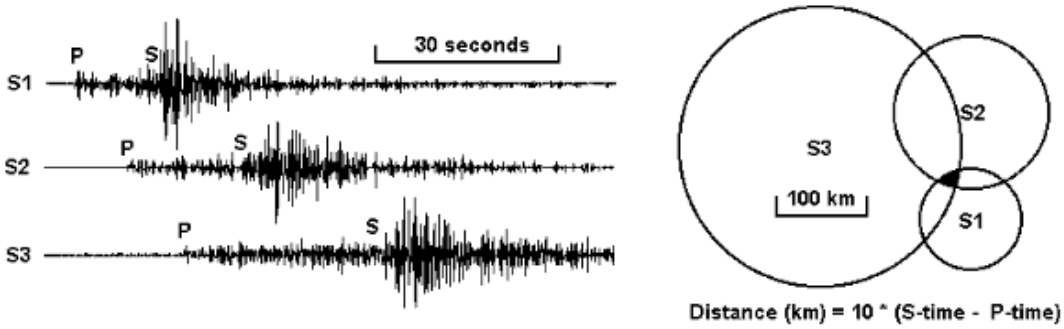

Figure 2.1. Epicenter location by the circle (or arc) method. The seismograms recording a local earthquake at stations S1, S2 and S3are shownd in the left. The locations of stations are shown in the right (NMSOP, 2002)

In Figure 2.1 the time diffrence between the P- and S-wave arrivals multiplied by the ratio vP·vS/(vP-vS) of the P- and S-wave velocities give the epicentral distance. The epicenter is found in the black area where the circles cross. It is clearly seen that with two stations, there are two possible locations, or no possible location if the two circles do not intersect. With more than three stations, the certainty of location increases. The "rule of thumb" formula is given in the lower right of the figure for the distance calculation (valid for Sn-Pn only) (Bormann, 2002).

The oldest aim of seismology is to make local, regional and global researches into the Earth's interior. Seismic networks are the only tools that qualify the detailed structure and physical properties of the deeper Earth's interior (Bormann, 2002).

The main object of seismic networks in high seismic areas is to determine the future seismic risk mitigation. For this reason, strong-motion recordings play a significant role and two sets of sensors have to be installed in order not to generate clips in the system. Nowadays, both types of sensors are integrated into a single system although there are important differences in strong and weak-motion network designs. Six-channel data loggers with three weak and three strong-motion channels are capable of covering the whole dynamic range of seismic events, from the lowest seismic noise to the largest damaging events (Bormann, 2002).

2.1.2. Characteristics of Seismic Stations

In the past, many seismic stations and networks were single component sensors and usually consisting of vertical seismometers because the equipment was analog and the record was on paper. Many of them are still in use. If three components had been used, the quality of equipment would have been better but the generated information would not have been more valuable. Today, the performance of three component seismic stations is favorable. Data recorders and data transmission links accept at least three channels of seismic data. On the other hand, one-component seismic stations are still a choice where communication capability and economy are limiting factors (Bormann, 2002).

Seismometers are very sensitive to small and distant events so they are too sensitive for strong-motion signals. This was a very appropriate point of view on analog recordings. Accelerometers have only been considered for strong motion and seismometers for weak motion. However, the latest technology accelerometers are almost as sensitive as short-period (SP) seismometers and also have a large dynamic range (up to more than 110 dB). Therefore, for SP networks, accelerometers work just as well as 1-Hz SP seismometers. In signal processing, there is no difference between using a seismometer or an accelerometer (Bormann, 2002).

Strong-motion accelerometers are designed to record the strongest events at small hypocentral distances. Their maximum acceleration is the gravity of the Earth (9.81 m/s^2). 0.25 g, 0.5 g, 1 g, 2 g, and 4 g sensitive accelerometers are available today and some accelerometers have perfect dynamic range and good signal resolution. They produce qualified records of smaller events near the epicentral region, where seismometer records may be clipped if a high-dynamic range recording system is not used. Too sensitive accelerometers may give clipped records for the strongest events (Bormann, 2002).

Weak-motion seismometers, are usually more sensitive, however, they cannot record large amplitudes like accelerometers. They can record very weak and/or very distant events that are comparable with amplitudes and the background seismic noise. Some seismometers can measure the lowest natural seismic noise which has smaller amplitudes than the ground motion amplitudes. It is also important to find appropriate, low seismic

noise sites for their installation. If the sites are not chosen appropriately or have high seismic noise, a seismometer with a high sensitivity highly is out of use. Using an accelerometer or a geophone might be suitable (Bormann, 2002).

Weak-motion sensors are divided into three classes: the short-period seismometers, broadband seismometers and very broadband seismometers (Bormann, 2002).

The short-period (SP) seismometers measure signals from 0.1 to 100 Hz, with a corner frequency at 1 Hz. They have a straight response to ground velocity for frequencies greater than this corner frequency. They are practical for local seismology where low frequencies of seismic signal are not of major interest or do not exist at all (Bormann, 2002).

The broadband seismometers (BB) have a flat response to ground velocity from 0.01 to 50 Hz. Therefore they allow a much broader range of studies than the SP records. The BB seismometers need a higher level of knowledge about instrumentation and analysis methods. They do not attenuate the 0.12 - 0.3 Hz natural seismic noise and their output signal contains much more seismic noise than a SP seismometer. These output seismic signals are buried in seismic noise and can be analyzed after filtering the remove background noise. BB seismometers are usually considered as the best choice. An example of a BB seismometer is the Guralp CMG40T seismometers which are operated by KOERI and have frequency range from 0.03 to 50 Hz (Bormann, 2002).

The very broadband seismometers (VBB) measure frequencies from below 0.001 Hz to approximately 10 Hz. They are employed in global seismology studies and able to resolve the lowest frequencies from Earth's tides and free oscillations of the Earth. Not only are they very expensive but also they are insufficient for seismic hazard analysis (Bormann, 2002).

Accelerometers measure seismic signals up to 200 Hz. Their output voltage is proportional to ground acceleration. However, seismometers' is proportional to the ground velocity. So, accelerometers stress high frequencies and attenuate low frequencies as

compared to seismometers. They are less appropriate for seismic applications where low-frequency signals are important (Bormann, 2002).

2.1.3. Forming a Seismic Network

In general, seismic stations are connected to the internet or to the public phone system. These stations are capable of recording a local seismic signal but there is not any real-time data transmission to a central site. They are all connected to the global communication network so they are defined to be a network. Theoretically, a networked computer that collects data from a number of stations is called a seismic network. In this way, the differences between local, regional, and global networks does not exist anymore in terms of hardware, data transmission and acquisition, but is basically a question of how the data collection software is set up to handle communication, data collection and processing (Bormann, 2002).

This means two types of seismic networks can be defined: physical and virtual. A physical seismic network (usually local) has remote seismic stations which are closely linked. The stations detect the ground motion and send data to the central recording station in real time. This type of network covers both the analog and digital systems. In Figure 2.2, the sensors are connected to a central recorder by means of a wire or radio link. The transmission may be analog with digitization taking place centrally, or an analog-to-digital converter (ADC) could also be placed at each sensor and the data transmitted digitally (Bormann, 2002).

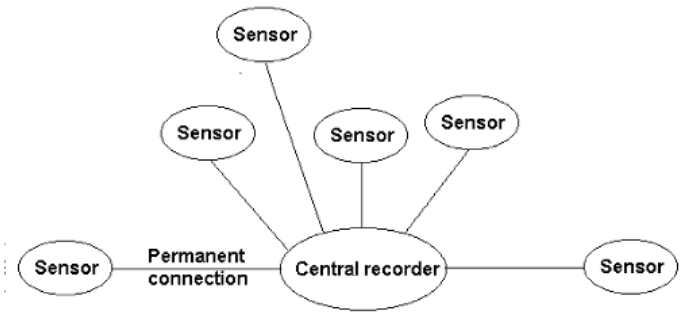

Figure 2.2. Schematic illustration of a physical seismic network (NMSOP, 2002)

A virtual seismic network is formed of seismic recorders that connected to a global communication network or a public phone system. A recorder may be related with a single seismic station or can be the central-recording site for a physical network. The remote recorders must detect local records as the data are not sent to the central recording system in real time. The central recording station is connected to the remote recorders and downloads data and makes the evaluation of possible events. Although, the virtual network carry data with a larger time delay than the physical network, both types of seismic networks might result in the same kind of output (Bormann, 2002).

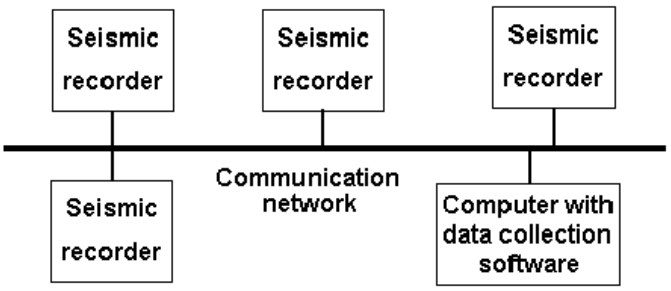

Figure 2.3. Schematic illustration of a virtual seismic network. The thick line is the communication network. The data collection computer collects data from some or all of the recorders connected to the network (NMSOP, 2002)

The determination of the kind of a network depends on two facts: price and the demand of real-time data. In the main, it is important to locate events and find out magnitude quickly. Hence, the raw data has to be obtainable in real time and a physical network must be used. There are two exceptions: virtual seismic networks that can operate real-time data transfer through the internet or each station in a network can supply event location and magnitude accurately and send to the central station. Data transfer must be done by remote stations, firstly. The drawback of the remote locations that are based on a single station data are not reliable so much because the results cannot be confirmed before the whole raw data arrives (Bormann, 2002).

It can be less expensive to set up a virtual network, if phone lines or a cell phone system is convenient at seismically quiet sites. For a large network, a virtual network may be the least costly choice (Bormann, 2002).

2.1.4. The Design and Function of KOERI Seismic Network

Seismic data acquisition in real time started in late seventies at Boğaziçi University Kandilli Observatory and Earthquake Research Institute (BU-KOERI). In recent years the national seismic network has been expanded considerably (Aktar and Karabulut, 2004). Now, it is composed of 158 seismic stations with 117 broadband three-component sensors, 21 short-period sensors, 15 accelerometers and 5 new OBSs (ocean-bottom seismometers) and controlled by NEMC (National Earthquake Monitoring Center). These 5 new ocean-bottom seismometers are expected to improve the location performance of the KOERI seismic network.

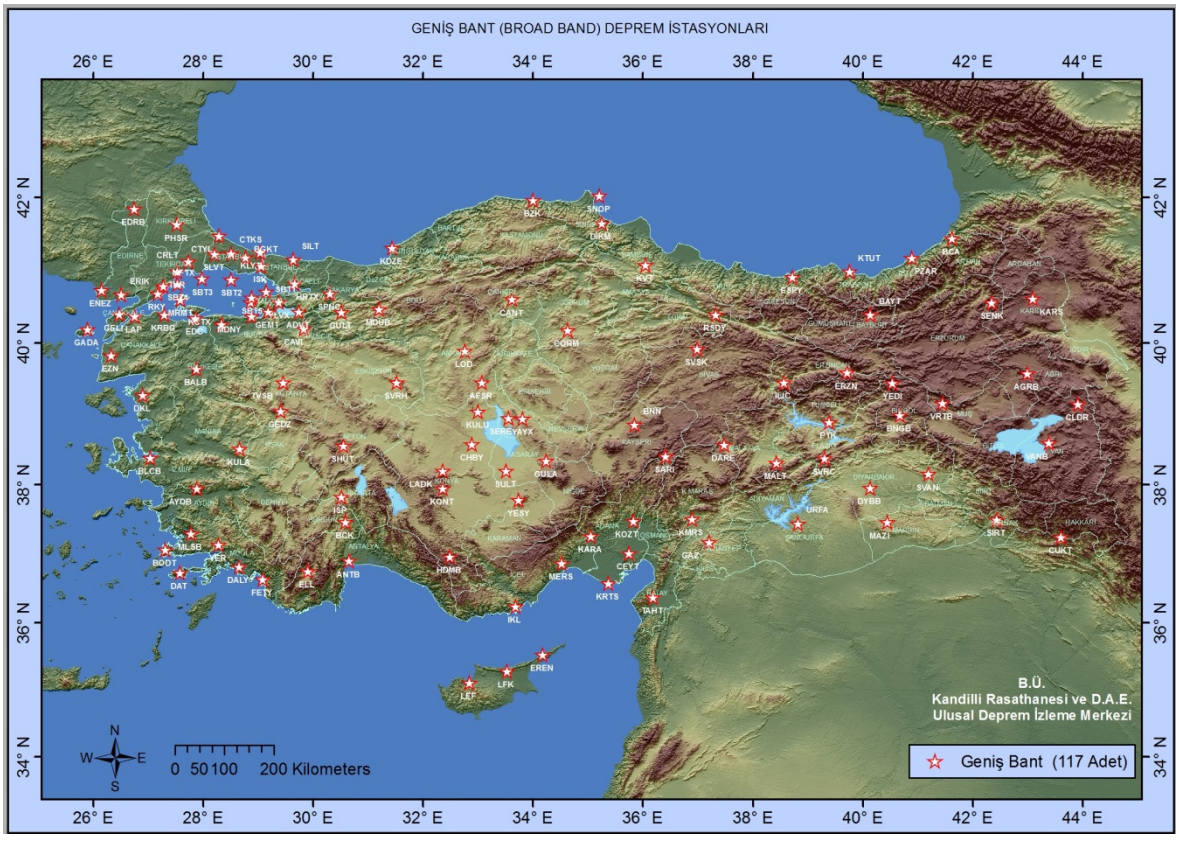

Figure 2.4. Location of BU-KOERI seismic stations (NEMC, 2011)

The national seismic network is related only with the observation of the deformation in the Earth's crust by studying seismic signals and makes the raw data available for research activities. The aim of the network is to give emergency information

about a big earthquake to public and related government agencies. It also takes a part in preparation of risk maps, urban planning and zonation (Aktar and Karabulut, 2004).

Leased-line digital telecommunication service, internet and satellite are used for data transmission. Data processing software systems are recommended for the National Data Center, such as the EARTHWORM (USGS) used at KOERI. EARTHWORM allows each institution to customize their own real-time system processing. It analyzes rapidly the earthquake activity and produces magnitude and location of earthquakes in real time as well as other products. This real-time information can be automatically delivered to the state authorities and system administrators by means of cell phones, fax and electronic mail. Data archiving is also an important issue. There are some international services (IRIS, ORFEUS, etc.) which disseminate the seismic data to the world (Aktar and Karabulut, 2004).

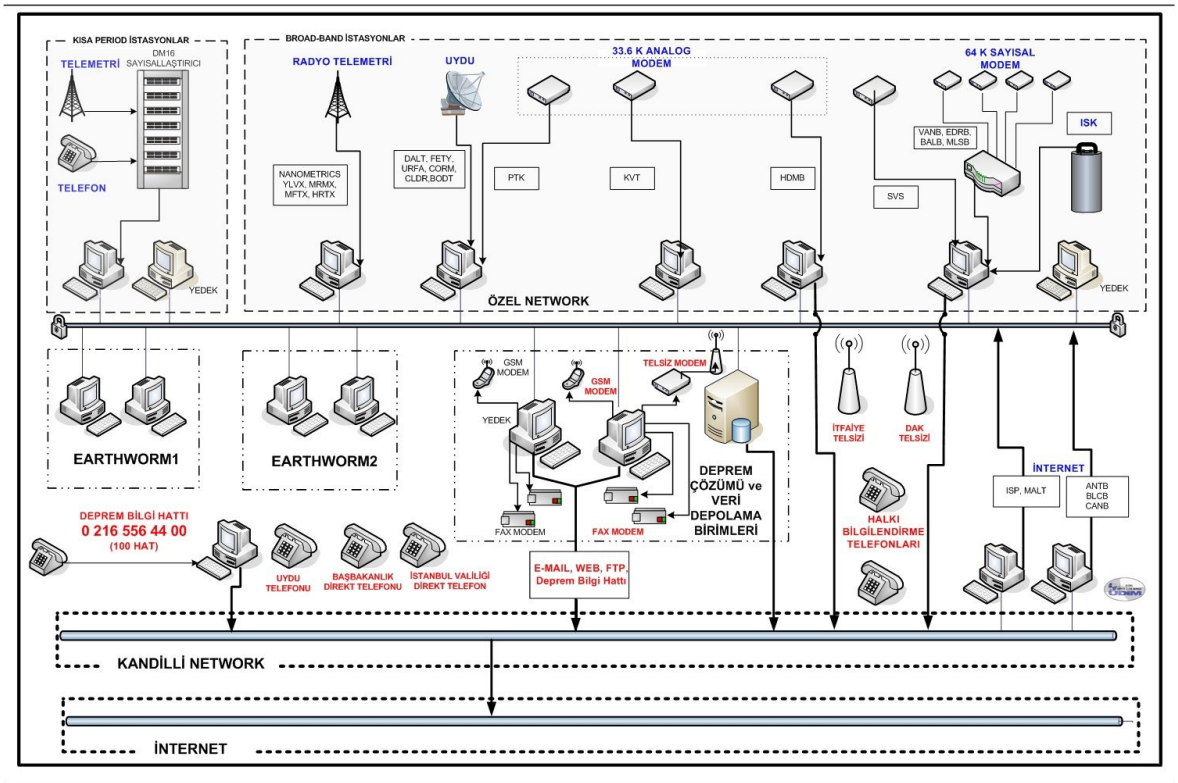

Figure 2.5. The operation of KOERI seismic network (NEMC, 2006)

Processing of real time data and scientific objectives has been improved with the construction of broadband seismometers. For instant, determination of earthquake location

is done automatically so it became more accurate and it has the capability of generating local and regional tomography and enhances the research of crust and upper mantle. For this purpose, KOERI uses Guralp CMG-3T (120 and 360 seconds), Guralp CMG-40T (30 seconds), Guralp CMG-3ESPD (30 and 120 seconds) and CMG-6T (30 seconds) broadband seismometers.

Figure 2.6. Güralp CMG - 3T broadband seismometer (taken from http://www.guralp.com)

2.2. Seismic Signals

In seismology, inverse problem is applied to the seismic records which bring significant information about the structure and physical properties of the inner Earth via the seismic waves' propagation path. While the seismic signals radiated from the source, are traveling through the Earth, they are weakened and deformed by geometric spreading, attenuation, diffraction, reflection, mode conversion, interference and also the transfer function of the seismograph. They are also distorted by the transfer function of the seismograph. Besides, seismic signals are sometimes disguised by seismic noise. Thus, SNR (signal to noise ratio) must be increased where conditions are bad by improving by appropriate ways of data acquisition and processing (Bormann, 2002).

A signal radiated from a seismic source is usually a complicated displacement step function or velocity impulse of finite duration from milliseconds up to a few minutes. According to the Fourier theorem any arbitrary transient function f(t) in the time domain can be represented by an equal function F(ω) in the frequency domain which is the Fourier transform of f(t). The following equations:

$$f(t) = (2\pi)^{-1} \int_{-\infty}^{\infty} F(\omega) \exp(i\omega t) d\omega \tag{2.1}$$

$$F(\omega) = \int_{-\infty}^{\infty} f(t) \exp(-i\omega t) dt = |F(\omega)| \exp\big(i\varphi(\omega)\big) \tag{2.2}$$

$|F(\omega)| = A(\omega)$, is the amplitude spectrum with the unit m/Hz, $\omega = 2\pi f$ the angular frequency (in unit Hz) and $\varphi(\omega)$ is the phase spectrum (with the units deg, rad or 2πrad). The integral f(t) is equal to a sum so the Fourier theorem explains that an arbitrary finite time series (even an impulsive one), can be expressed as a sum of monochromatic periodic functions (Bormann, 2002).

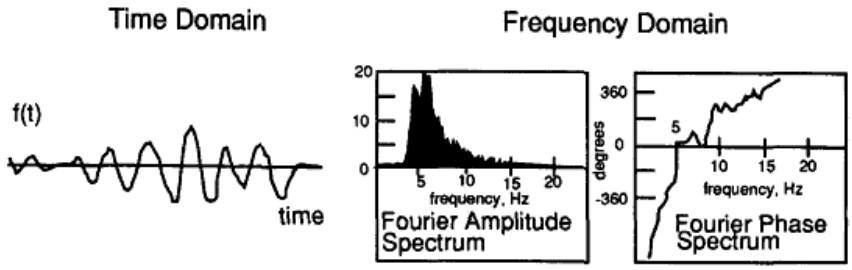

Figure 2.7. Schematic illustration of Fourier Transform of a signal (NMSOP, reproduced from Lay and Wallace, 1995)

Figure 2.7 shows that a signal recorded as a function of time (left) can be represented equivalently in the frequency domain by its Fourier spectrum. The amplitude (middle) and phase spectrum (right) are both needed to provide the complete time series (Bormann, 2002).

A needle impulse in the time domain is equal to an infinite homogeneous spectrum in the frequency domain. Otherwise, an infinite harmonic signal in the time domain is equivalent to a simply spectral line in the frequency domain. In another way, if the input signal is a needle impulse with an infinite spectrum but the bandwidth of the seismograph is too narrow (→ 0), then the record output won't be a needle impulse, but rather an almost un-attenuated infinite monochromatic record (Bormann, 2002).

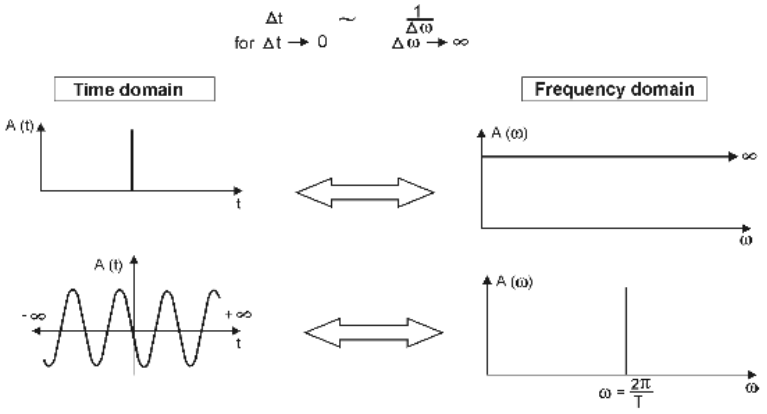

Figure 2.8. Schematic illustration of the equivalent representation of a needle impulse (above) and an infinite harmonic signal (below) in the time and frequency domain (NMSOP, 2002)

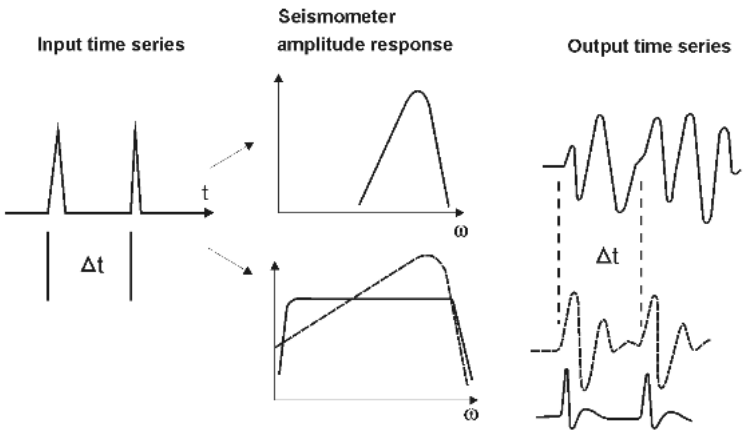

Figure 2.9. Schematic illustration of seismic impulses in record outputs of seismographs with narrow-band displacement response (upper) and broadband responses (below; broken line: velocity response, full line: displacement response) are illustrated. (NMSOP, 2002)

2.3. Seismic Noise

Seismic signals always carry noise and they have two origins: Noise generated by instrument and noise generated by earth vibrations which is accepted to be “real” noise; in other words ground noise (Havskov and Alguacil, 2004).

2.3.1. Short-period Seismic Noise

The source of short-period seismic noise can be wind, cultural noise and the movement of water. Seismic noise levels range from about 0.5 up to 50 Hz. Every site is exposed to these kinds of sources such as the distance from the ocean and cultural sources, the wind climate of the site and depth of burial of the sensor. There are also seasonal variations due to wind or water flow in nearby rivers (Webb, 2002).

Wind noise is usually the prevalent source from 0.5 to about 5 Hz. It depends on the strength of the wind and the feature of the site. Wind can join into high frequencies by its direct action on trees, bushes, and other structures although at lower frequency the fluctuations allied with wind can drive motions on the ground (Webb, 2002).

The dominant sources of high-frequency noise are man-made which are called cultural sources such as rotating or hammering machinery, road and rail traffic. In principle, cultural noise is avertable, although it is impractical to site stations at appropriate distances away from highways or cities (Webb, 2002). It is important to site stations as far as 25 km from power plants or rock-crushing machinery, 15 km from railways, 6 km from highways, and a kilometer or more from smaller roads (Wilmore, 1979).

2.3.2. Long-period Seismic Noise

Long-period seismic noise (0.2 to 50 MHz) is usually associated with atmospheric pressure fluctuations (Webb, 2002). On the other hand, long-period seismometers are always sensitive to temperature changes. Horizontal noise power may be larger than vertical noise power because of the tilt which joins gravity into the horizontal components (Bormann, 2002). Vertical component of seismometers may also respond to changes in

gravity at these very low frequencies (as the mass of atmosphere changes above a site with atmospheric pressure) (Webb, 2002). Another reason for long-period noise may be air circulation in the seismometer vault or underneath the sensor cover. Therefore, in order to reduce long-period environmental noise, seismometer installation and protection must be done carefully (Bormann, 2002).

There are two dominant peaks in the seismic spectrum which are called microseisms and easily recognizable at all broadband seismic stations. The lower amplitude, longer period peak is known as the single-frequency peak. The higher amplitude, shorter period peak is known as the double-frequency peak (McNamara and Buland, 2003).

2.4. Magnitude of Completeness (M_c)

Mc is defined as the lowest magnitude at which 100 per cent of the events are observed in a space-time volume. A part of events is missed by the network lower than this magnitude because they are too small to be detected by enough stations, or they are mixed with the coda of a larger event or they are below the magnitude of interest so they passed undetected (Rydelek and Sacks, 1989).

Although completeness is an essential parameter for seismicity studies, it does not provide any information about the errors in hypocentral location. The errors are related with the goodness of the velocity model used in hypocenter location and the distribution, density and background noise levels of the seismic stations (D'Alessandro *et al.,* 2001).

3. SEISMIC NETWORK EVALUATION THROUGH SIMULATION (SNES) METHOD

The SNES method evaluates the performance of a seismic network in hypocentral location routine by applying a numerical simulation. The SNES method requires the following input: the locations of the each seismic station in the network and their background noise levels, the velocity model used in hypocenter location routine and a law that allows estimating the variance in the residual times. The SNES method handles with the magnitude, confidence level and hypocentral depth, the deployment of the active stations involved in the location routine, the azimuthal gaps and confidence intervals in hypocentral parameters by considering both the distribution and the background seismic noise levels of the seismic network and the convenience of a velocity model (D'Alessandro *et al.,* 2001).

The SNES method is classified into five steps:

1) Estimate the background noise levels of the vertical components of each seismic station.

2) Estimate an empirical law which links the variance of the residual times to the hypocentral distance.

3) Hypocenters of earthquakes with fixed magnitude are simulated at the nodes of a regular grid and then the seismic spectra at the receivers are calculated by considering the effects of propagation.

4) Determine the ratio between the earthquake seismic spectra and noise spectra which contributes useful information for the hypocenter locations.

5) Generate the covariance matrices of the data, the partial derivatives of the model and then generate the covariance matrices of the hypocentral parameters (D'Alessandro *et al.,* 2001).

3.1. Characterization of the Seismic Noise

For each station, the mean and the variance of the vertical component of noise is estimated. The location of a seismic network is intensely affected by the noisiness of its stations. Therefore, the characterization of the seismic noise is an essential part of the SNES method. In fact, the exact reading of the seismic phases is dependent to the quality of the signal or to its wideband spectral ratio (WSR) which is the ratio between the mean power spectral density (PSD) of the earthquake signals and that of the background seismic noise (D'Alessandro *et al.,* 2001).

"Many sources of noise may compromise the performance of a seismic network" (Webb, 2002). The map of a mean seismic noise demonstrates the distribution of the noise levels of the stations (D'Alessandro *et al.,* 2001).

3.1.1. Noise Spectra

It is possible to get the noise level at all frequencies with a simple operation (Havskov and Alguacil, 2004). The seismic signal or noise power $(a_2/a_1)^2$ is usually indicated in units of dB (= deciBel). The power difference in dB is $10 \log[(a_2/a_1)^2] = 20 \log(a_2/a_1)$. The power spectral density in units of dB is $1 (m/s^2)^2/Hz$, it can be written as:

$$P_a[dB] = 10 \log (P_a/1(m/s^2)^2/Hz) \tag{3.1}$$

A new world-wide noise model was introduced by Peterson (1993) in these units. It describes the upper limits and lower limits of the accumulated ground acceleration power spectral densities which are determined by means of 75 global digital stations for noisy and quiet periods. The models which are the New High Noise Model (NHNM) and New Low Noise Model (NLNM), demonstrate the presently received expected limits of seismic noise. Some cases may go beyond these limits (Bormann, 2002).

$$P_v[dB] = P_a[dB] + 20 \log (T/2\pi) \tag{3.2}$$

$$P_d[dB] = P_a[dB] + 40 \log (T/2\pi) = P_v[dB] + 20 \log (T/2\pi) \tag{3.3}$$

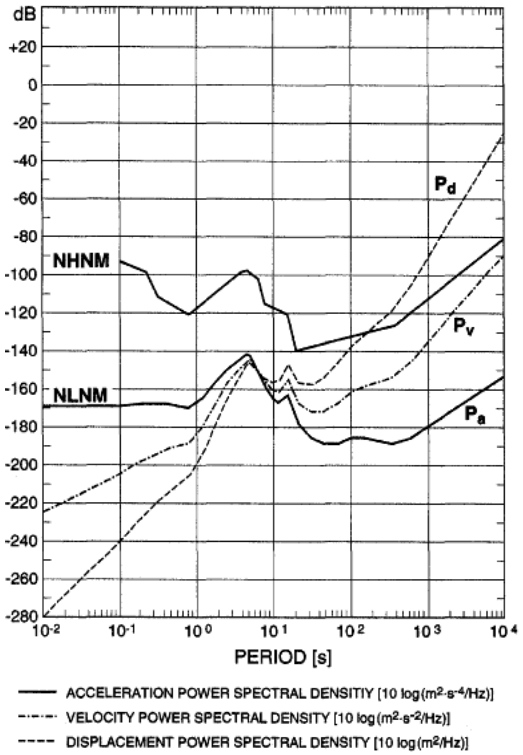

Figure 3.1 NHNM and NLNM of Peterson (1993). Envelope curves of acceleration (Pa), velocity (Pv) and displacement noise power spectral density (Pd) (in dB) are shown as a function of noise period (NMSOP, 2002)

3.1.2. Power Spectral Density

PSD (power spectral density) quantifies the seismic background noise (McNamara and Buland, 2003).

The most known method for estimating the PSD for stationary random seismic data is the direct Fourier transform or Cooley-Tukey method (Cooley and Tukey, 1965). The method calculates the PSD via a finite-range fast Fourier transform (FFT) of the original data (D. E. McNamara and R. P. Buland, 2003). The PSD of a random process and finite power y(t) ($0 \leq t \leq Tr$), can be calculated by using the Fourier transform of the signal (D'Alessandro *et al.,* 2001).

$$Y(f, Tr) = \int_0^{Tr} y(t) \exp(-i2\pi f t)\, dt \qquad (3.4)$$

where Tr = length of time series segments,

f = frequency.

For discrete frequency values, fk, the Fourier components are described as:

$$Yk = \frac{Y(fk, Tr)}{\Delta t} \tag{3.5}$$

for, $f_k = k / NDt$ when k = 1, 2, …, N-1,

where Δt = sample interval

N = number of samples in each time-series segment, $N = Tr / \Delta t$.

As a result, by using the Fourier components described above, the total power spectral density calculation is defined as (McNamara and Buland, 2003) :

$$P_k = \frac{2\Delta t}{N} |Yk|^2 \tag{3.6}$$

3.1.3. Welch's Method

Welch's method or mediated periodogram is used to calculate the power of a signal vs. frequency. It decreases noise in the estimated power spectra (Proakis and Manolakis, 1996).

The signal is divided into K data segments of length L, overlapping by D points. If D = M / 2, the overlap is going to be 50 per cent, if D = 0, the overlap is said to be 0 per cent. Then the overlapping segments are windowed. After dividing into overlapping segments, the individual K data segments have a window applied to them in the time domain. Because of the windowing of the segments, Welch method becomes a "modified" periodogram. After doing those above, the periodogram is calculated by the discrete Fourier transform, and then calculating the squared magnitude of the result. Then the single periodograms are time-averaged, which decreases the variance of the discrete power measurements (Proakis and Manolakis, 1996).

A half-overlapped signal, for which its periodograms are, calculated by (D'Alessandro *et al.,* 2001):

$$Pw\,(f) = \frac{1}{K}\sum_{k=1}^{K} P_{L,K}\,(f) \tag{3.7}$$

3.2. Estimation of The Residual Time Variances of The Seismic Phases

An empirical law that binds the variance of the residual times of P and S phases to the hypocentral distance is obtained by using residual times in the earthquake catalogue. Understanding of the variance of the residual times is important for estimating the confidence region in the location procedure (D'Alessandro *et al.,* 2001).

The uncertainties of estimated hypocentral parameters are related with the variance of the residual times ($\sigma^2_{\Delta T}$) with the assumption of no errors in the velocity model or in the seismic phase readings. This is a function of the variance of WSR (σ^2_{WSR}) and the variance of the velocity model used (σ^2_{MOD}) which is given below (D'Alessandro *et al.,* 2001).

$$\sigma^2_{\Delta T} = \sigma^2_{WSR} + \sigma^2_{MOD} \tag{3.8}$$

The σ^2_{WSR} in the reading of seismic phases P_g and P_n is very small (~ 0.01 s^2) while WSR values greater than 10 in the frequency range 0.1-10 Hz (Zeiler and Velasco, 2009). Nevertheless, the variance of the residual time $\sigma^2_{\Delta T}$ takes a much larger value and this distinction is assigned to σ^2_{MOD} (D'Alessandro *et al.,* 2001).

The variance σ^2_{MOD} does not taken into account for the geological complexity of the area. It can take values much greater than phase-picking uncertainty. Larger values of σ^2_{MOD} imply that the model fails to sufficient for velocity structure in the monitored region. The evaluation of the goodness of the velocity model can be achieved by a statistical analysis of residual time variance. It helps identifing the systematic errors (D'Alessandro *et al.,* 2001).

3.3. Earthquake Spectra Calculation

The circumstances for the earthquake simulation and seismic spectra calculations should be created. For this reason, it is important to define an appropriate source and velocity and attenuation models to estimate for a particular magnitude and hypocenter position, the earthquake energy that reaches at the receivers, by considering the effects of propagation (D'Alessandro *et al.,* 2001).

It is possible to compute the seismic wave spectrum at the focus S (ω) or its envelope of mean azimuthal average $\bar{S}(\omega)$ with the defined source model. The amplitude and frequency content are changed by attenuation of the waveform propagating away from the source. Hence, the seismic spectrum $\bar{S}_R$ (ω,x) estimated at a receiver at position x takes into account the attenuation because of the geometrical spreading, the partitioning of energy in the existence of interfaces and free surface effects which are the only attenuation effects in a perfect elastic medium and also energy dispersion due to an imperfect elasticity and scattering fact (D'Alessandro *et al.,* 2001).

The model can be defined as the Fourier transform of the impulse generated by the source S(t) (D'Alessandro *et al.,* 2001).

$$S(\omega) = \frac{1}{2\pi} \int_{-\infty}^{+\infty} S(t)\, e^{-i\omega t} dt \qquad (3.9)$$

In general, the amplitude of the seismic spectrum is explained by complex models that are linked to the specific functions of directivity. They suggest a dependence of the spectrum on the direction of observation and are the direct results of the finite source extension. Because of the destructive interference of seismic waves radiated from the source, some frequencies cannot be detected and the high frequencies are attenuated by laws of the type $\omega^{-\gamma}$ (D'Alessandro *et al.,* 2001).

Therefore, S(ω) is usually described in terms of the envelope of mean azimuthal average $\bar{S}(\omega)$ and represented in bi-logarithmic axes. For a finite source extension, $\bar{S}(\omega)$ is defined by

$$\bar{S}(\omega) = C_s \frac{M_0}{1 + (\frac{\omega}{\omega_0})^{\gamma}} \omega^2 \tag{3.10}$$

where ω is the angular frequency, M_0 is the scalar seismic moment, ω_0 is the corner frequency, γ is the damping constant for high frequencies and also a function of the source models taking values between 0 and 3 (usually 2), C_s is a constant depends on the phase and source model taking into account and n takes values 0, 1 or 2 depending on displacement, velocity or acceleration, respectively (D'Alessandro *et al.,* 2001).

The seismic spectrum are defined by far-field or near-field approximations. Far-field approximations are often used which are made at hypocentral distances much greater than the average size of the seismic sources. (D'Alessandro *et al.,* 2001).

Brune's circular fault model (1970) is commonly used for M<6 events. "The source model presented by Brune (1970) includes a flat circular fault with a finite radius α the action of which is that of a shear stress pulse dedicated to the whole surface but in the opposite direction on the two inner surfaces of the fault" (D'Alessandro *et al.,* 2001). Hence, C_s for the amplitude far-field may be calculated (Brune, 1970) under the assumption of homogeneous elastic medium and the whole stress fall

$$C_s = \frac{Rp}{4\pi\rho r c^3} \tag{3.11}$$

where ρ is the density of the medium, r is the hypocentral distance, c is the velocity of P or S depending on the spectrum considered and R_p is the mean square value of the directivity function of the source averaged all over the solid angle. R_p takes values of 0.55 and 0.65 for P and S phases, respectively. Under the assumption of a homogeneous medium, the r dependence takes into account the geometric attenuation G(x) (D'Alessandro *et al.,* 2001).

The M_0 scalar seismic moment can be determined by the M_L local magnitude using the Hanks and Kanamori relation (1979) (D'Alessandro *et al.,* 2001).

$$\mathrm{Log}_{10}\, M_0 = 1.5\, M_L + 16.0 \tag{3.12}$$

For high frequencies, the amplitude seismic spectrum is directed by the pulse shape produced at the source (Brune, 1970)

$$S(t) = M_0\, C_s\, \omega_0{}^2\, t\, e^{-t\,\omega_0} \tag{3.13}$$

and especially the sudden rise of the pulse at t = 0. For frequencies over the corner frequency ω_0, are related with the radius of the source α, the earthquake spectrum decreases as ω^{-2}

$$\alpha = \frac{kc}{\omega_0} \tag{3.14}$$

where k is a constant depends on the velocity of the fault rupture and the time of stress release. For constant rupture velocity V_c equals to 0.9β and instant release of stress, k takes values of 3.36 and 2.34 for P and S waves, respectively (Brune, 1970).

The stress drop Δσ is related to the scalar seismic moment M_0

$$\Delta\sigma = \frac{7M_0}{16a^3} \tag{3.15}$$

The corner frequency ω_0 can be expressed by combining (3.14) and (3.15)

$$\omega_0 = \sqrt[3]{\frac{\Delta\sigma}{M_0}}\,.\,\xi\,.\,c \tag{3.16}$$

where $\xi = \sqrt[3]{16/7}k$. As it is clearly seen from the Equation (3.16), the corner frequency is directly proportional to the fall of stress and to the velocity of the medium and inversely

proportional to the scalar seismic moment and so to the magnitude. Moderate sized events have values $\Delta\sigma$, consist of the narrow range 1-10 MPa with an average value of about 6 MPa (Kanamori and Anderson, 1975).

The attenuation change the amplitude and the frequency content of the waveform during travelling. Therefore, the seismic spectrum $\bar{S}_R(\omega,x)$ at a generic receiver position **x** is going to be

$$\bar{S}_R(\omega,x) = \bar{S}(\omega)\, E(\mathbf{x})\, A(\omega,\mathbf{x}) \tag{3.17}$$

where $E(\mathbf{x})$ is considered to be the attenuation because of the expansion of the wave front or geometrical spreading, the partitioning of energy at the interfaces and free surface effects. $A(\omega,\mathbf{x})$ is related with both energy dispersion due to the imperfect elastic medium and scattering phenomenon (D'Alessandro *et al.,* 2001).

The wave attenuation is defined by the spreading of the wave front $G(\mathbf{x})$. It is coherent with the ray theory and by splitting of energy at the buried interfaces $P(\mathbf{x})$ and at the free surface $F(\mathbf{x})$ (D'Alessandro *et al.,* 2001).

$$E(\mathbf{x}) = G(\mathbf{x})\, P(\mathbf{x})\, F(\mathbf{x}) \tag{3.18}$$

These attenuations comply with the law of protection of energy and are a direct solution of it. Assuming a homogeneous and elastic medium, geometric attenuation $G(\mathbf{x})$ is taken into account for being equivalent to the inverse of the hypocentral distance

$$G(\mathbf{x}) = 1 / r(\mathbf{x}) \tag{3.19}$$

where $r(\mathbf{x}) = \sqrt{h^2 + d^2}$, h is the hypocentral depth and d is the epicentral distance. From (3.19), it is seen that $G(\mathbf{x})$ is independent of frequency. Nevertheless, the distance which the seismic wave travel is different from the hypocentral distance because of the complexity of the geological structures crossed (D'Alessandro *et al.,* 2001).

The complexity of underground is usually outlined by 1D velocity models. The propagation of seismic waves obey the law of Snell equations which explains in a 1D medium that the velocity varies with depth z, takes the form

$$\frac{\sin i(z)}{c(z)} = p \tag{3.20}$$

where p is the ray parameter or horizontal apparent slowness, i(z) is the incidence angle and c(z) is the velocity of the body wave. The travel times and the changes in the amplitude can be determined by using Snell's law (D'Alessandro *et al.,* 2001).

"While analyzing a seismogram, it is easy to find out the seismic phase which has the lower travel time and usually, it is the only one used in the hypocentral location procedure. The arrival order of the seismic phases linked to the body wave depends on the epicentral distance, mechanical-geometrical parameters of the model and hypocentral depth" (D'Alessandro *et al.,* 2001).

For homogeneous layers with horizontal interfaces, the length of the ray x_k and its travel time t_k of the critically refracted wave from the top of the k-th layer for stations with epicentral distance d, can be obtained by the formulas below (D'Alessandro *et al.,* 2001).

$$x_k = d + \sum_{i=m}^{k} h_i \ (\cos^{-1} i_i - \tan i_i) + \sum_{i=n}^{k} h_i \ (\cos^{-1} i_i - \tan i_i) \tag{3.21}$$

$$tk = \frac{d}{c_k} + \sum_{i=m}^{k} \frac{h_i \cos i_i}{c_i} + \sum_{i=n}^{k} \frac{h_i \cos i_i}{c_i} \tag{3.22}$$

where c_i is the velocity of the seismic waves in the layer h_i and i_k is the angle of critical refraction. "In (3.21) and (3.22) the station and the hypocenter are located on the top of the m-th and the n-th layers, respectively. If the altitude of the hypocenter and/or of the station does not intersect with any interface, h_m and h_n must be corrected by considering the effective fraction of the layer crossed. The improvement of travel times and amplitudes for

stations placed above sea level was carried out by enlarging the upper layer of the velocity model up to the station altitude" (D'Alessandro *et al.,* 2001).

Phases that have minimum travel times near the epicenter are given by direct waves. Nonetheless, it is not possible to display the length of the rays and travel times by basic analytical expressions. They can be obtained iteratively by applying the technique of "shooting". In this method, a seismic ray is shot from the source with the azimuth of the seismic station and the angle which the ray makes with the vertical in the source is varied iteratively to determine its emergence in the seismic station location (D'Alessandro *et al.,* 2001).

Thus, if there is a P wave velocity model and a fixed hypocentral depth, the first arrival of the phase on the seismogram will be dependent on the epicentral distance. Under the assumption of increasing velocity with depth, epicentral distance increases and the ray of the minimum seismic travel time will tend to deepen along those pathways that are related with the critical refractions from layers that are even deeper. The geometric attenuation displays some discontinuity that is compatible with that of the apparent velocity. These discontinuities are linked to the modification of the phase related to the first arrival (D'Alessandro *et al.,* 2001).

With the law of protection of energy, the division of the energy at the interfaces is the total of the energy density flows of refracted and reflected waves equals to the energy density flow of the incident wave (D'Alessandro *et al.,* 2001).

$$\sum \frac{1}{2} \, c \, p \, A^2 \, \omega^2 = \cos t \tag{3.23}$$

The equations that explain the derivation of energy partitioning at interfaces P(**x**) in terms of amplitudes were determined from Zoeppritz (1919).

For a plain P wave with the amplitude A_0 and incident on an interface between two elastic media having different mechanical features, assuming that there is a continuity of

stress and displacement, the partition of energy in terms of amplitude is controlled by the system equations below

$$A_1 \cos\Theta_1 - B_1 \sin\lambda_1 + A_2 \cos\Theta_2 + B_2 \sin\lambda_2 = A_0 \cos\Theta_1 \quad (3.24)$$

$$A_1 \sin\Theta_1 + B_1 \cos\lambda_1 - A_2 \sin\Theta_2 + B_2 \cos\lambda_2 = -A_0 \sin\Theta_1 \quad (3.25)$$

$$A_1 Z_1 \cos 2\lambda_1 - B_1 W_1 \sin 2\lambda_1 - A_2 Z_2 \cos 2\lambda_2 - B_2 W_2 \sin 2\lambda_2 = -A_0 Z_1 \cos 2\lambda_1 \quad (3.26)$$

$$A_1 \gamma_1 W_1 \sin 2\Theta_1 + B_1 W_1 \cos 2\lambda_1 + A_2 \gamma_2 W_2 \sin 2\Theta_2 - B_2 W_2 \cos 2\lambda_2 = A_0 \gamma_1 W_1 \sin 2\Theta_1 \quad (3.27)$$

where $\gamma_i = \beta_i/\alpha_i$, $Z_i = p_i\alpha_i$ and $W_i = p_i\beta_i$ for i = 1, 2. A_1, A_2, Θ_1 and Θ_2 are the amplitudes and the angles of P waves reflected and refracted, respectively while B_1, B_2, λ_1 and λ_2 are the amplitude and the angles of reflected and refracted S waves respectively. "The solution of the equation system is given by means of complex functions. The module and phase supply the amplitude and the phase of reflection and refraction coefficients, respectively. The values of the reflection coefficients are between -1 and +1, while the values of refraction coefficients are between 0 and 2" (D'Alessandro *et al.,* 2001).

With the determination of the amplitude of P and S waves reflected from an interface, the effect of free surface F(**x**) can be calculated (D'Alessandro *et al.,* 2001).

$$A_1 = A_0 \frac{\sin 2\Theta_1 \sin 2\lambda_1 - (\alpha/\beta)^2 \cos^2 2\lambda_1}{\sin 2\Theta_1 \sin 2\lambda_1 + (\alpha/\beta)^2 \cos^2 2\lambda_1} \quad (3.28)$$

$$B_1 = A_0 \frac{2(\alpha/\beta) \sin 2\Theta_1 \cos 2\lambda_1}{\sin 2\Theta_1 \sin 2\lambda_1 + (\alpha/\beta)^2 \cos^2 2\lambda_1} \quad (3.29)$$

If the incidence angles are close to normal, the incident and reflected waves combine together and they double the amplitude of the original signal (D'Alessandro *et al.,* 2001).

A frequency-dependent attenuation of the wavefield A (ω,**x**) is caused by the imperfect elasticity of rocks and the presence of a small-sized random component in the heterogeneity of the mechanical parameters and defined as below

$$A(\omega,\mathbf{x}) = I(\omega,\mathbf{x})\, S(\omega,\mathbf{x})\, B(\omega) \tag{3.30}$$

where I (ω,**x**) is the attenuation depending on the rheology of the medium, S (ω,**x**) is the attenuation caused by scattering phenomena and B (ω) is the transfer function of the first layer under the station, I (ω,**x**) is linked to the friction of the inside medium which transforms the mechanical energy into the heat energy. Additionally, the interaction of the wavefield with random small-sized heterogeneity generates the scattering (D'Alessandro *et al.,* 2001).

The quality factors $Q_i(\omega)^{-1}$ and $Q_s(\omega)^{-1}$ quantify scattering and the attenuation inside the medium. For a given medium, they express that the fraction of energy lost during a complete cycle of a monochromatic wave of frequency ω. The two phenomena are described by an exponential function below

$$I(\omega,\mathbf{x})\, S(\omega,\mathbf{x}) = e^{-\left(\frac{\omega r}{2cQ_T(\omega)}\right)} \tag{3.31}$$

where $Q_T(\omega)^{-1} = Q_i(\omega)^{-1} + Q_s(\omega)^{-1}$ which is the sum of the quality factor includes both effects. The frequency dependence Q_T was observed theoretically which can be written as:

$$Q_T = Q_0\, \omega^b \tag{3.32}$$

where Q_0 is the quality factor for ω = 1 Hz and b is the exponent that displays the variation of the frequencies (D'Alessandro *et al.,* 2001).

Considering the lithosphere, for Q_0 values of the order of 10^2 and for b values between 0.5 and 1 were observed in the range of frequencies between 0.1 and 20 Hz. Normally, the quality factor of P waves is greater than the quality factor of S waves in the same medium. Their ratio Q_α/Q_β ranges between 1 and 2. If b<1, the high frequencies will be more attenuated than the low frequencies (Sato *et al.,* 2002).

The transfer function B (ω) is independent from hypocentral distance but it is frequency dependent (Anderson and Hough, 1984).

$$B(\omega) = e^{-\pi\delta f} \tag{3.33}$$

where δ is the near surface attenuation and takes positive real values of the order of 10^{-2} s^{-1} with typical value of 0.05 s^{-1} (Havskov and Ottemöller, 2010).

3.4. Determination of the Ratio of Earthquake-to-Noise Spectra

Earthquakes with fixed magnitude and hypocentral depth are simulated at the nodes of a regular grid. The theoretical seismic spectra at the receivers and the ratio between this spectrum and the previously estimated noise spectra are determined for each simulated earthquake. This stage gives information about the seismic stations' detection capabilities in the hypocenter location process (D'Alessandro *et al.,* 2001).

In this step, the maps of numbers of active stations in location routine with azimuthal gaps and the M_c are composed. The azimuthal gap is the largest gap between any two seismic stations used in epicenter solution. A gap of 180° or larger implies that the event occurred outside the network (D'Alessandro *et al.,* 2001).

3.5. Construction of the Covariance Matrices

"The hypocentral depth, which is one of the hypocentral parameters, is the most difficult one to determine for regional events. Because of the fact that, the travel-time derivative with respect to depth, changes very slowly as a function of the depth if the station is far away from the epicenter. In other words, with the little changes in travel times, the depth can be moved up and down" (D'Alessandro *et al.,* 2001).

"The focal depth is well restraint only when the phases that are put in the location routine have a different sign from the partial derivative, such as for a local event; direct upgoing Pg and downgoing Pn are observed" (D'Alessandro *et al.,* 2001).

The uncertainity of hypocentral-parameter is related with the hypocentral depth, magnitude and confidence level. In this stage, the covariance matrix C_d is generated. The diagonal terms of C_d are the variances in the estimated residual times, while the off-diagonal terms are the covariances which express the relationship between errors of pairs of stations. Assuming that there is no correlation between reading errors of arrival time on different stations, the off-diagonal matrices of C_d is set to be zero. This assumption can be used to determine the covariance matrix of the solution C_s:

$$\mathbf{C_s = G^{-g} C_d \, [G^{-g}]^T} \tag{3.34}$$

where G^{-g} is the generalized inverse matrix of the travel-time spatial derivatives that are calculated at the hypocenter. The covariance matrix $\mathbf{C_s}$ provides the variances and covariances of the origin time T_0 and of the hypocentral coordinates (x_0, y_0, z_0) (D'Alessandro *et al.,* 2001).

"Hereafter, the uncertainty in hypocentral parameters can be estimated as the confidence interval for a x^2 distribution with four degrees of freedom. The confidence interval of the generic focal parameter r_{par} at the confidence level of 95 per cent can be estimated as

$$r_{par} = \sqrt{9.488 \,.\, \sigma^2_{par}} \tag{3.35}$$

where σ^2_{par} is the variance of the focal parameter taking into account and 9.488 is the value of Δx^2 for the confidence level of 95 per cent and four degrees of freedom. The axes of the confidence ellipsoid was obtained by eliminating the terms of C_s related to time origin and defining them in basic form. In order to estimate an average location error, the radius of equivalent sphere (RES) can be also determined:

$$RES = \sqrt{r_1 \,.\, r_2 \,.\, r_3} \tag{3.36}$$

where r_1, r_2 and r_3 are the semiaxes of the confidence ellipsoid. It is essential to indicate that this kind of error estimate does not take into account location bias caused by systematic model errors. The real error will exceed this estimate. Thus, the SNES method can only estimate the correctness of the hypocentral location, not its accuracy" (D'Alessandro *et al.,* 2001).

4. DATA COLLECTION

The first step of the SNES method is to estimate the noise power of the vertical components for each station of the seismic network. For this reason, continuous seismic records from NEMC of KOERI for the period 2005-2010 has been compiled.

For the next stage, the earthquake catalogues were taken from NEMC. They include the same years as the continuous seismic records and consist of 20,259 events with all magnitude values. They contain the date, origin time, duration and local magnitudes (MD and ML, respectively), epicenters and depth information of earthquakes. The hypocenter locations of events were not re-determined.

In order to evaluate the appropriateness used in location routine, the velocity model of Turkey was required. The hypocenter locations of the selected earthquakes were previously calculated by using HYPO71 program considering the velocity model of Kalafat *et al.,* (1987). Moreover, the empirical law that link the variance of residual times to the hypocentral distance, was estimated by means of this velocity model.

These are used as input of SNES code and then outputs of the location performance and magnitude of completeness were evaluated.

5. DATA ANALYSIS

5.1. Characterization of the Seismic Noise

For each station, a large number of three-hour waveform segments during a 6 year period were selected from continuous digital seismic data. Each year was divided into four seasons and one month represents each season (Winter, Spring, Summer and Fall were represented by January, April, July and October, respectively). Five different days and nights were also picked in each month (day times were preferred from 5 a.m. to 5 p.m. and night times from 5 p.m. to 5 a.m.). For each five nights and five days of a month, the acceleration PSD curves of the vertical component of the noise were generated, related to the period 2005-2010. It is also possible to make a comparison of PSD curves of seasons and day and night related to the noise levels at each site.

The selection of the three-hour waveform was made by eyesight by using Scream 4.5 seismic monitoring software program. Furthermore, attention was paid only to choose noisy parts, not to choose earthquake waveforms. Thus, the days the events occurred were ignored because they can contaminate the raw noise signals.

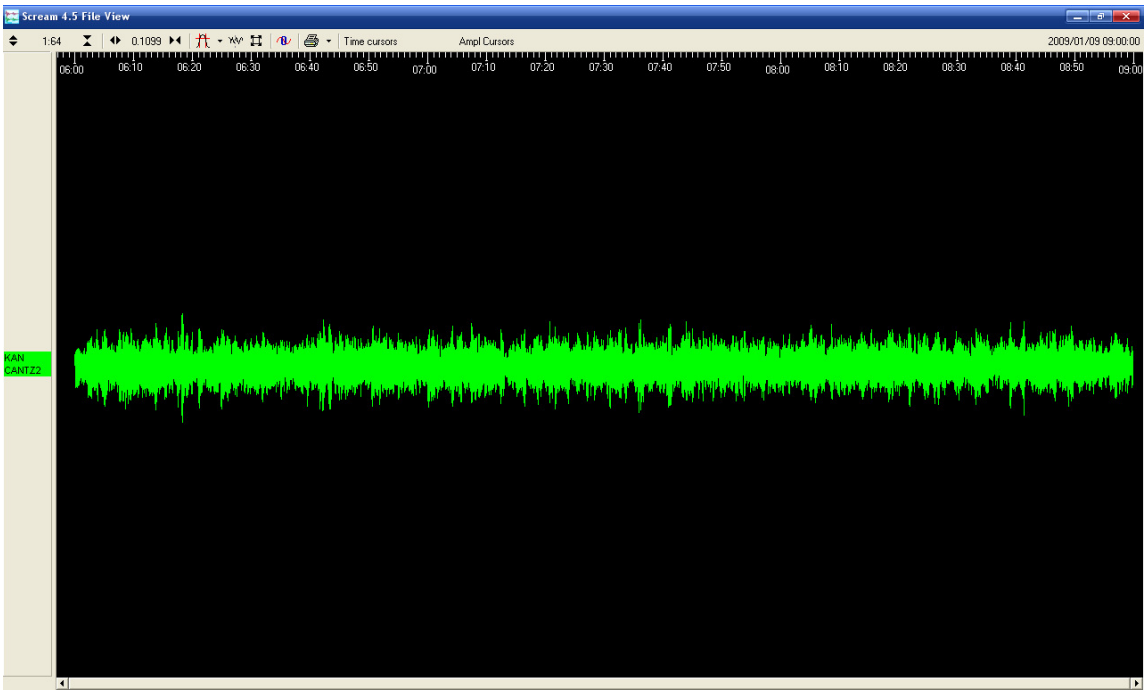

Figure 5.1. Seismic noise record of the vertical component of CANT station on January 9th 2009, during 06:00-09:00 GMT

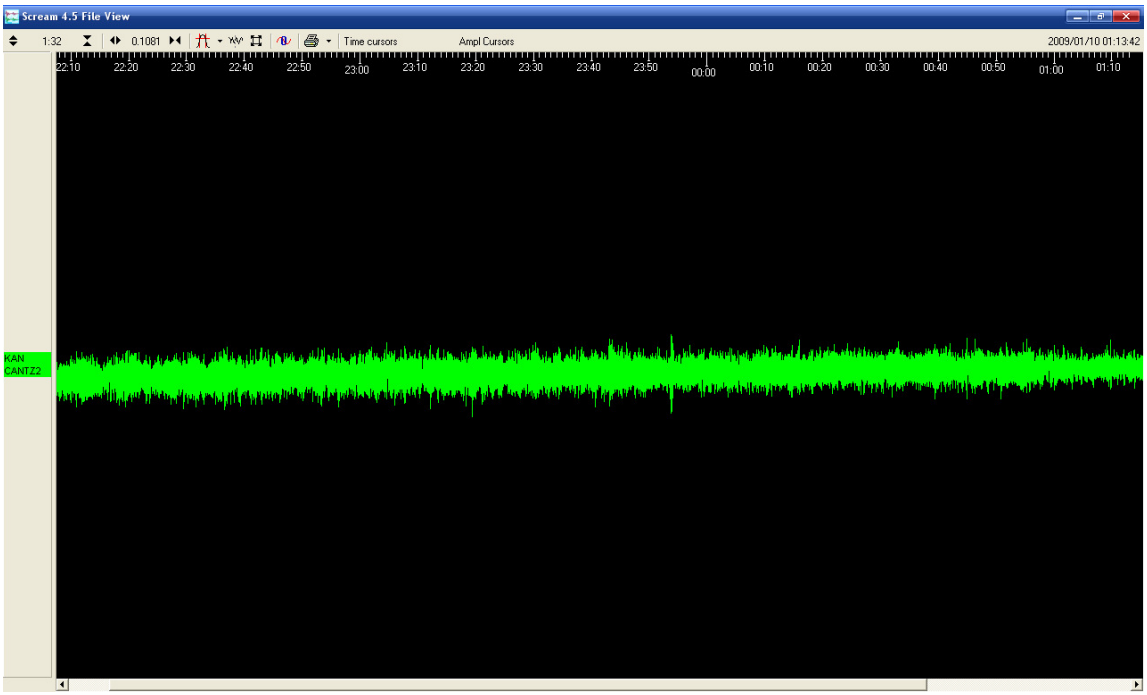

Figure 5.2. Seismic noise record of the vertical component of CANT station on January 9th 2009, during 22:10-01:10 GMT

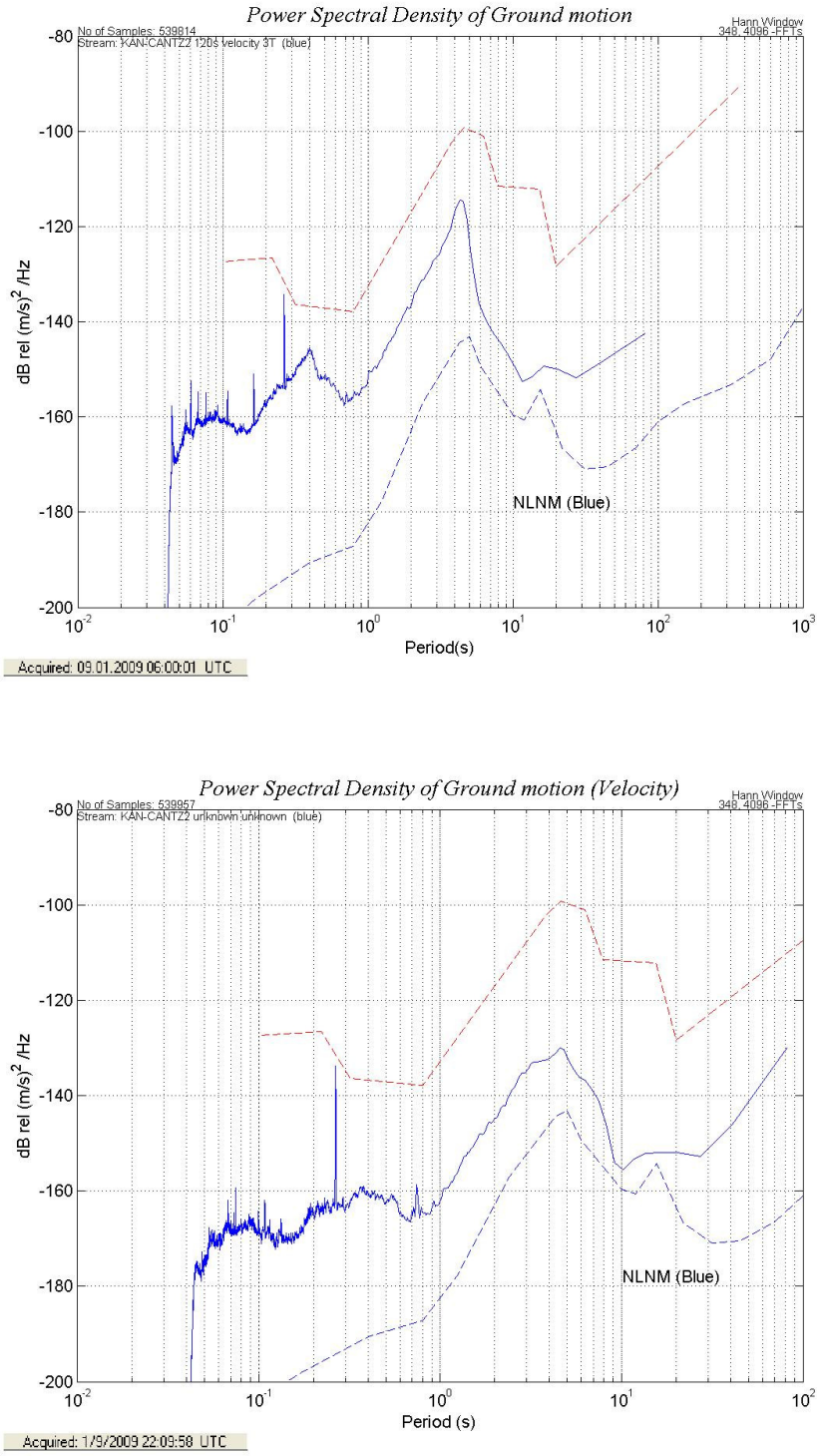

Figure 5.3. Diurnal variations of seismic noise for vertical component of CANT station. Day time (January 9th, 2009, during 06:00-09:00 GMT) variation is indicated above, night time (January 9th, 2009, during, 22:10-01:10 GMT) variation is indicated below

Figure 5.3 shows diurnal variations of seismic noise as a function of period for vertical component of CANT station. The noise level of the day time is close to the NHNM (New High Noise Model) of Peterson (1993) whereas the noise level at night is close to NLNM (New Low Noise Model) of Peterson (1993). For the day time, at longer periods the noise dropped to ~ -152 dB at 28 seconds, then increased to ~ -143 dB through 81 seconds; the microseismic peak is at about -135dB at 0.26 seconds. For the night time, at longer periods the noise dropped to ~ -158 dB at 28 seconds, then increased to ~ -130 dB through 80 seconds; the microseismic peak is at about -133 dB at 0.28 seconds. The noise level is higher in the day time than the night time. The increase and the decrease of the seismic noise are probably due to the cultural noise.

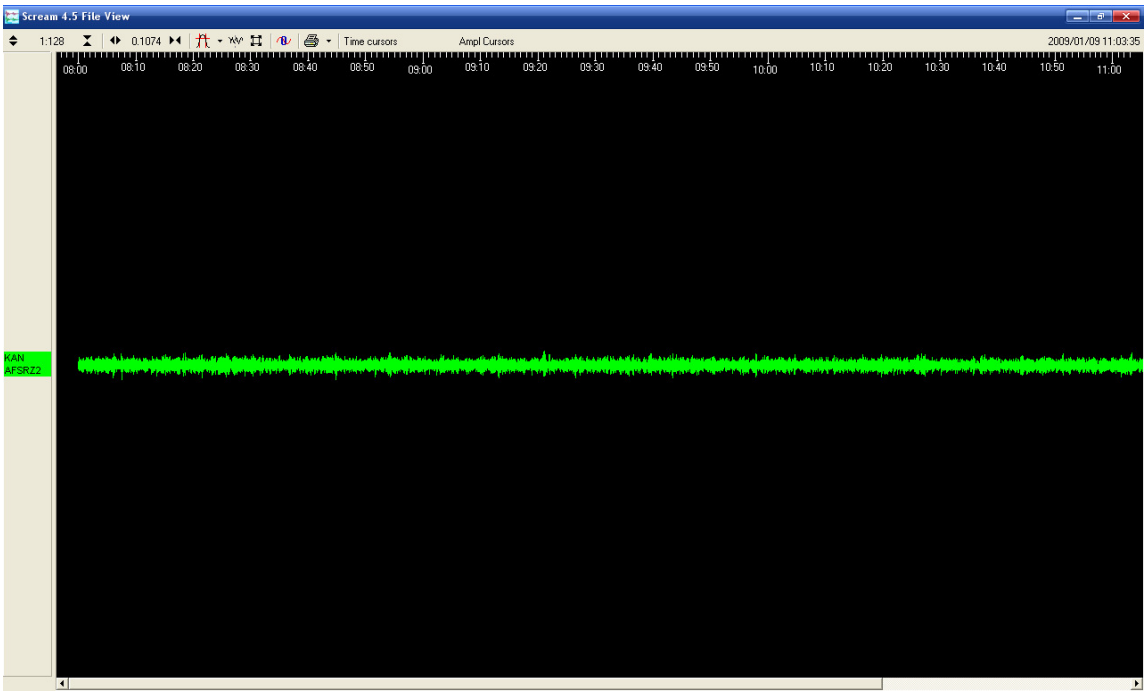

Figure 5.4. Seismic noise record of the vertical component of CANT station on January 9th 2009, during 08:00-11:00

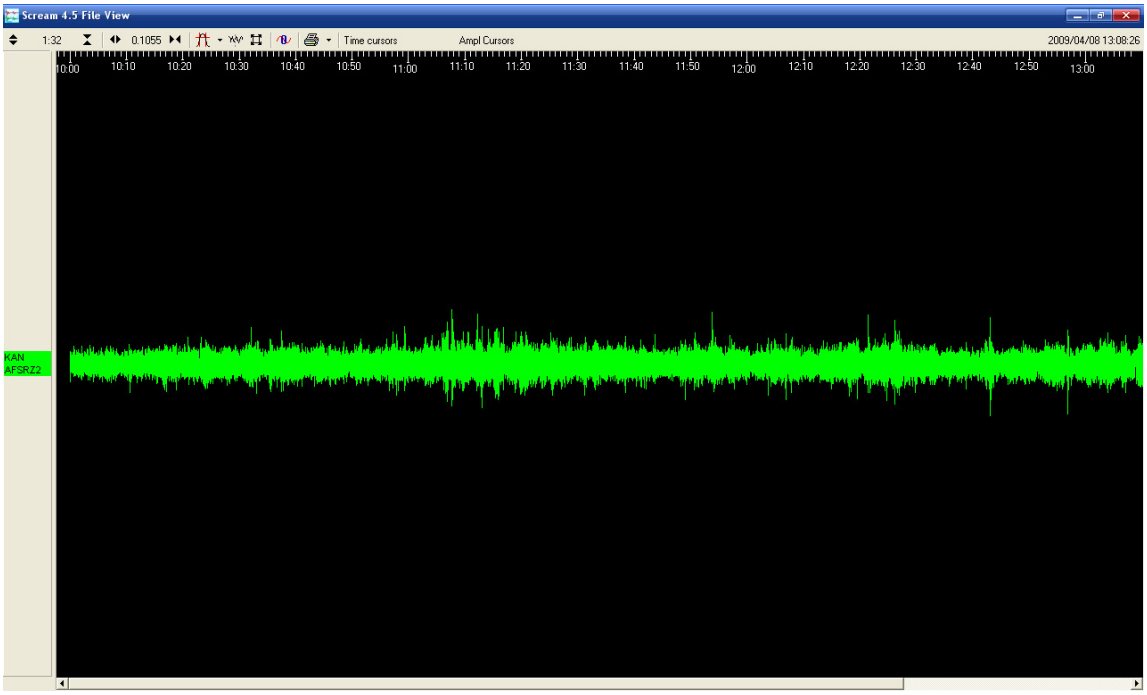

Figure 5.5. Seismic noise record of the vertical component of CANT station on April 8th 2009, during 10:00-13:00 GMT

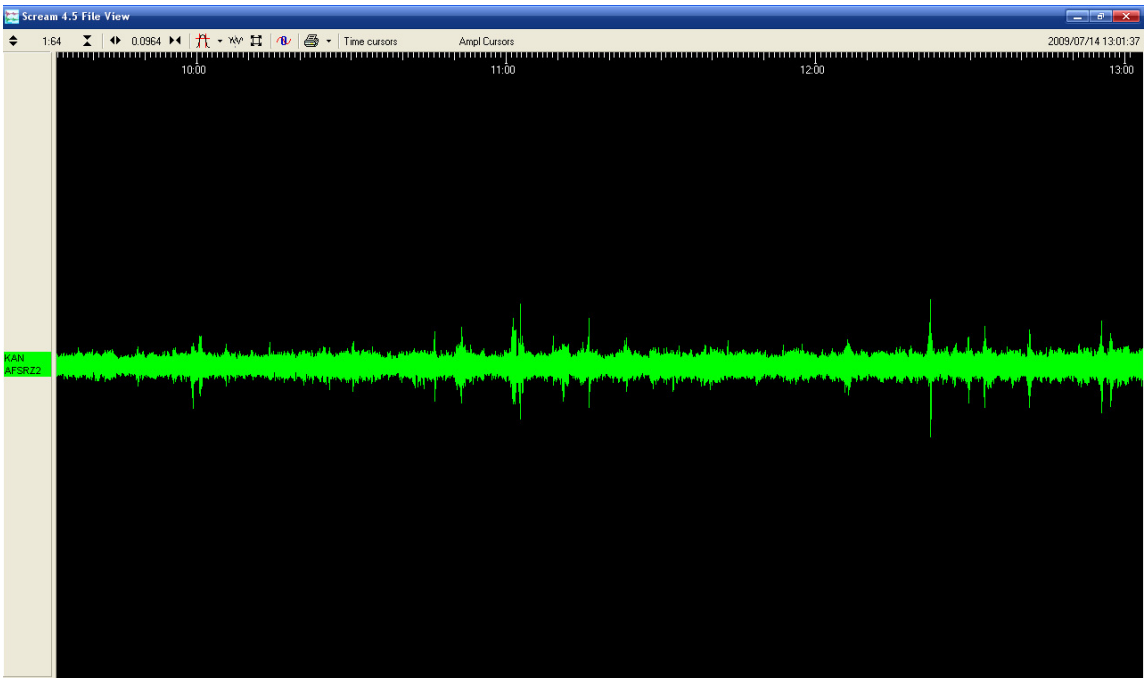

Figure 5.6. Seismic noise record of the vertical component of CANT station on July 14th 2009, during 09:50-12:50 GMT

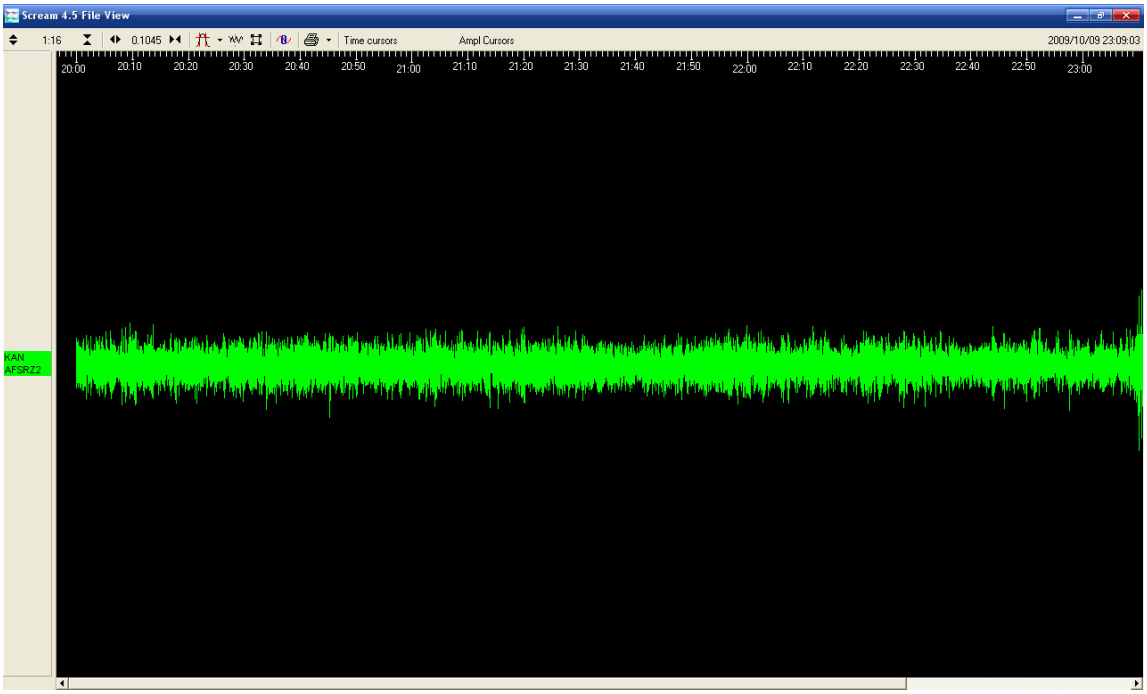

Figure 5.7. Seismic noise record of the vertical component of CANT station on October 9th 2009, during 20:00-23:00 GMT

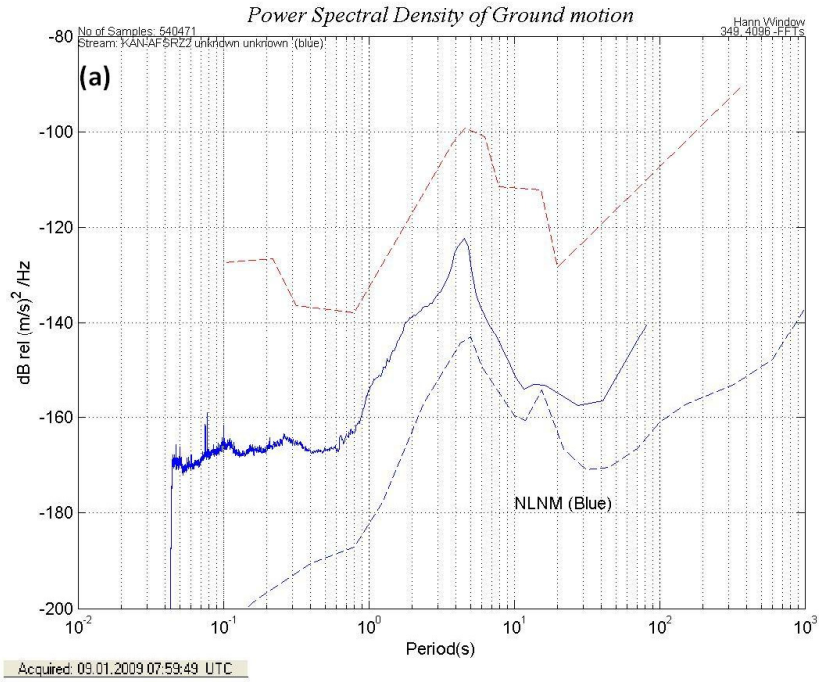
Power Spectral Density of Ground motion
No of Samples: 540471
Stream: KAN-AFSRZ2 unknown unknown '(blue)'
Hann Window
349, 4096 -FFTs
(a)
dB rel (m/s)^2 /Hz
Period(s)
NLNM (Blue)
Acquired: 09.01.2009 07:59:49 UTC

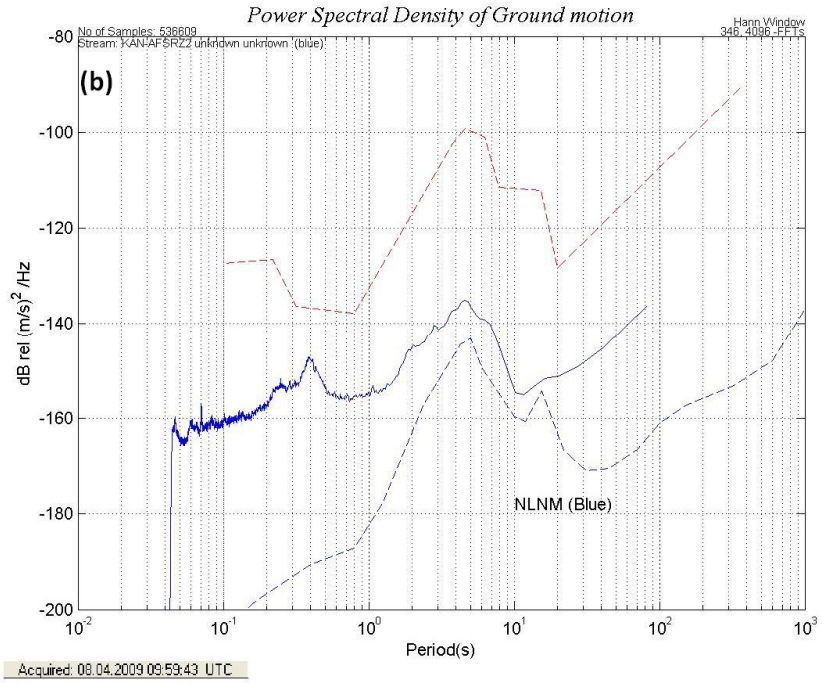
Power Spectral Density of Ground motion
No of Samples: 536609
Stream: KAN-AFSRZ2 unknown unknown '(blue)'
Hann Window
346, 4096 -FFTs
(b)
dB rel (m/s)^2 /Hz
Period(s)
NLNM (Blue)
Acquired: 08.04.2009 09:59:43 UTC

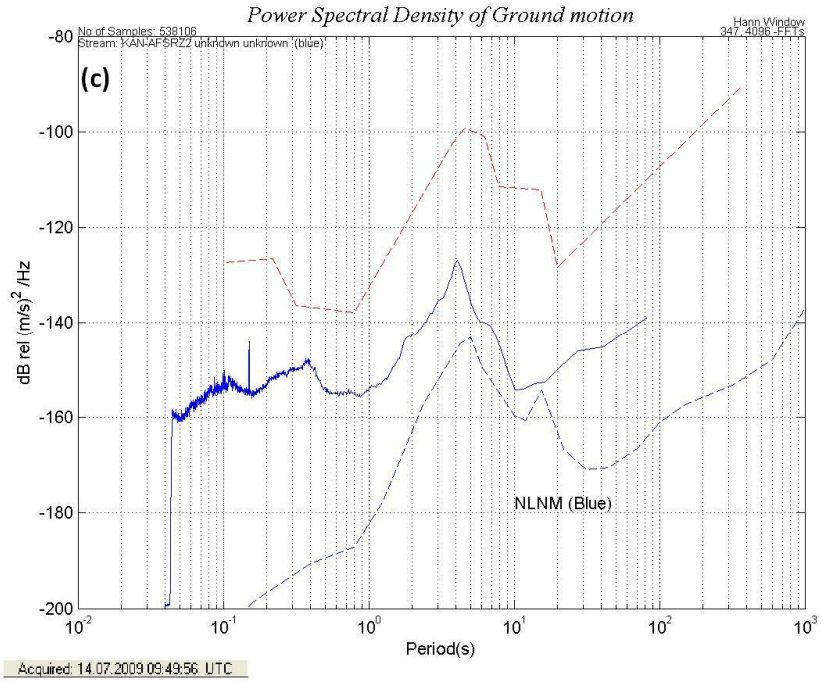

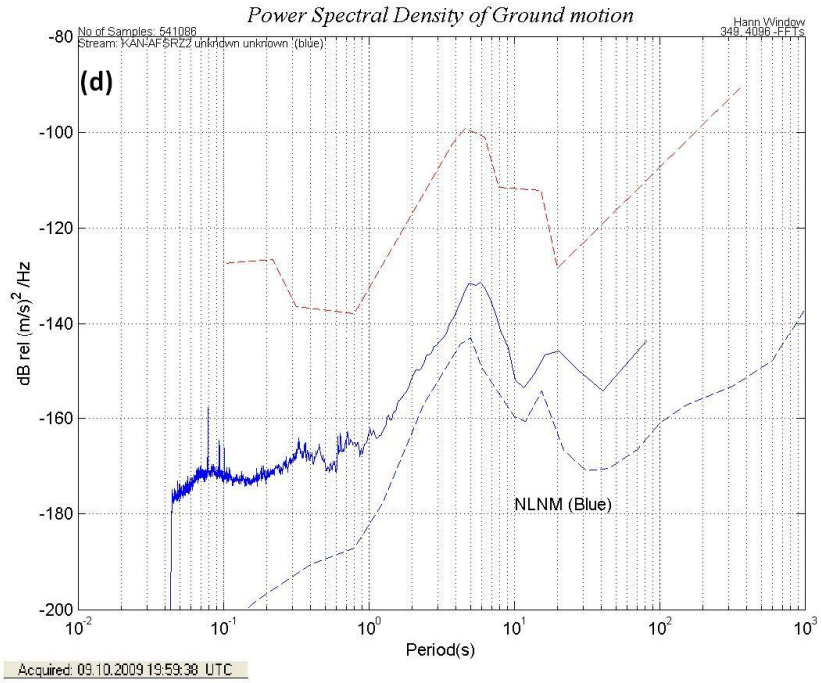

Figure 5.8. Seasonal variations of seismic noise as a function of period for vertical component of AFSR. Variations of January, April, June and October are represented as (a), (b), (c) and (d), respectively

Figure 5.8 shows seasonal variations of seismic noise as a function of period for vertical component of AFSR station. The amplitude of the noise is the highest in winter. In winter, the noise dropped to ~ -156 dB and then incresed to ~ - 140 dB, while the microseismic peak is around -159 dB at 0.08 seconds. In spring, the noise decreased at ~ -154 dB then increased to ~ -136 dB, while the microseismic peak is seen at about -156 dB at ~ 0.075 seconds. In summer, the noise dropped to about –153 dB and then increased to about –141 dB, while the microseismic peak reached at about -144 dB at ~ 0.6 seconds. In fall, the noise decreased to ~ -154 dB then increased to ~ -142 dB, while the microseismic peak is seen at about -158 dB at about 0.08 seconds. The highest noise level in winter is probably due to the intense wind which affects the station.

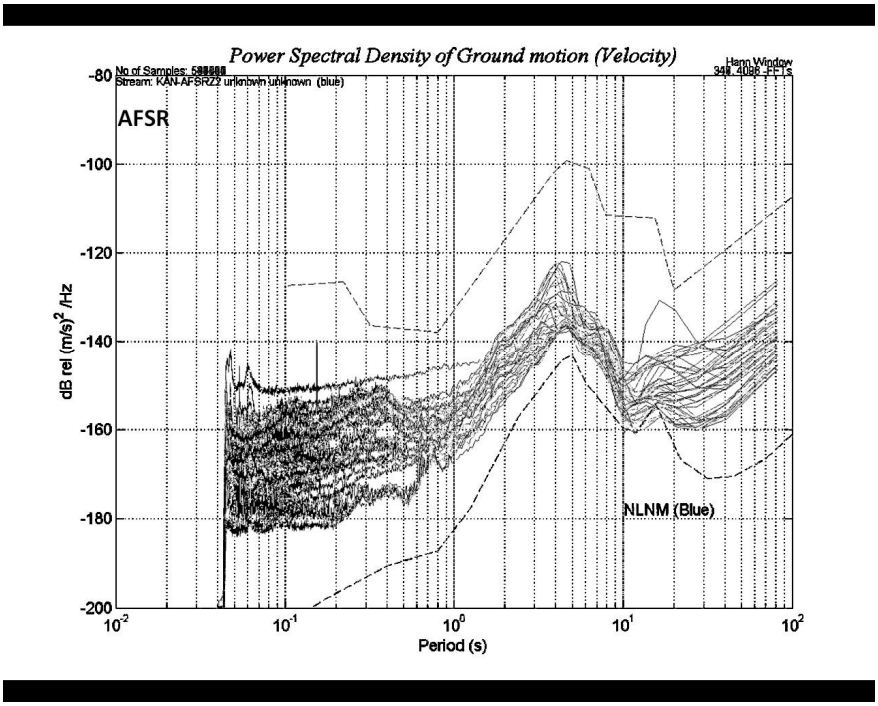

Figure 5.9. 2005-2010 variations of seismic noise as a function of period for vertical component of AFSR

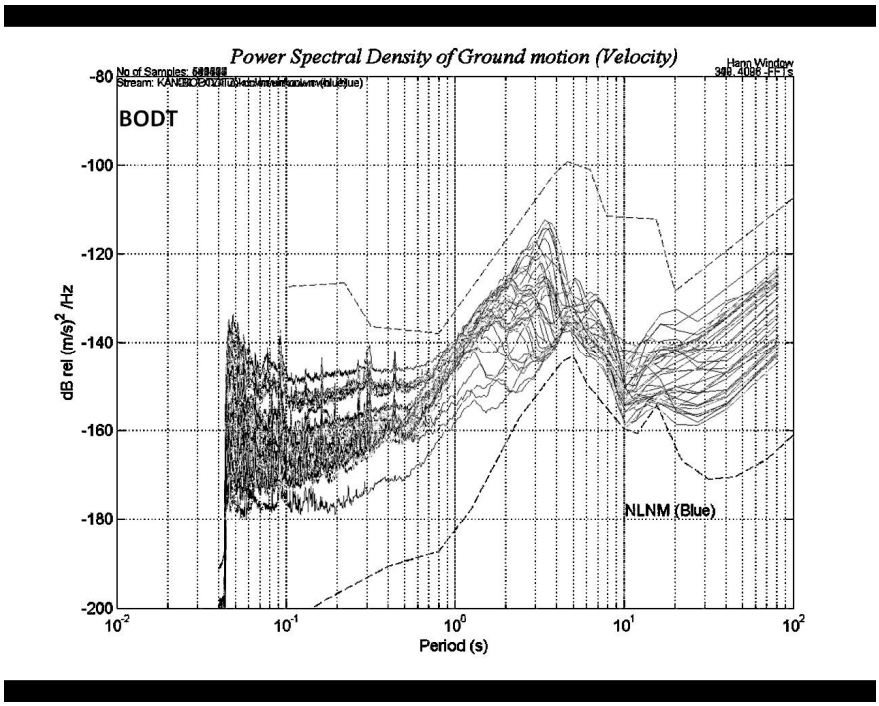

Figure 5.10. 2005-2010 variations of seismic noise as a function of period for vertical component of BODT

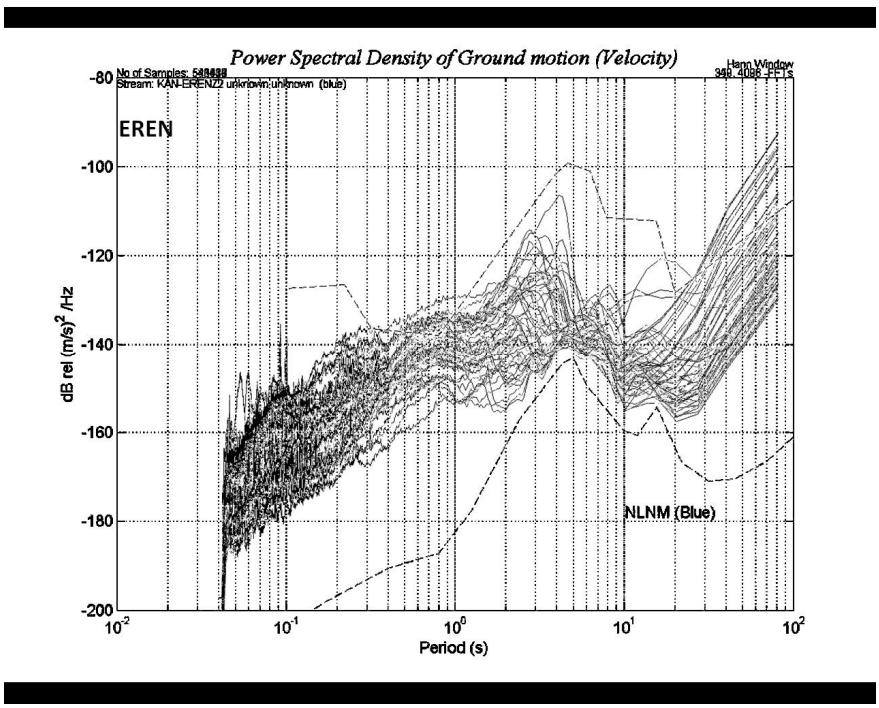

Figure 5.11. 2005-2010 variations of seismic noise as a function of period for vertical component of EREN

For each station, all power spectral density graphs from 2005 to 2010 combined together. Three of them are illustrated above (AFSR, BODT and EREN) (Figure 5.9, 5.10, 5.11). AFSR is a continental station and has the lowest seismic noise. The noise level is close to the NLNM of Peterson (1993) for periods greater than 12 seconds. At shorter periods (below 12 seconds), the noise level at this continental station can vary by 30 dB from one to another. BODT is a coastal station which is located on the continent but near near the coast. It has an intermediate noise level and is similar to AFSR continental station. EREN is an island station which is located on Cyprus and has the highest noise level. The noise level is close to the NHNM of Peterson (1993) for periods greater than 20 seconds. This behaviour is reflecting the fact that island stations are more sensitive to oceanic storms because Rayleigh waves arrive at the stations before being attenuated (Stutzmann *et al.,* 2000).

Figure 5.12 shows the estimated power of the seismic noise for KOERI seismic stations. It was obtained by calculating the mean of the vertical component of the acceleration PSD in the frequency range 1-12 Hz for each station and applying the inverse distance-weighted method (Shepard, 1968) for data grid standardization.

For applying this method, Turkey is gridded with 5 km distances. The mean PSD values were assigned to the intersection points of each 5 km distances. This technique is defined as the 2D moving average method which was applied to the grid to minimize local effects related to the possible bad installations of the stations and to highlight the presence of regional-scale noise characteristics (Shepard, 1968).

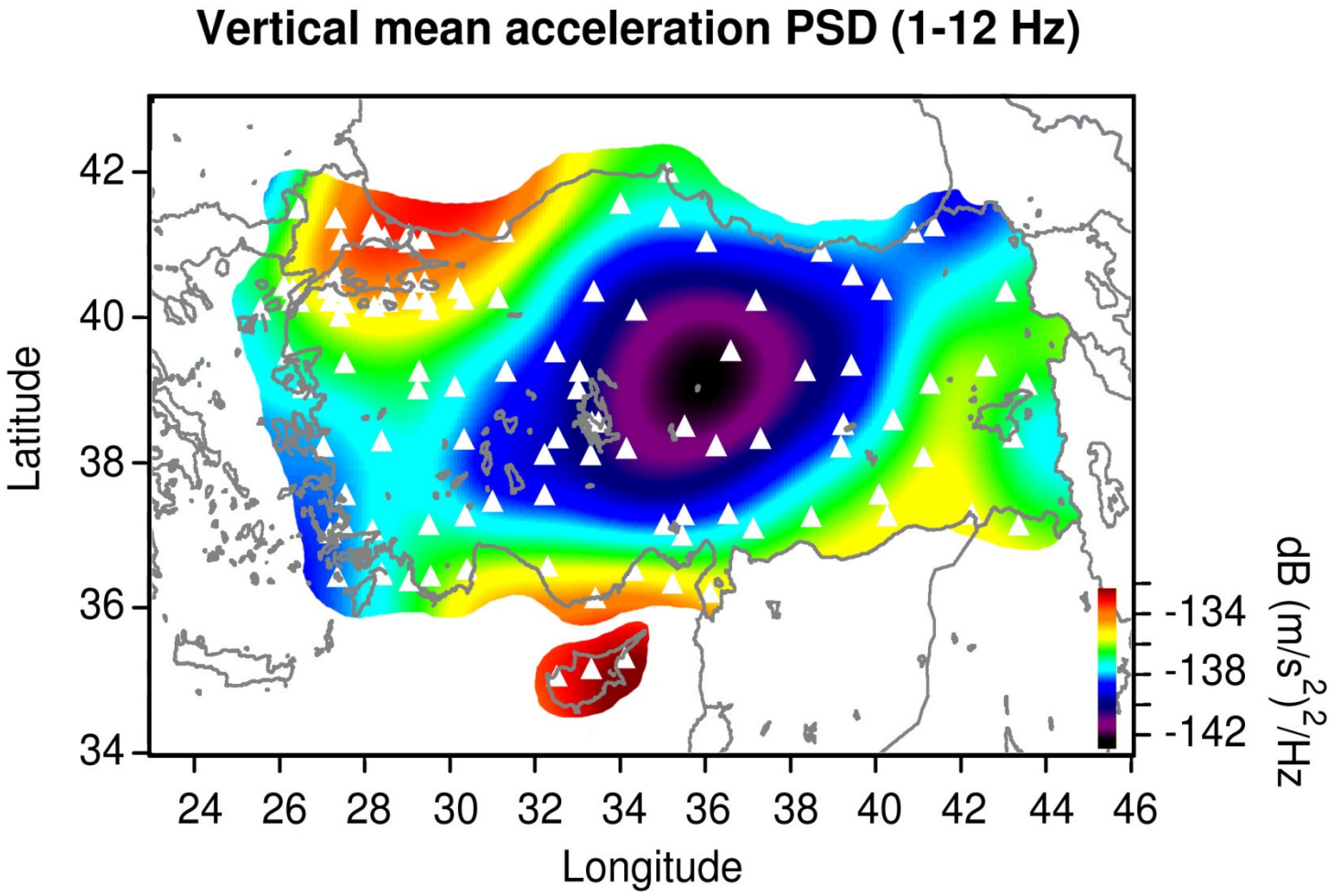

Figure 5.12. Average power of the vertical component noise for KOERI seismic stations

The noise power map in Figure 5.12 shows areas of greater background noise in Istanbul and neighboring cities and Cyprus, whereas lower background noise are seen in Kayseri, Nevşehir, Sivas, Yozgat and Malatya.

Stations with high noise levels around Istanbul are probably associated with the high level of urbanization and the presence of anthropogenic noise. Furthermore, it can be related with the presence of weakly bounded sediments, where the velocity of the seismic waves is low, thus, it can create resonance by amplifying motion at the surface. On the other hand, the high background seismic noise in these regions may associate with the geothermal activity. Likewise, Cyprus island stations with high noise levels are probably a direct result of the geological and geographical nature of the islands. Actually, the seismic stations near the coast or on the islands are generally characterized by a high level of seismic noise due to the water movement (McCreery, 1993).

The low noise of the stations in Kayseri and surrounding regions can be associated with the low urbanization and with the solid rocks which they are made of volcanic rocks. Although there are two important volcanoes in these regions, the lack of noise can be based on the absence of volcano-seismic activity.

5.2. Estimation of the Residual Time Variance

An earthquake is characterized by its hypocentral parameters (its origin time T_0 and position x_0, y_0, z_0) and associated uncertainties (σ_T, σ_x, σ_y, σ_z). Hypocentral parameters are obtained by inversion of the arrival times of seismic phases read on seismograms (D'Alessandro *et al.,* 2001). "The finest way of the estimation of the focal parameters is to determine in an iterative mode by minimizing the Euclidean norm of the residual travel times: $\Delta T = T_{obs} - T_{cal}$, where T_{obs} is the time read on the seismogram and T_{cal} is the calculated travel time. The error in reading the seismic phase can be thought random, so the sign of ΔT on seismic rays that have travelled the same volume can give information about the existence of regions with above (+) or below (-) average velocity than those of the Earth model used. Meanwhile, the important variable in the error analysis is the arrival-time variance $\sigma^2_{\Delta T}$" (D'Alessandro *et al.,* 2001) In general, this value is greater

than would be expected from timing and picking errors alone and can be assigned with the inappropriateness of the velocity model used in the hypocenter location procedure or with the velocity anisotropy (Rothman *et al.,* 1974).

"The theoretical separation of the two terms of Equation (3.8) may be difficult to apply" (D'Alessandro *et al.,* 2001). At this time, an empirical law that links the variance of the residual time to the hypocentral distance was estimated. For this reason, two different residual time versus hypocentral distance data bases were created by using P and S arrival times related to the earthquakes located by BU-KOERI-NEMC between 2005 and 2010. A total of more than 25000 residual time-hypocentral distance pairs were used to generate the 2D color histograms in Figure 5.13. For their construction, groups of 0.05 s and 10 km were used for the residual time and hypocentral distances, respectively.

The variances of the residual times are up to the maximum hypocentral distance of 780 km and 250 km for P and S phases, respectively, were calculated for each distance group. On the further sides of these values correspond to the lack of data which made the estimates unimportant.

The data variance estimates were fitted with polynomial functions by using the statistical criteria. The solution shows a good adhesion to the observed data when the polynomial degree (or the complexity) increases. But also it shows a good adherence to the related component of random error (D'Alessandro *et al.,* 2001).

"The behavior of the solution related to the variation in complexity can be studied through slope and variance. Slope, measures the deviation from the mean estimate of the optimal estimator and variance measures the stability of the estimator with respect to the observed data" (D'Alessandro *et al.,* 2001). In general, while complexity increases, slope decreases whereas variance increases (Hastie *et al.,* 2008).

For balancing these two quantities and determining the complexity of the optimal model, the expected or generalization error was predicted. For P and S phases, fifth and fourth orders of the polynomials were determined so as to minimize this error.

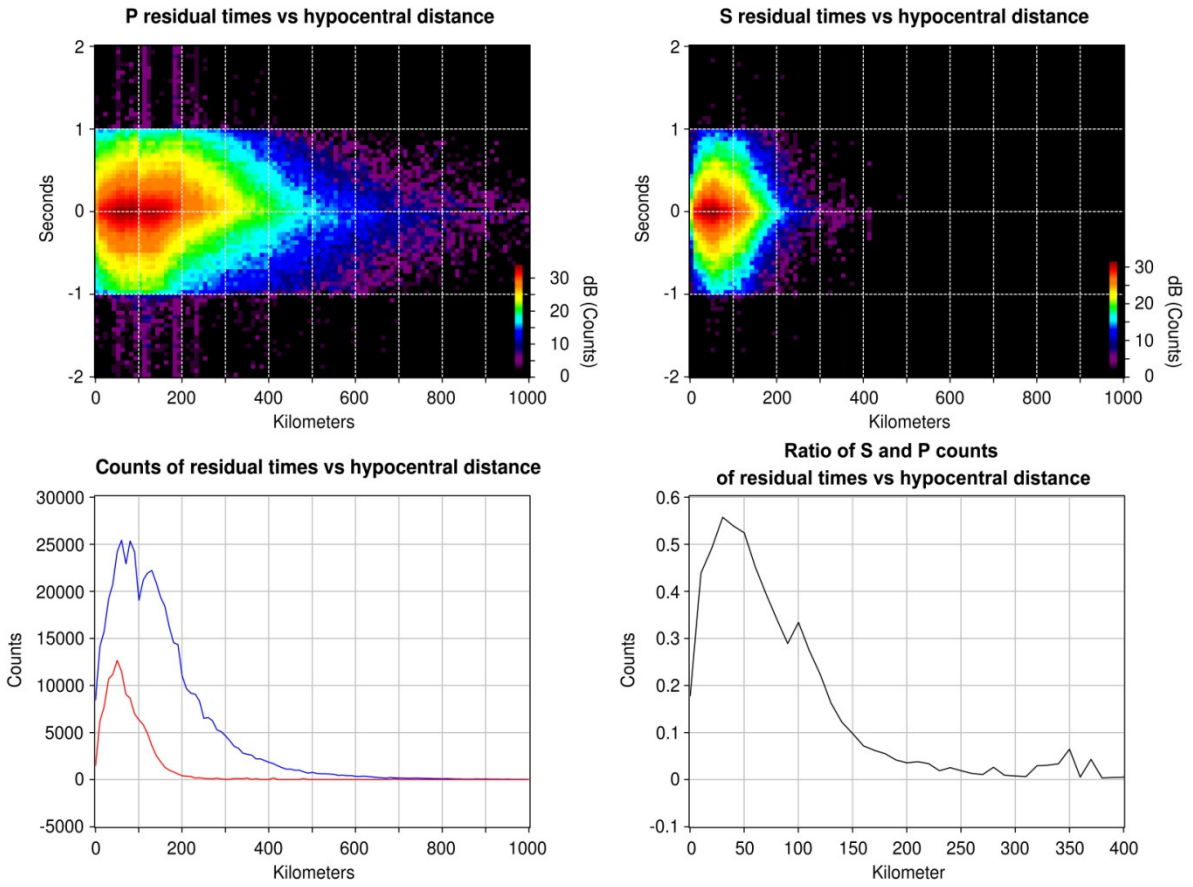

Figure 5.13. 2D histograms of P and S residual time versus hypocentral distance in logarithmic color scale are illustrated above. The number of P (blue line) and S (red line) residual times from local and regional earthquakes and their ratios are illustrated below

Figure 5.13, shows the 2D histograms of P and S residual times, P and S residual time counts and S/P count ratios as a function of hypocentral distance. The 2D histograms are nearly symmetric. "The spread in the residual time histograms can be modeled as the sum of random scatter in the times due to picking errors and systematic travel-time difference because of the lateral heterogeneity" (D'Alessandro *et al.,* 2001).

S phase counts have the maximum between 50 and 55 km whereas P phase counts have two maxima between 50-75 km and 75-100 km. The count ratio S/P shows an inverse relation to the hypocentral distance. This ratio reaches a maximum value of 0.56 at small hypocentral distances and decreases rapidly with the hypocentral distance, falling below 0.1 for hypocentral distances greater than 150 km.

"Using seismic phases with different velocities brings about better determination of hypocenter. So, in general, it is favorable to use multiple phases for each seismic station, supposing that the phases are identified correctly. The S_g phases contribute to the location process importantly whereas S_n phases contribute insignificantly" (D'Alessandro *et al.,* 2001).

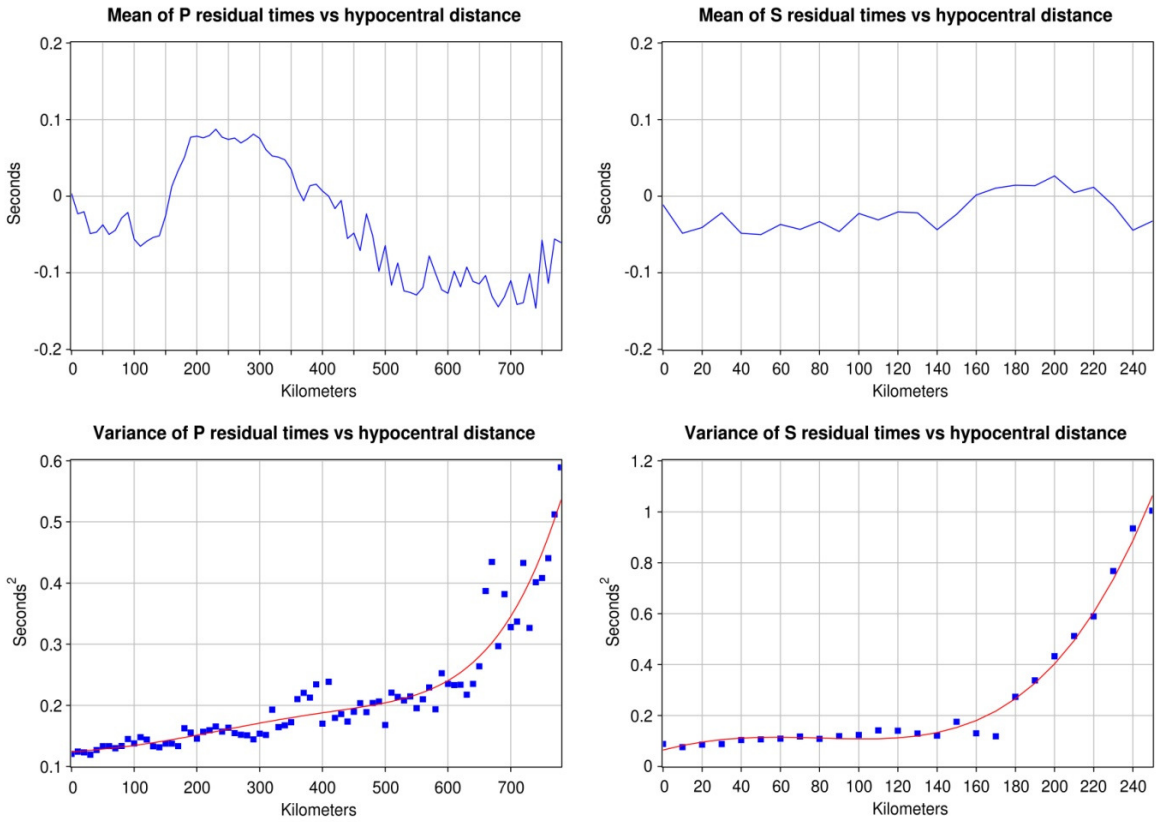

Figure 5.14. Above: Mean P phase and S phase residual times as a function of hypocentral distance. Below: Blue squares represent the variance of P and S phase residual times as a function of hypocentral distance; red curves illustrates polynomial fits to residual data

Figure 5.14 shows the mean and the variance of the residual times of the P and S phases as a function of hypocentral distance. The average P phase residual times show small and mostly negative values. This behavior is probably related to the P wave velocity model used in the location procedure which is faster than the real P wave velocity of the Earth (The most common global 1-D Earth model NMSOP-91 assumes the average

velocities for the upper and lower crust are for P waves 5.8 km/s, 6.5 km/s, and for S waves 3.36 km/s, 3.75 km/s, respectively). The average S phase residual times show a similar trend to that of the P phases. It takes negative values for hypocentral distances less than 160 km and more than 225 km and positive values are within this range. This behavior is probably related to the S velocity model which is faster in surface than the real S wave velocity model. Both P and S velocity models are required to be optimized. The values of the residual times that move away from zero introduce the systematic errors in hypocenter location.

$$\sigma^2_P = 8.547 \cdot 10^{-15} x^5 - 9.550 \cdot 10^{-12} x^4 + 3.069 \cdot 10^{-9} x^3 - 8.432 \cdot 10^{-8} x^2 + 9.559 \cdot 10^{-5} x + 1.232 \cdot 10^{-1} \quad (5.1)$$

$$\sigma^2_S = 3.263 \cdot 10^{-10} x^4 + 4.361 \cdot 10^{-8} x^3 - 2.336 \cdot 10^{-5} x^2 + 2.006 \cdot 10^{-3} x + 6.432 \cdot 10^{-2} \quad (5.2)$$

Equation (5.1) and Equation (5.2) demonstrate the fifth and fourth orders of the polynomials, determined by polynomial regression for the variance in the residual times of the P and S phases, respectively and are graphed in Figure 5.13.

It is assumed that σ^2_{SNR} is an unimportant value so Equations (5.1) and (5.2) can be defined in terms of σ^2_{MOD}. As hypocentral distance increase, both σ^2_P and σ^2_S grow rapidly, seen in Figure 5.14.

The law that defines σ^2_P as a function of hypocentral distance is explained by a fifth order polynomial function (Equation 5.1). Its growth varies for different hypocentral distance intervals. At hypocentral distances of less than about 500 km, the σ^2_P shows an almost linear upward trend. The first arrival phase has travelled mainly within the crust, in this interval. This trend of σ^2_P can be confirmed by the geological complexity of the crust in the Turkish territory and the resulting velocity heterogeneity. For hypocentral distances greater than about 500 km, σ^2_P begins to grow rapidly. This behavior is due to the inappropriateness, in its deep part, of the 1D velocity model used by BU-KOERI in the hypocenter location procedure. Therefore, it is clearly seen from upward motion of the variance that the crust is heterogeneous. If the variance tends to stabilize at an interval, it can be said that that layer is more homogeneous than the crust or the other layers.

The law that defines σ^2_S as a function of hypocentral distance is explained by a fourth order polynomial function (Equation 5.2). The σ^2_S reaches higher values than σ^2_P, however, it is nearly stable at hypocentral distances of less than about 140 km. For hypocentral distances greater than 140 km, it begins to grow exponentially.

On the other hand, Equation (5.1) and Equation (5.2) can be used to estimate the variance of the residual times for each station of the seismic network.

5.3. Earthquake Simulation: Seismic Spectra Calculation

It is essential to define an appropriate source and velocity and attenuation models to estimate for a particular magnitude and hypocenter position (D'Alessandro *et al.,* 2001). For this reason, the Brune source model was used in order to calculate the seismic spectra at the receiver.

One-dimensional velocity model constituted by BU-KOERI-NEMC was used in the hypocenter location routine to make the simulation of earthquakes. P wave velocities range between 4.5-5.91 km/s in 5.4 km thickness and between 5.91-7.8 km/s in 31.6 km thickness.

Table 5.1. The velocity model of Turkey used by KOERI (Kalafat *et al.,* 1987)

Vp (km/sec)	Depth (km)
4.500	0.000
5.910	5.400
7.800	31.600
8.300	89.200

The values of S wave velocity and density (ρ) used in the spectra calculation were estimated by using the empirical relationships of Brocher (2005).

$$Vs\ (km/s) = 0.7858 - 1.2344Vp + 0.7949Vp^2 - 0.1238Vp^3 + 0.0064Vp^4 \qquad (5.3)$$

Equation (5.3) is valid for $1.5 < Vp < 8$ km/sec.

$$\rho\ (g/cm^3) = 1.6612Vp - 0.4721Vp^2 + 0.0671Vp^3 - 0.0043Vp^4 + 0.000106Vp^5 \qquad (5.4)$$

Equation 5.4 is called the Nafe-Drake curve and is valid for $1.5 < Vp < 8.5$ km/sec (Ludwig *et al.,* 1970).

Table 5.2. Empirical Vp, Vs and density relations

Vp (km/sec)	Vs (km/sec)	Density (g/cm^3)
4.50	2.67	2.45
5.91	3.51	2.70
7.80	4.46	3.22
8.30	4.89	3.40

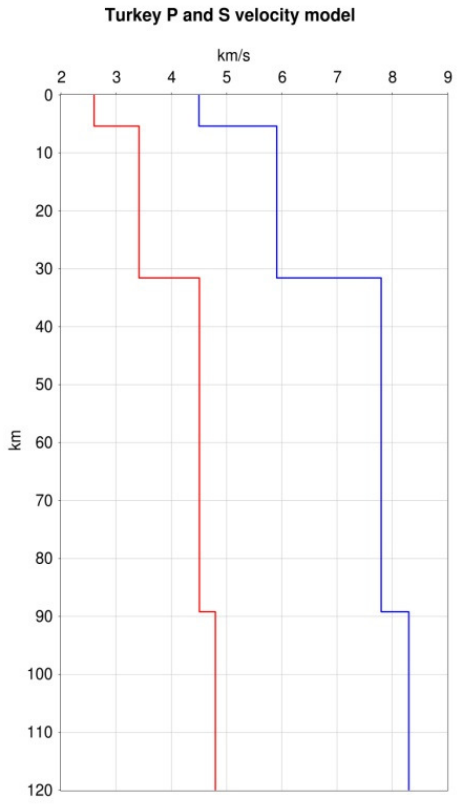

Figure 5.15. 1D P wave and S wave velocity model of Turkey (Blue line represents the P wave velocity; red line represents the S wave velocity)

The equations expressed in Chapter 3.3 are used to calculate the seismic spectra for the 1D velocity model used by BU-KOERI in the earthquake location procedure.

P wave attenuation law proposed by Bindi *et al.,* (2006) for Turkey has been used. Bindi *et al.,* (2006) obtained the relation $Q_p = 56\ f^{0.25}$ for $2.5 \leq f \leq 10$, with the magnitudes for earthquakes between 1 and 4.5, most of them have a source depth between 5 and 15 km and the hypocentral distances range from 10 to 142 km. In general, the near surface attenuation (δ) is expressed in a typical value 0.05 s^{-1} (Havskov and Ottemöller, 2010).

For the calculation of the seismic spectra, the hypocentral depth was fixed at 10 km, assigned the values $\alpha = 5.9$ km/s, $\Delta\sigma = 6$ MPa, $R_p = 0.55$, $V_c = 0.9\beta$, $k = 3.36$ and $\delta = 0.05$ s^{-1} to the parameters of the algorithm written in Chapter 3.3.

The seismic spectra of 20,259 real earthquakes located by BU-KOERI, were estimated to check the goodness of the source model. Earthquakes with M_L 2.5, 3.0, 3.5 and the epicentral distance between 0 and 300 km were selected for evaluating the location performance of BU-KOERI seismic stations.

For different magnitude and epicentral distances, the estimated velocity PSDs of the vertical component of the noise, including all seismic stations from 2005 to 2010, were combined together and plotted (Figure 5.16) by using the velocity model and the attenuation law described above. In order to make a comparison, the reference velocity PSDs of the vertical component of noise (NHNM and NLNM, Peterson, 1993) were also plotted.

Figure 5.16 shows all velocity PSD of the vertical component of noise accommodated in the Peterson (1993) reference NHN and NLN models. It also demonstrates that the signal-to-noise ratio is a function of the magnitude and epicentral distance of the level noise found at the station (D'Alessandro *et al.,* 2001).

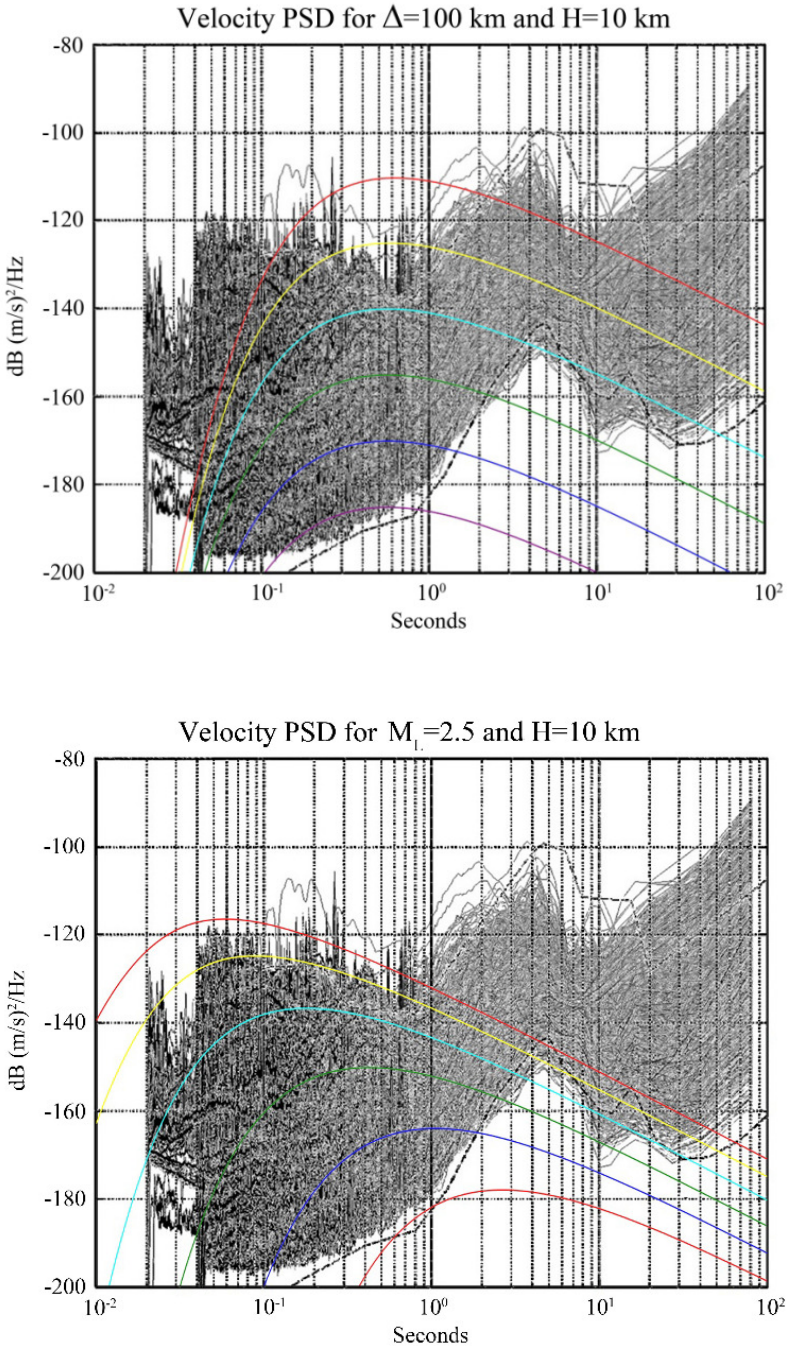

Figure 5.16. Above: PSDs for the fixed epicentral distance 100 km and varying the magnitude (violet: M_L 1.5, blue 2.0, green: 2.5, cyan: 3.0, yellow: 3.5, red: 4.0). Below: the magnitude was fixed at 2.5 and varying the epicentral distance (violet: Δ = 320 km, blue: 160 km, green: 80 km, cyan: 40 km, yellow: 20 km, red: 10 km)

It can be seen from the left side of the Figure 5.16 that, KOERI seismic stations are successfully capable of detecting earthquakes with the magnitude 4.0 at the epicentral distance of 100 km and hypocentral distance of 10 km. The detection capability is insufficient for earthquakes with 3.5, 3.0, 2.5, 2.0 and 1.5 magnitudes for the epicentral and hypocentral distances of 100 km and 10 km, respectively.

Similarly, it can be said from the right of the Figure 5.16 that when the epicentral distance is 10 km, the seismic stations can detect earthquakes with magnitude 2.5 well enough with the hypocentral distance of 10 km. The detection capability is insufficient for the epicentral distances 20, 40, 80, 160 and 320 km with the magnitude 2.5.

5.4. Location Performance of KOERI Seismic Stations

The location performance of KOERI seismic stations was investigated for magnitudes M_L = 2.5, 3.0 and 3.5 by fixing the hypocentral depth at 10 km. The confidence level of the hypocentral parameter estimates at P = 95 per cent. The threshold of 95 per cent of the acceleration PSD of the vertical component PSD_S was estimated for each station to calculate WSR (Wide spectral ratio) in the frequency range 1-12 Hz, typical of the seismic phases of events

$$\mathrm{WSR}_{(1-12\ \mathrm{Hz})} = 10\ \mathrm{Log}_{10}\left(\frac{\int_1^{12}\mathrm{PSD_E}\ \mathrm{df}}{\int_1^{12}\mathrm{PSD_S}\ \mathrm{df}}\right) \tag{5.5}$$

where PSD_E is the power spectra of the theoretical P phase. Stations with WSR>10 were considered to be active in the location routine. After determining the active stations with useful P phases for the location procedure, the corresponding S phases were added only for those stations having higher WSR to identify the average ratio P phase number / S phase number equal to that determined for the seismic catalogue of BU-KOERI-NEMC.

The area was gridded by using a square mesh having equal sides with 5 km, while the SNES maps were calculated for amplitude confidence intervals at 95 per cent of the hypocentral parameter estimate. Uncertainties in the focus parameters were represented up

to 2 s and 10 km for the origin times and hypocentral coordinates, respectively. To smooth the maps and reduce the random noise, a 2D moving average with square windows having 5 km per side was employed with the application of a cubic 2D spline insertion to improve the graphics. The results of the SNES maps are given in the following chapter.

6. RESULTS

In this study, the SNES method was applied to BU-KOERI seismic stations to assess and measure its performance for locating local and regional seismicity. Furthermore, it allows to specifying seismogenic areas on the Turkish territory which are not covered adequately.

Figures from 6.1 to 6.11 show the SNES maps which were constructed for magnitudes M_L 2.5, 3.0 and 3.5. Each SNES map was divided into six sub-maps that introduce the number of active stations, the azimuthal gaps and the amplitude of the confidence interval of the origin time, latitude, longitude and hypocentral depth.

Figure 6.10 and 6.11 show the hypocentral position uncertainty map and the M_c map determined with the SNES method. The hypocentral position uncertainty maps were calculated as RES (radius of equivalent sphere) of the 95 per cent confidence ellipsoid whereas the M_c map was obtained by considering earthquakes for magnitudes M_L 2.5, 3.5, 4.5, 5.5+.

The SNES maps show that earthquakes with the magnitude M_L 2.5 are recorded by no more than a dozen of stations. The azimuthal gap does not fall below 100° and the error in origin time is 3.8 seconds. Most of the Turkish territory is not well covered, including Cyprus. Only few areas which are southeast of Marmara Sea and Gulf of Gökova covered with expected errors in epicentral and hypocentral depth prediction do not fall below 3 km and 5.5 km, respectively.

For M_L 3, the maximum number of stations increases to 20, while the azimuthal gap reaches about 60° and the origin time error reaches about 2 seconds. The coverage of Turkish peninsula for M_L 3 is better than the coverage of M_L 2.5 but it is clearly seen that there are still many areas that are not covered well. The errors in epicentral and hypocentral estimate drop to 2 km and 4 km, respectively. The quality of the epicentral estimate is better in Marmara Region and the hypocentral depth error is lower particularly in southwest corner of Marmara Sea.

For M_L 3.5, the maximum number of stations exceeds 28, while the azimuthal gap drops about to 40° and the origin time error falls below 2 seconds. In the central and some sothern parts of Marmara Sea, the errors in epicentral and hypocentral estimate are 2 km and 3 km, respectively. For this magnitude, almost the entire Turkish territory, except the coast of Black Sea Region, the eastern boundary of Turkey and the south part of Southeastern Anatolia Region, is well covered. A few parts of Black Sea Region and some parts of Aegean Sea and Mediterranean Sea are also covered.

The SNES maps indicate a direct relationship with the magnitude and the area. As the magnitude increases, the enlargement in the coverage of the area increases too. The direct relationship is also valid for the quality of the location. Moreover, when the magnitude goes up from M_L 3.0 to M_L 3.5, only the error in the epicentral estimate tends to stabilize. In better covered areas, error does not fall below 1.5 km for the epicenter and below 3 km for the hypocentral depth.

For most of the Turkish territory, the estimated error in longitude is less than the estimated latitude error. This behavior is unquestionably related with an imbalanced distribution of the seismic stations due to the shape of the peninsula.

M_L 2.5

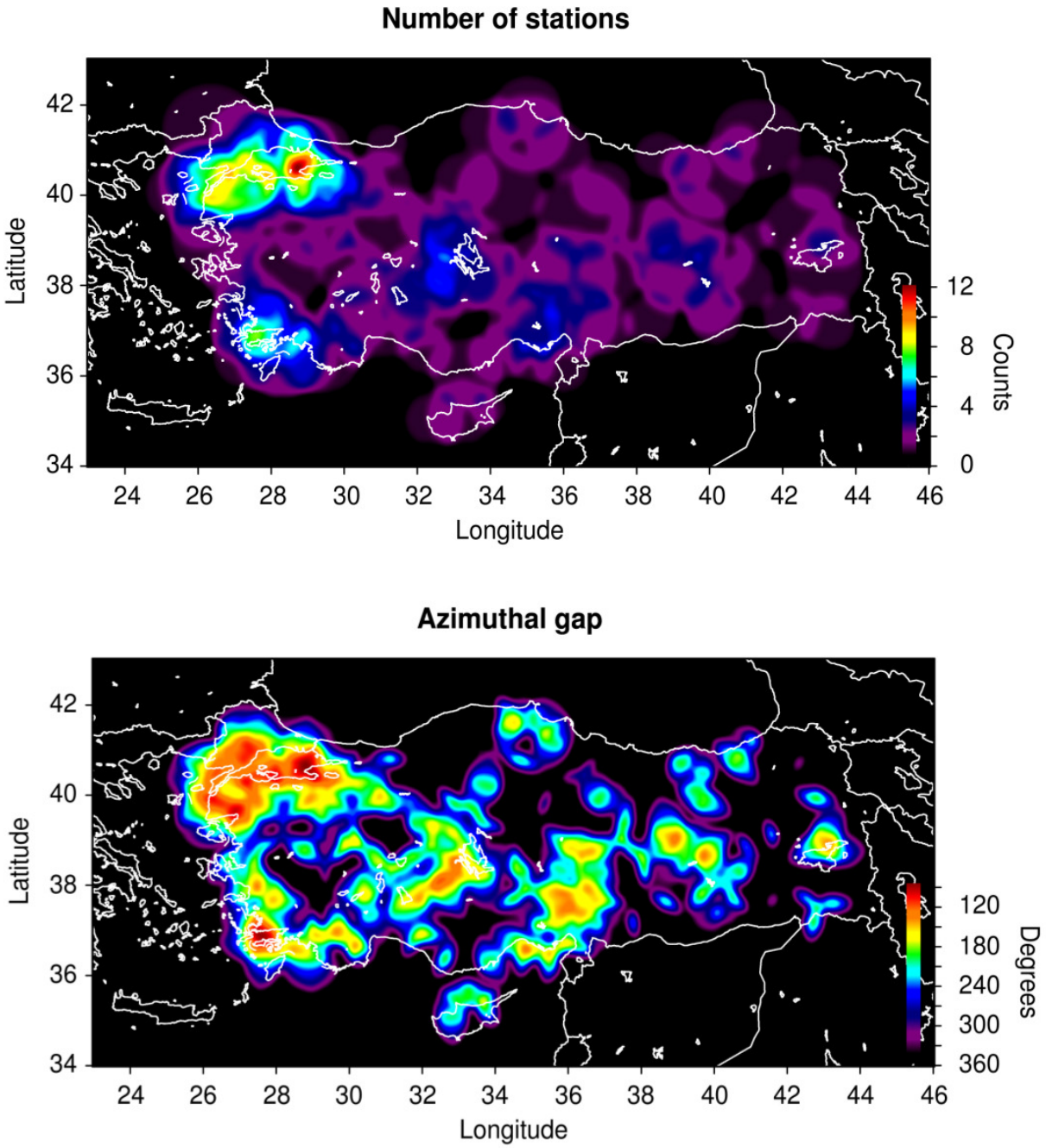

Figure 6.1. SNES maps of number of stations and azimuthal gap for M_L 2.5, H = 10 km and confidence level of 95 per cent. Events with a magnitude of 2.5 are recorded by a dozen stations and the minimum azimuthal gap is 90°

M_L 2.5

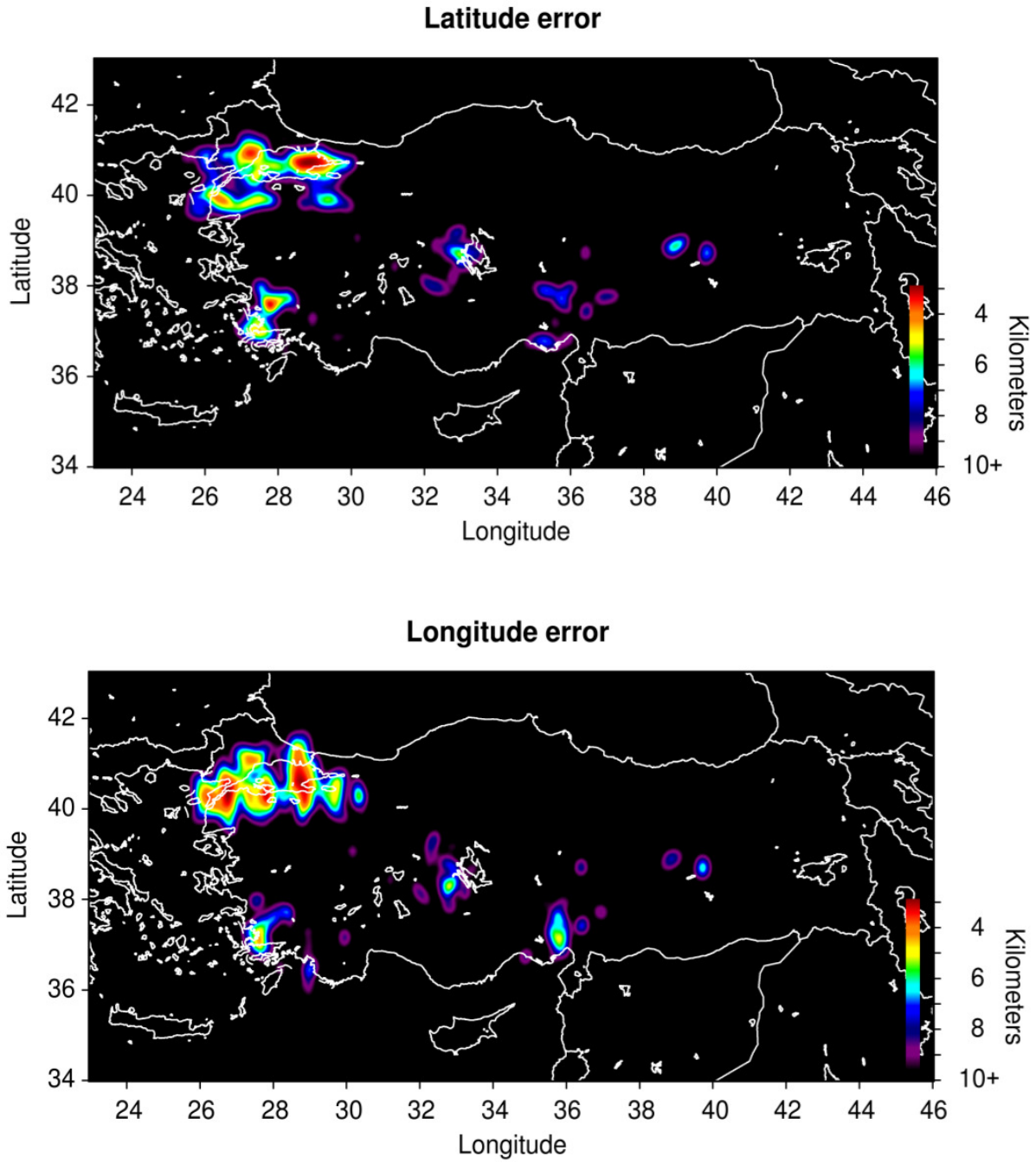

Figure 6.2. SNES maps of latitude and longitude error for M_L 2.5, H = 10 km and confidence level of 95 per cent. Some areas of Marmara Sea are covered with expected errors in epicentral prediction which do not fall below 3 km

M_L 2.5

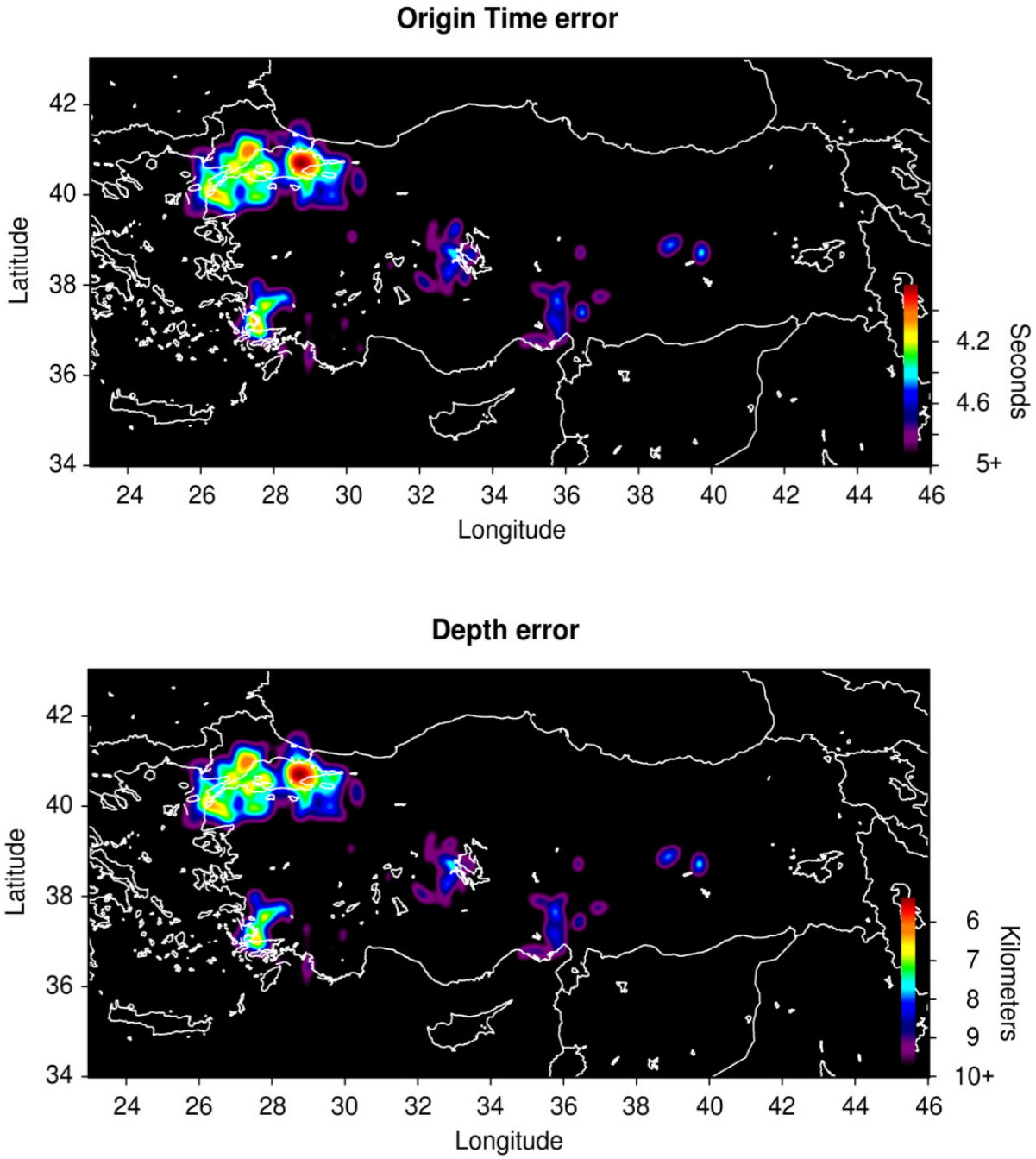

Figure 6.3. SNES maps of origin time error and depth error for M_L 2.5, H = 10 km and confidence level of 95 per cent. The error in origin time is about 3.8 seconds. East part of Marmara Sea is covered with expected errors in hypocentral depth prediction which do not fall below 5.5 km

M_L 3.0

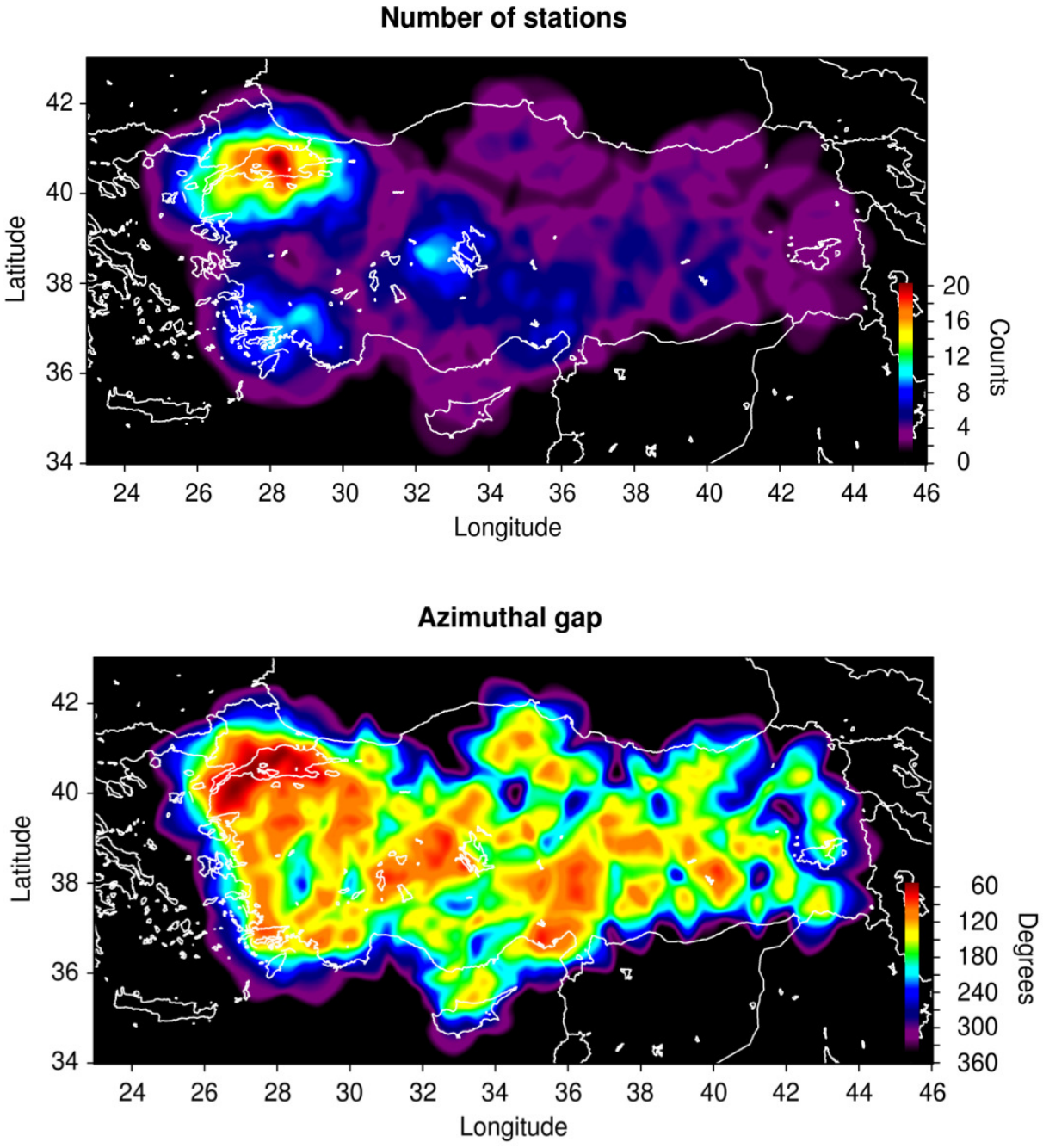

Figure 6.4. SNES maps of number of stations and azimuthal gap for M_L 3.0, H = 10 km and confidence level of 95 per cent. The maximum number of stations increases to just 20, while the minimum azimuthal gap reaches about 60°

M_L 3.0

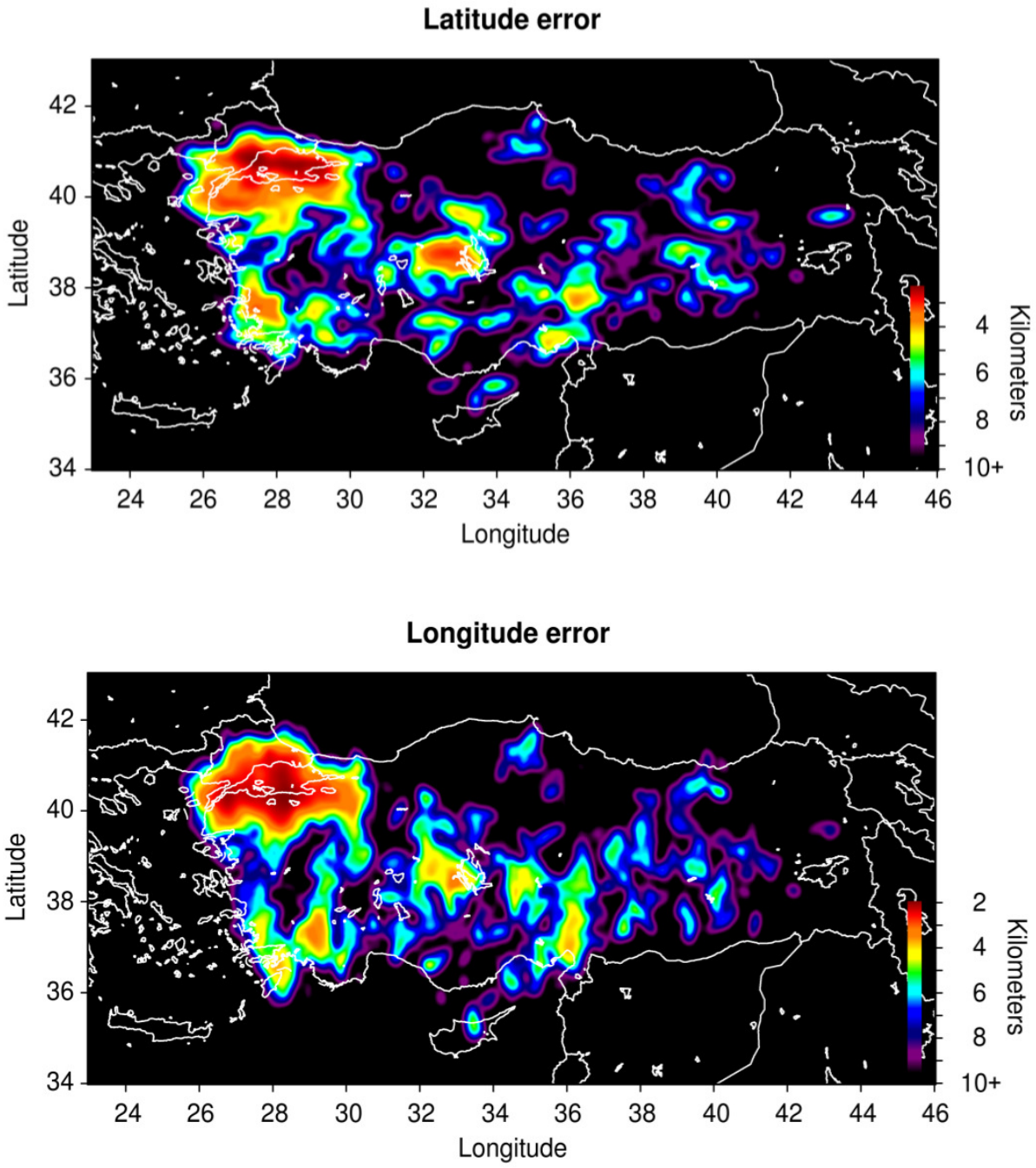

Figure 6.5. SNES maps of latitude and longitude error for M_L 3.0, H = 10 km and confidence level of 95 per cent. The errors in epicentral estimate drop to 2 km

M_L 3.0

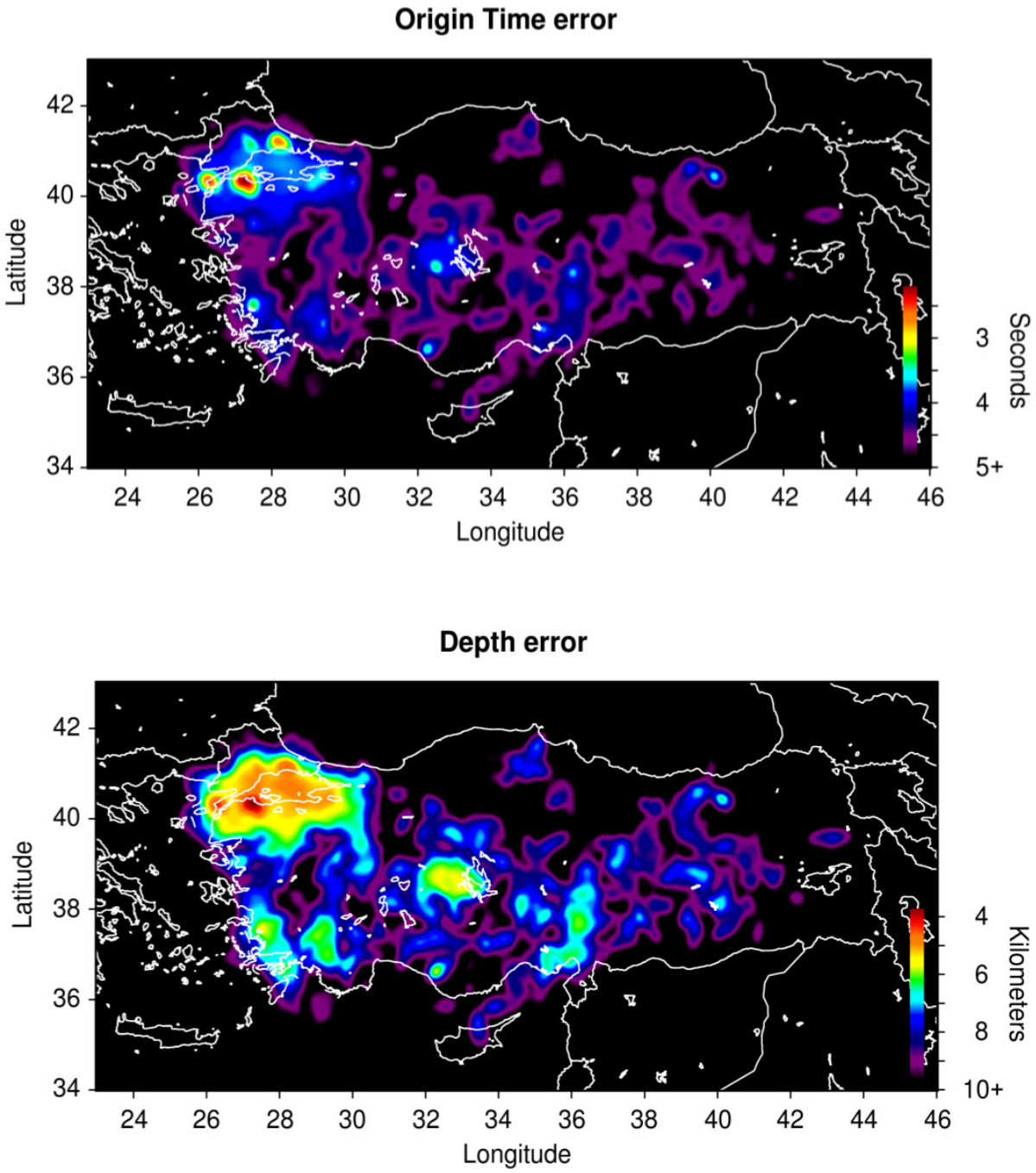

Figure 6.6. SNES maps of origin time error and depth error for M_L 3.0, H = 10 km and confidence level of 95 per cent. The origin time error reaches to about 2 seconds. The errors in hypocentral estimate drop to 4 km

M_L 3.5

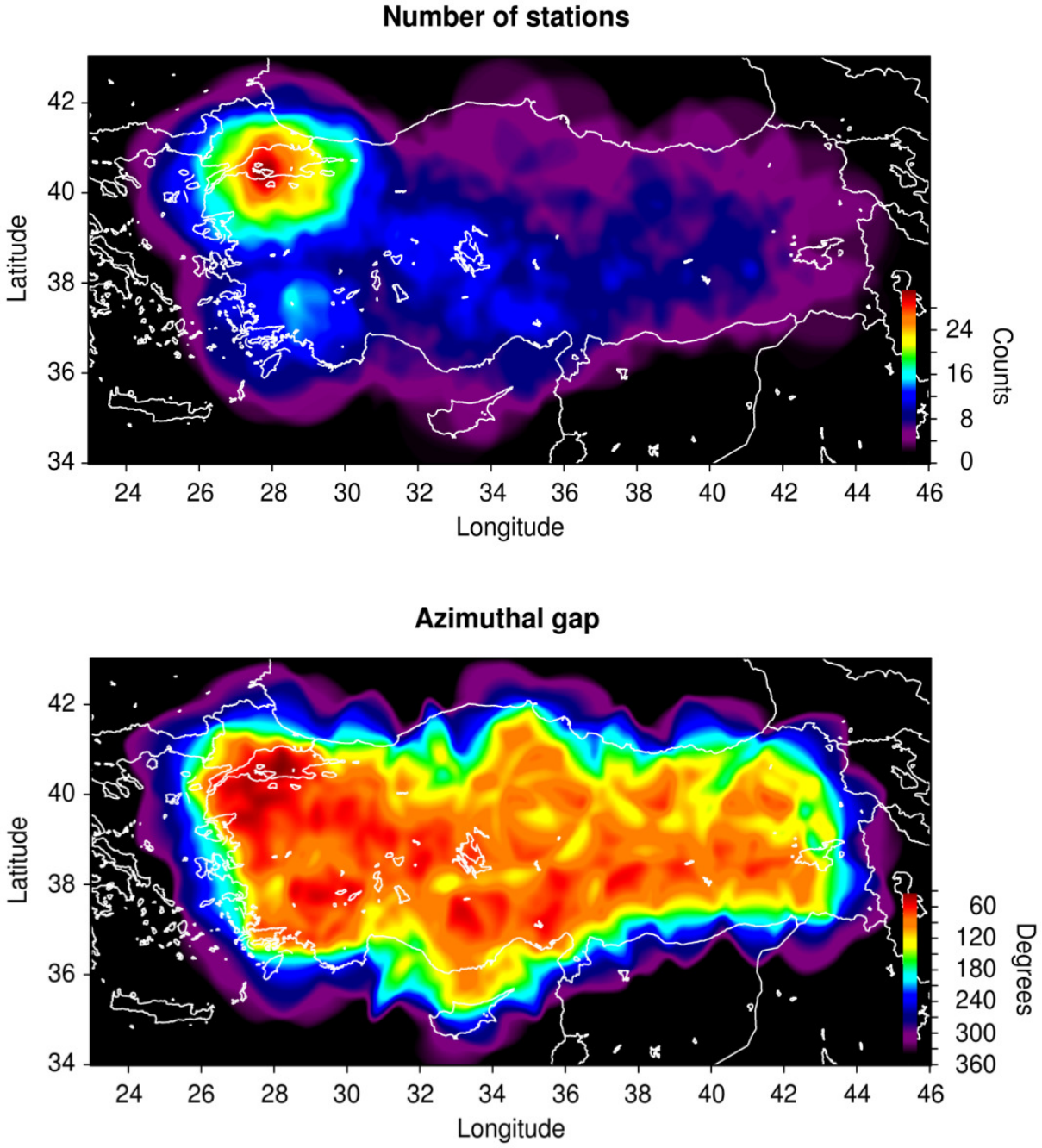

6.7. SNES maps of number of stations and azimuthal gap for M_L 3.5, H = 10 km and confidence level of 95 per cent. The maximum number of stations exceeds 28, while the minimum azimuthal gap drops to about 40°

M_L 3.5

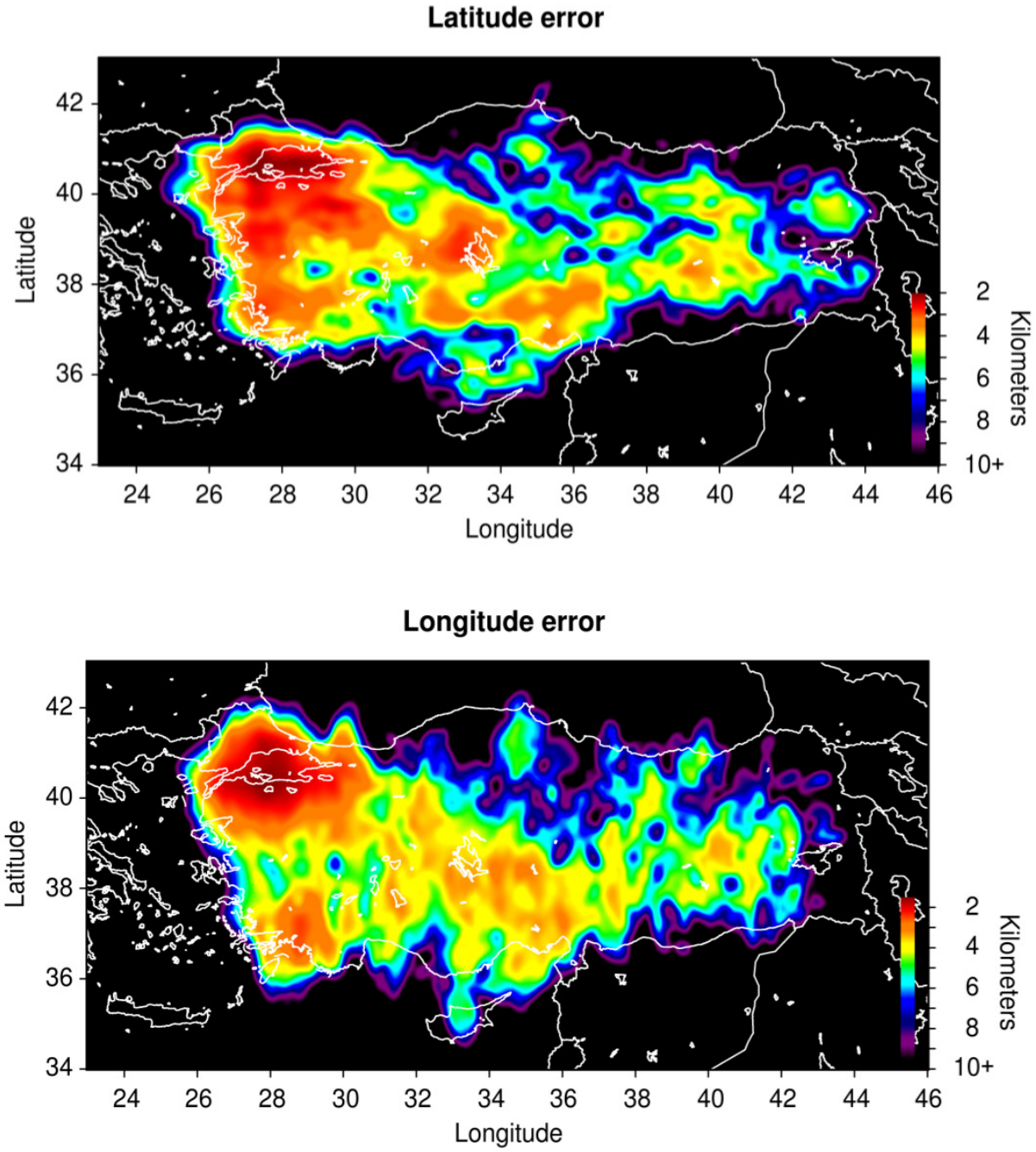

Figure 6.8. SNES maps of latitude and longitude error for M_L 3.5, H = 10 km and confidence level of 95 per cent. The minimum error in epicentral estimate is about 2 seconds, seen in Marmara Region

M_L 3.5

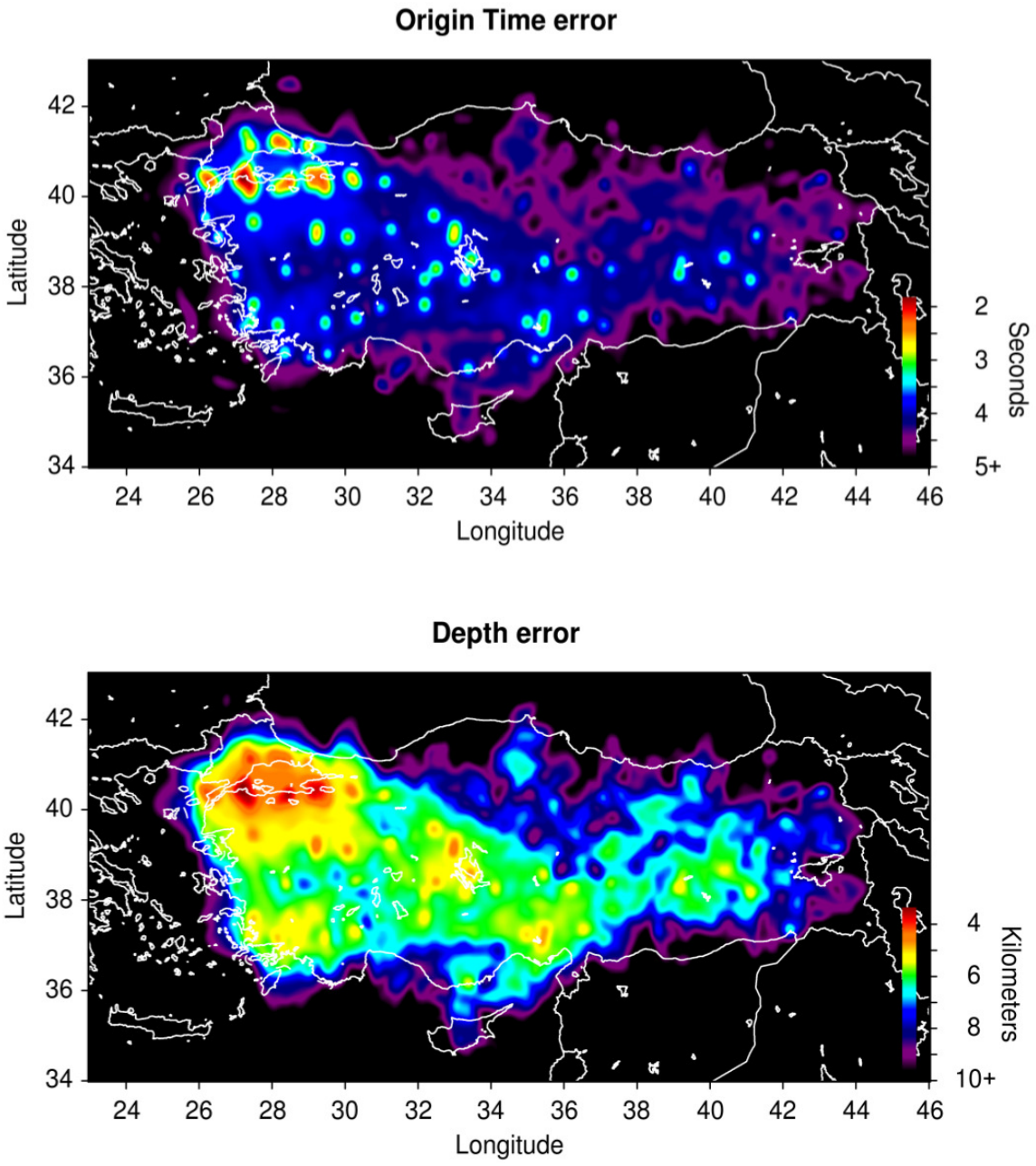

Figure 6.9. SNES maps of origin time error and depth error for M_L 3.5, H = 10 km and confidence level of 95 per cent. The origin time error falls below 2 seconds. The minimum error in hypocentral estimate is about 3 km and seen at some parts of Marmara Sea

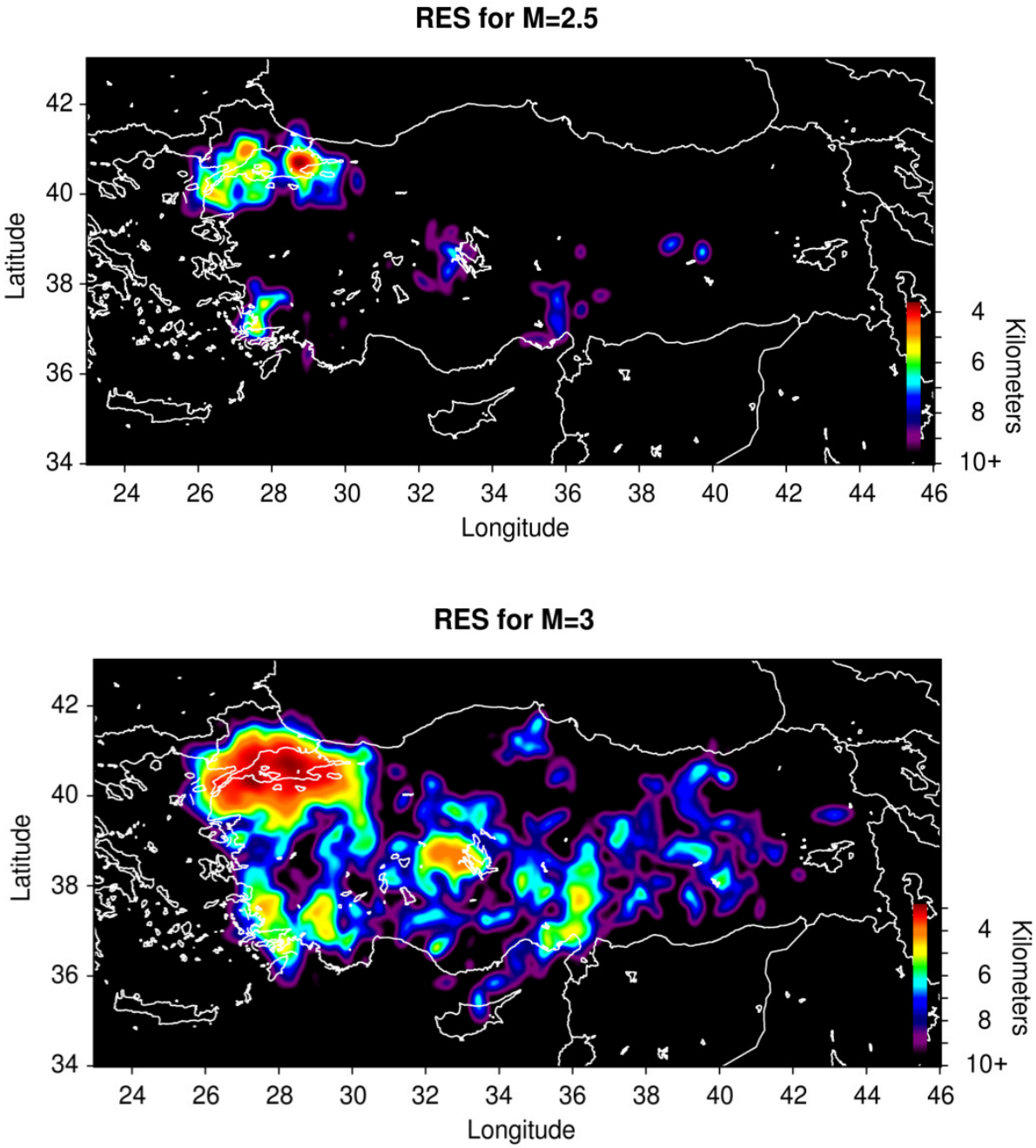

Figure 6.10. Map of hypocentral position uncertainties for M = 2.5 and M = 3.0 which were calculated as RES of the 95 per cent confidence ellipsoid

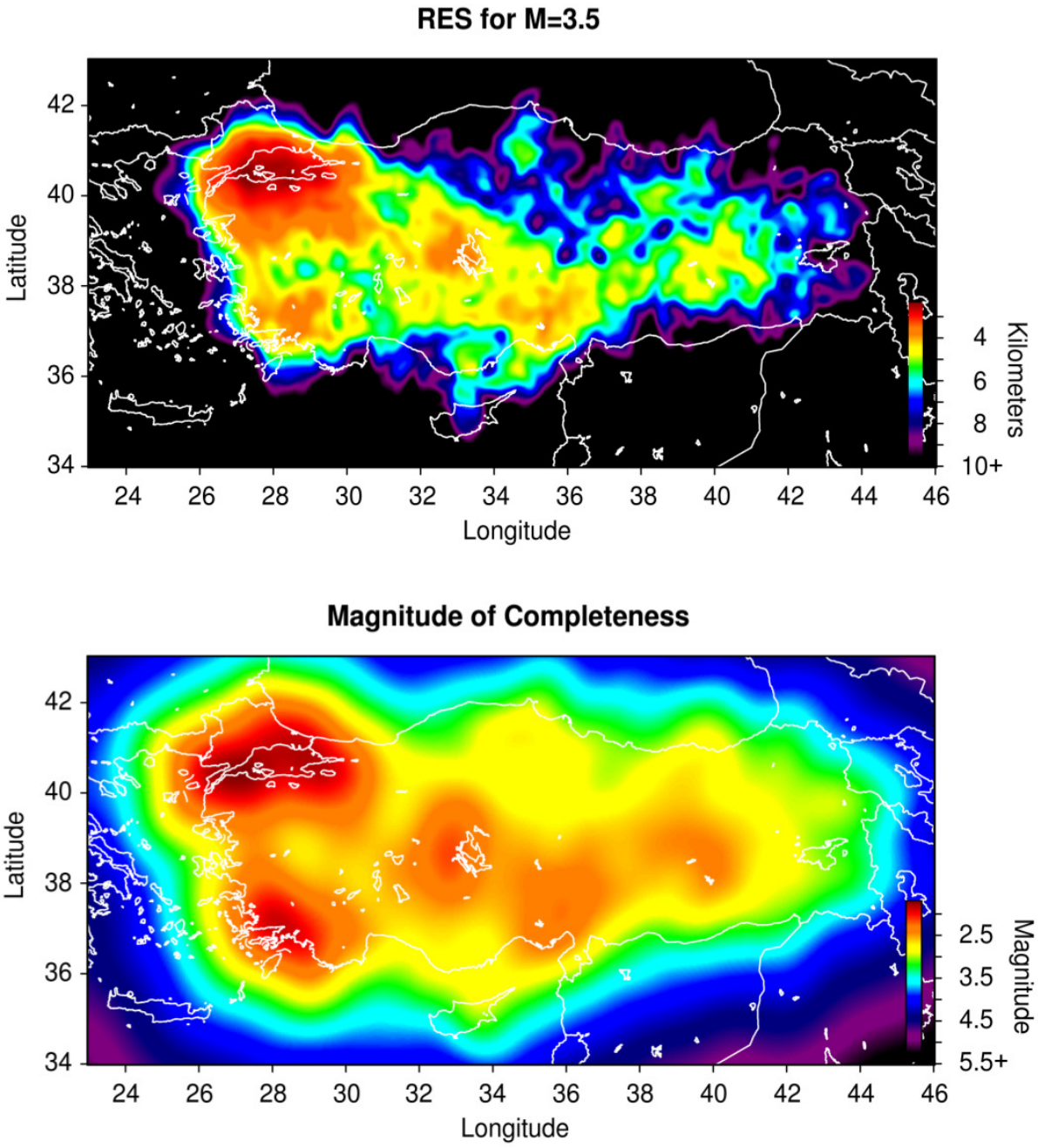

Figure 6.11. Above: Map of hypocentral position uncertainties for M = 3.5 were calculated as RES of the 95 per cent confidence ellipsoid. Below: M_c map which was determined by the SNES method

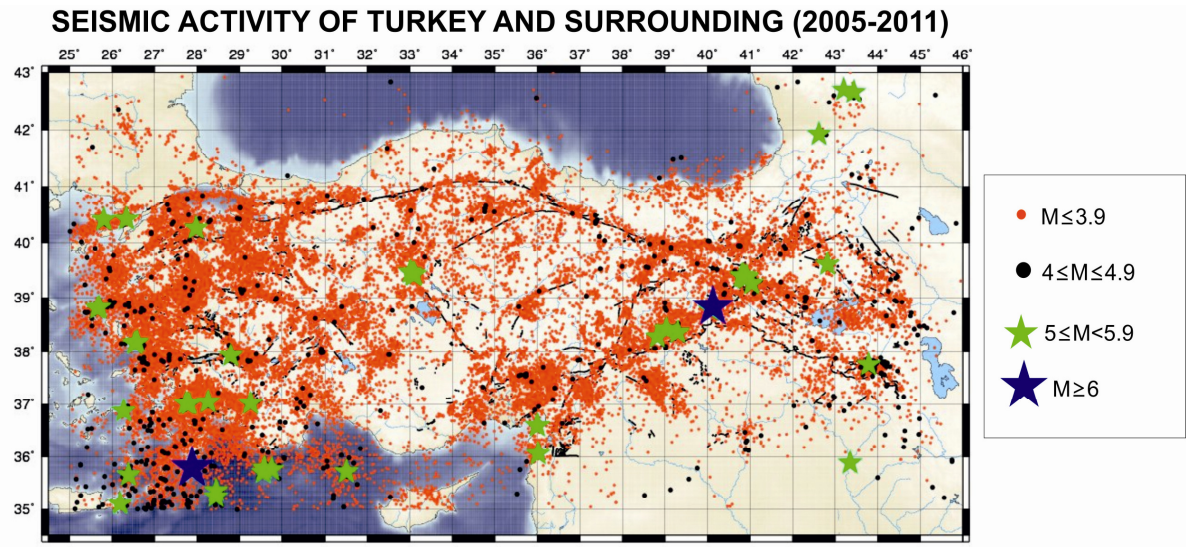

Figure 6.12. Seismic activity of Turkey and surrounding regions (NEMC, 2011)

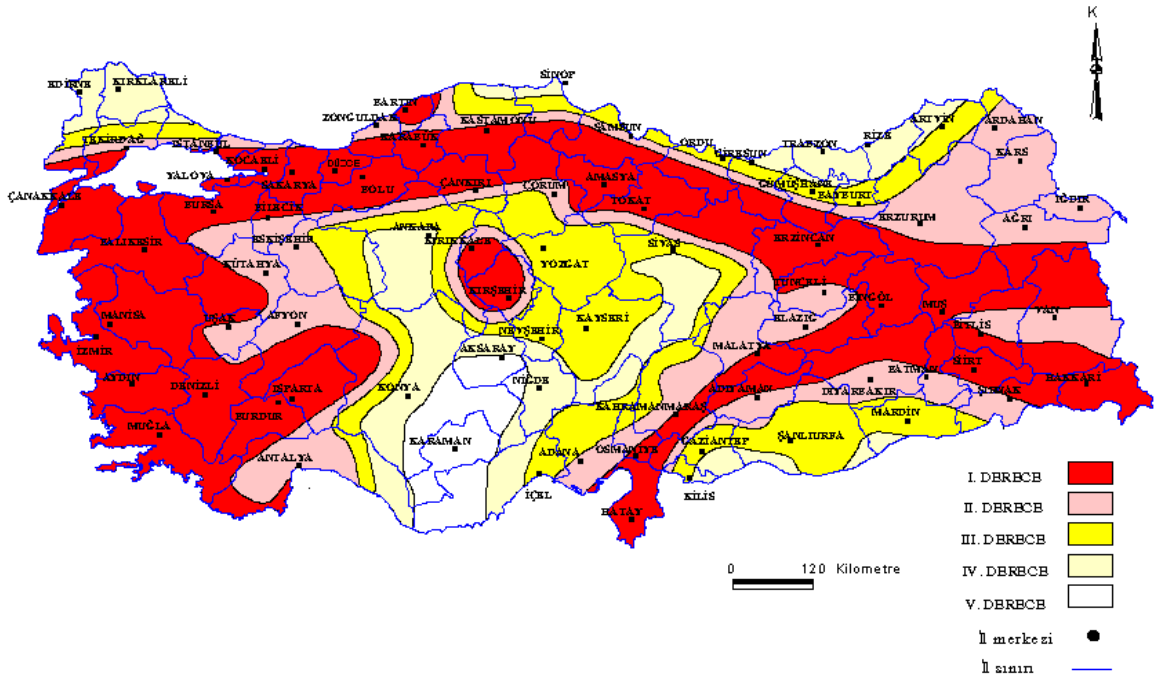

Figure 6.13. Earthquake hazard map of Turkey (Ministry of Public Works and Settlement, 1996)

The map of seismic activity of Turkey and surrounding region is given in Figure 6.12 (NEMC, 2011).

The earthquake hazard map given in Figure 6.13, was constructed according to the peak ground acceleration (PGA) values with 10 per cent probability of exceedance in 50 years and divides Turkey into 5 areas where the PGA values are expected to be greater than 0.4 g or smaller than 0.1 g in red and white regions, respectively. In other words the red colored regions have the most vulnerable places when a strong earthquake occurs (Özmen *et al.,* 1997).

In Figure 6.10, the southeast part of Marmara Sea is well covered for M_L 2.5 and shows RES of about 4 km. For M 3.0 and M 3.5, Marmara Region and surrounding areas demonstrates the best RES values of about 3 km and 2.5 km, respectively.

In Figure 6.12, epicentral locations of earthquakes with magnitudes less than or equal to 3.9 are illustrated with orange dots, which is compatible with Figure 6.13 defining the areas by high seismic hazard. Although these areas contain active faults, they are not well covered for M 3.5, 3.0 and 2.5 on the RES maps showing variable RES values between 2.5 km and 10+ km, except some parts of Marmara Region.

Most of the Turkish territory is not covered for M_L 2.5 events, probably due to the low density of the seismic stations. It is the same for M_L 3.0 but better than the coverage for M_L 2.5 events. East and west parts of Black Sea region are not covered for M_L 3.5 events, probably again due to the low density of stations and may be due to the high noise of the area caused by the sea waves.

The M_c map was constructed by fixing the hypocentral depth at 10 km and the probability level at 0.95. Comparing the SNES maps with the M_c map, it is clearly seen that the parameter M_c overestimates the level of coverage of the seismic stations of BU-KOERI, particularly in the areas outside the network. For instance, at M_L 2.5, the SNES map shows that the hypocentral depth is poorly constrained in many parts of Turkish territory, whereas the M_c map shows good network coverage where the error in hypocentral depth is the highest in the SNES map. Also, Marmara Region and southwest part of Turkey are well covered in the M_c map for M_L 2.5. Moreover, in the M_c map for M_L 2.5, surrounding regions of Tuz Lake, Adana and Elazığ are well covered; however those regions are covered with the error in hypocentral depth at least 8 km in the SNES

map. At M_L 3.0 in the M_c map, the majority of Turkey and northern Cyprus are well covered while only the southwest part of Marmara Sea indicates acceptable errors. At M_L 3.5 in the M_c map, the areas that bordering the Turkish peninsula are well covered while they are not covered or covered with high errors of hypocentral depth in the SNES map.

Lastly, in Figure 6.15, a vertical section of the location uncertainty between the points A (Lat 35,Lon 28) and B (Lat 43, Lon 28) is illustrated for M_L 3.5 and a confidence level of 95 per cent. The northern part of the vertical section shows that the error in latitude, longitude, depth and RES increase with depth, whereas in the southern part of it, the errors vary along the section. The northern part of the section shows that the epicenter is well constrained to a hypocentral depth of about 50 km with 2 km error while the southern part of the section shows 3 km error for the same hypocentral depth. Both the latitude and longitude errors in the northern part of the section indicate minimum values of errors at depth zero. In southern part of the section, the hypocentral depth is well constrained to a depth of 50 km with 5.5 km error whereas in the northern part of it, the error is about 4 km at the same depth. The minimum error in hypocentral depth (3.5 km) is seen at a depth about 10 km in the northern part of the section whereas the minimum error in hypocentral depth is 6 km at the same depth in the southern part of it. The coverage in the northern part of the section is better, which shows a RES that for M_L 3.5 has an error of less than 3 km at zero.

Figure 6.14. Vertical section of points A (35 Lat., 28 Lon.) and B (43 Lat., 28 Lon.)

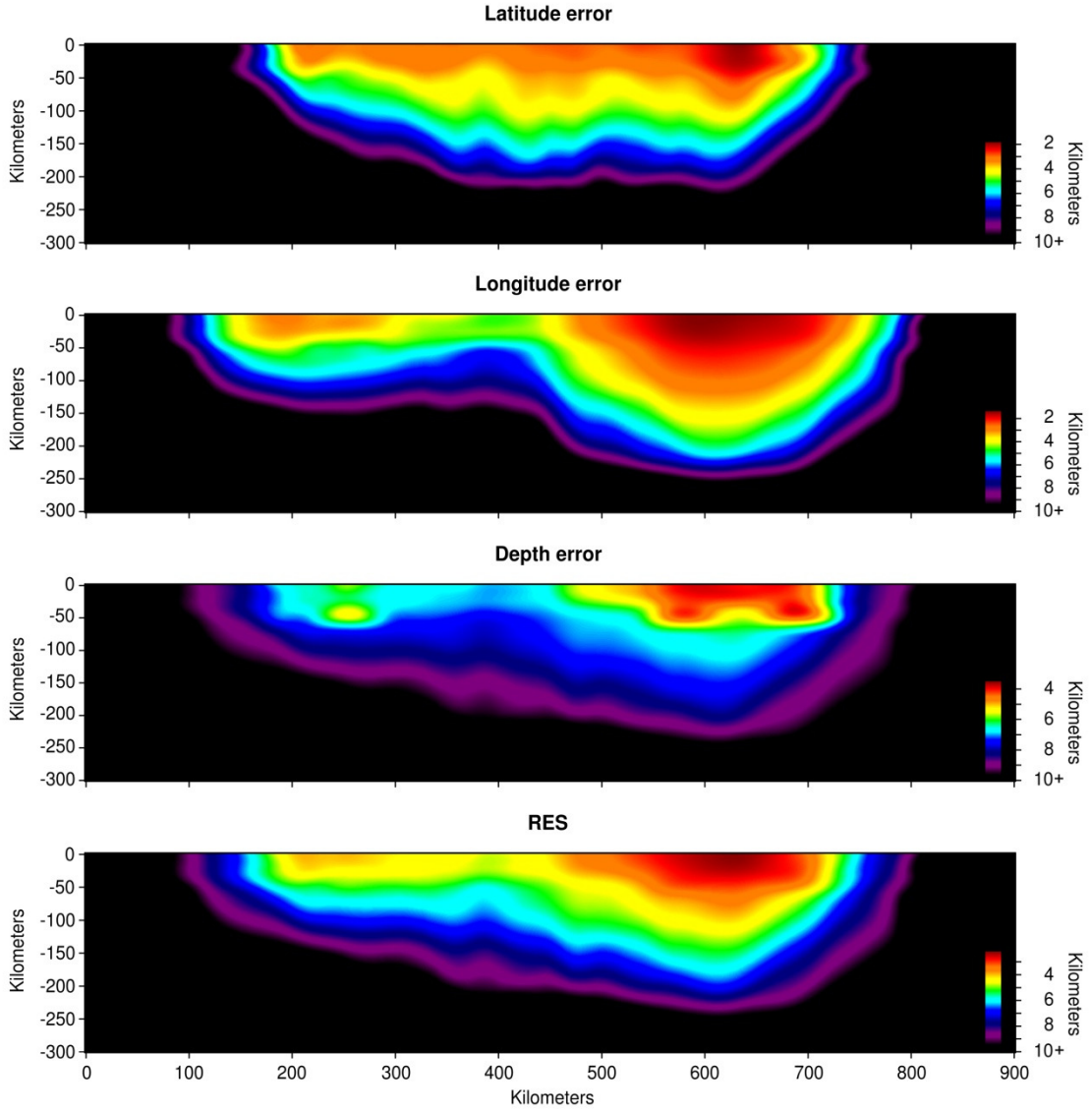

Figure 6.15. Vertical section of the location uncertainty between points A and B determined for M_L 3.5 and a confidence level of 95 per cent

7. CONCLUSION

In order to evaluate location performance with the current form of the stations, the SNES method was applied to the BU-KOERI seismic stations. The method has an advantage of estimating the location errors in areas of high and low seismicity. It is also convenient for planning the installation of new seismic stations.

The average noise power map of Turkey was constructed in the frequency range 1-12 Hz, which illustrates the areas of higher background noise (Istanbul and neighboring regions and Cyprus Island) and of lower background noise (Kayseri, Nevşehir, Sivas, Yozgat and Malatya) within the BU-KOERI seismic network.

An empirical law was determined which binds the variance of the residual times of the P and S phases to the hypocentral distance. The study of the residual times of P and S phases has allowed evaluating the appropriateness of the BU-KOERI velocity model used in the location procedure. In order to reduce the mean and the variance of the residual times, P and S velocity models should be optimized. To achieve this goal, optimized velocity models for different regions of the Turkish territory should be constructed.

It is shown that BU-KOERI seismic network provides the best monitoring coverage in the southeast of Marmara Sea and Gulf of Gökova with maximum number of twelve stations, for M_L 2.5, with errors that are 3 km and 5.5 km for epicenter and hypocentral depth, respectively. At M_L 3.0, BU-KOERI seismic network gives the best quality of the epicentral estimate with a maximum number of twenty stations in Marmara Region with errors that are 2 and 4 km for epicenter and hypocentral depth, respectively. At M_L 3.0, the seismic network is capable of constraining earthquake hypocenters to depths of about 220 km for offshore areas of southwest part of Turkish territory and about 150 km for northern Marmara Region with at least 28 seismic stations. This seismic network also provides a threshold of completeness down to M_L 3.0 for almost all Turkish territory.

Figure 6.10 and Figure 6.11 show that most of the Turkish territory is not covered for M_L 2.5 events, probably due to the low density of the seismic stations. It is the same for M_L 3.0 but better than the coverage for M_L 2.5 events. East and west parts of Black Sea region are not covered for M_L 3.5 events, probably again due to the low density of stations and may be due to the high noise of the area caused by the sea waves.

Comparing Figure 6.10 and 6.11 with Figure 6.12 and 6.13, areas with high seismic hazard contain active faults, they are not well covered for M 3.5, 3.0 and 2.5 on the RES maps showing variable RES values between 2.5 km and 10+ km.

It is also pointed out that the M_c is not a good measure of the performance of a seismic network. The main purpose of a seismic network is to supply earthquake location with acceptable errors. The M_c does not give any information about the expected error in hypocenter location. This parameter only indicates that whether or not a seismic network is able to detect a seismic event; it does not have a relation with the stations regarding to the hypocenter or the errors introduced by the velocity model used in the location procedure. Because of the fact that, the M_c tends to overestimate the performance of a seismic network.

The evaluation of the location performance of the BU-KOERI can be improved with the current installation of five OBSs (ocean bottom seismometer) in Marmara Sea. This deployment is expected to enhance offshore network coverage in the area between them and the stations on land.

Consequently, location performance of BU-KOERI seismic network should be improved by installing more seismic stations on the Turkish territory where the coverage of the stations is insufficient. In addition, with the construction of OBSs, the location performance of the network is expected to be enhanced.

APPENDIX A: LIST OF BU-KOERI SEISMIC STATIONS

Table A.1. List of BU-KOERI seismic stations

Code	Name	N	E	H (m)	Seismometer	Digitizer	Commun.	Location	Set-up Date	Period	Freq.	Geology
ADVT	Abdulvahap	4025,99	2944,3	193	CMG-3TD	DM24-3M	Satellite	Bursa/İznik	19.05.2006	120 s	50 Hz	Graywacke
AFSR	Afşar	3926,81	3304,22	1055	CMG-3ESPD	DM24-3M	Satellite	Ankara/Bala	15.09.2008	30 s	50 Hz	-
AGRB	Ağrı/Hamur	3934,53	4259,52	1820	CMG-3TD	DM24-3M	Satellite	Ağrı/Hamur	12.11.2006	120 s	50 Hz	Volcanic
ALT0	Altıntaş	3905,52	3011,03	1060	CMG-3TD	DM24-3M	Satellite	Kütahya/Altıntaş	31.03.2007	120 s	50 Hz	Limestone
ANTB	Antalya	3653,99	3039,23	20	CMG-6TD	DM24-3M	İnternet	Antalya	12.03.2004	30 s	50 Hz	Alluvium
ARMT	Armutlu	4034,1	2851,96	320	CMG-3ESPD	DM24-3M	Satellite	Yalova/Armutlu	17.12.2007	30 s	50 Hz	Graywacke
AYDB	Aydın	3756,8	2753,45	1246	CMG-3ESPCD	DM24-3M	Satellite	Aydın/Paşa yaylası	03.10.2009	30 s	50 Hz	Limestone
BALB	Balıkesir	3938,4	2752,8	120	CMG-3TD	DM24-3M	Satellite	Balıkesir	27.06.2002	120 s	50 Hz	Volcanic(Basalt-Andesite)
BAYT	Bayburt	4039,35	4014,1	1675	CMG-3ESPCD	DM24-3M	Satellite	Bayburt/Aydıntepe	17.09.2008	30 s	50 Hz	-

BCA0	Borçka	4126,7	4137,34	500	CMG-3TD	DM24-3M	Satellite	Artvin/Borçka	24.05.2006	120 s	50 Hz	Limestone
BCK0	Bucak	3727,66	3035,26	859	CMG-3TD	DM24-3M	Satellite	Burdur/Bucak	29.03.2001	120 s	50 Hz	Limestone
BGKT	Boğazköy	4110,86	2846,38	80	CMG-3ESPD	DM24-3M	Satellite	İstanbul/Boğazköy	07.08.2007	30 s	50 Hz	Metamorphic
BLCB	Balçova	3823,12	2702,52	150	CMG-3TD	DM24-3M	İnternet	İzmir/Balçova	05.10.2004	360 s	50 Hz	Limestone
BNGB	Bingöl	3859,48	4040,75	1180	CMG-3ESPCD	DM24-3M	Satellite	Bingöl/Ilıcalar	21.11.2008	30 s	50 Hz	Limestone
BNN0	Bünyan	3851,13	3550,83	1380	CMG-3TD	DM24-3M	Satellite	Kayseri/Bünyan	23.01.2007	120 s	50 Hz	Limestone
BODT	Bodrum	3703,73	2718,62	379	CMG-3ESPD	DM24-3M	Satellite	Muğla/Bodrum	14.02.2005	30 s	50 Hz	Limestone
BUY0	-	-	-	-	-	-	-	-	-	-	-	-
CANT	Çankırı	4036,37	3337,18	815	CMG-3TD	DM24-3M	Satellite	Çankırı	12.12.2006	120 s	50 Hz	Limestone
CAVI	Çavuşköy	4012,11	2950,26	670	CMG-3ESPD	DM24-3M	Satellite	Bilecik/Çavuşköy	27.09.2007	30 s	50 Hz	Limestone
CEYT	Ceyhan	3700,64	3544,87	100	CMG-3ESPD	DM24-3M	Satellite	Adana/Ceyhan	24.08.2005	30 s	50 Hz	Limestone

CHBY	Cihanbeyli	3834,94	3253,41	1086	CMG-6TD	DM24-3M	GPRS	Konya/Cihanbeyli	-	30 s		-
CLDR	Çaldıran	3908,64	4355,03	2094	CMG-3ESPD	DM24-3M	Satellite	Van/Çaldıran	16.12.2004	30 s	50 Hz	Basalt
CORM	Çorum	4010,71	3437,81	1292	CMG-3ESPD	DM24-3M	Satellite	Çorum	08.10.2004	30 s	50 Hz	Limestone
CRLT	Çorlu-Tekirdağ	4107,74	2744,16	230	CMG-3ESPD	DM24-3M	Satellite	Tekirdağ/Çorlu	16.05.2007	30 s	50 Hz	Limestone
CTKS	Kestanelik-Çatalca	4114,24	2830,43	47	CMG-3ESPD	DM24-3M	Satellite	İstanbul/Çatalca	28.09.2007	30 s	50 Hz	Limestone
CTYL	Yalıköy-Çatalca	4128,56	2817,38	77	CMG-3TD	DM24-3M	Satellite	İstanbul/Çatalca	29.09.2007	360 s	50 Hz	Limestone
CUKT	Çukurca	3714,84	4336,46	1298	CMG-3ESPD	DM24-3M	Satellite	Hakkari/Çukurca	01.10.2005	30 s	50 Hz	Limestone(hard)
DALT	Dalyan	3646,15	2838,23	548	CMG-3TD	DM24-3M	Satellite	Muğla/Dalyan	17.08.2004	120 s	50 Hz	Limestone
DARE	Darende	3834,27	3728,99	1080	CMG-6TD	DM24-3M	Satellite	Malatya/Darende	31.07.2007	30 s	50 Hz	Limestone
DAT0	Datça	3643,74	2734,67	1100	CMG-3ESPD	DM24-3M	Satellite	Muğla/Datça	08.10.2005	30 s	50 Hz	Limestone(hard-bedrock)
DIKM	Dikmen	4138,98	3515,47	258	CMG-3TD	DM24-3M	Satellite	Sinop/Dikmen	27.06.2006	120 s	50 Hz	Marl-Limestone

DKL	Dikili	3904,28	2654,32	49	CMG-3TD	DM24-3M	Satellite	İzmir/Dikili	-	120 s		-
DYBB	Diyarbakır	3757,19	4008,36	657	CMG-3TD	DM24-3M	Satellite	Diyarbakır	10.12.2009	120 s	50 Hz	-
EDC0	Edincik	4020,81	2751,8	269	CMG-3TD	DM24-3M	Satellite	Balıkesir/Edincik	12.07.2008	120 s	50 Hz	Granite
EDRB	Edirne	4150,82	2644,62	209	CMG-40TD	DM24-3M	Satellite	Edirne/Lalapaşa	27.03.2002	360 s	50 Hz	Gneiss-Schist
ELL0	Elmalı	3644,9	2954,51	1230	CMG-3TD	DM24-3M	Satellite	Antalya/Elmalı	22.09.2006	120 s	50 Hz	Limestone
ENEZ	Enez	4044,17	2609,18	100	CMG-3TD	DM24-3M	Satellite	Edirne/Enez	21.02.2006	120 s	50 Hz	Limestone
EREN	Yenierenköy	3531,75	3410,45	88	CMG-3TD	DM24-3M	Satellite	KKTC/Yenierenköy	22.03.2007	120 s	50 Hz	Limestone
ERIK	Erikli	4040,25	2630,79	41	CMG-3ESPD	DM24-3M	Satellite	Edirne/Keşan	02.07.2008	30 s	50 Hz	Limestone
ERZN	Erzincan	3935,2	3943,32	1500	CMG-3ESPD	DM24-3M	Satellite	Erzincan/Çağlayan	13.10.2008	30 s	50 Hz	Limestone
ESPY	Espiye	4091,	3872	430	CMG-ESP	DM24-	Satellite	Giresun/Es	02.03.2007	60 s	50	Hard ground

		67	,73			3M		piye			Hz	
EZN0	Ezine	3949,6	2619,55	48	CMG-3TD	DM24-3M	Satellite	Çanakkale/Ezine	11.10.2006	30 s	50 Hz	Serpentine Breccia
FETY	Fethiye	3638,12	2905,01	200	CMG-3ESPD	DM24-3M	Satellite	Muğla/Fethiye	03.12.2004	30 s	50 Hz	Limestone
GADA	Gökçeada	4011,45	2553,92	130	CMG-3TD	DM24-3M	Satellite	Çanakkale/Gökçeada	05.07.2006	120 s	50 Hz	Basalt
GAZ	Gaziantep	3710,33	3712,68	864	CMG-3TD	DM24-3M	Satellite	Gaziantep	06.03.2007	120 s	50 Hz	Limestone
GEDZ	Gediz	3902.66	2924.63	886	CMG-6T	DM24-3M	GSM-GPRS	Kütahya	-	-	-	-
GEMT	Gemlik	4026,1	2911,34	220	CMG-3TD	DM24-3M	Satellite	Bursa/Gemlik	07.07.2006	120 s	50 Hz	Limestone
GLHS	Gölhisar	3715,6	2949,83	1100	CMG-6T	-	-	Burdur/Gölhisar	08.04.2005	30 s	50 Hz	Sandy Clay
GONE	Gönen	4002,8	2741,16	140	CMG-3ESPD	DM24-3M	Satellite	Balıkesir/Gönen	27.06.2008	30 s	50 Hz	Limestone
GULA	Gülağaç	3820,66	3414,16	1128	CMG-6TD	DM24-3M	GPRS	Aksaray/Gülağaç	-	30 s	-	-
GULT	Gölveren-Taraklı	4025,92	3030,9	930	CMG-3ESPD	DM24-3M	Satellite	Sakarya/Taraklı	15.09.2007	30 s	50 Hz	Limestone

HDMB	Hadim	3657,84	3229,16	1946	CMG-3TD	DM24-3M	Satellite	Konya/Hadim	06.11.2003	30 s	50 Hz	Limestone
HRTX	Hereke	4049,3	2940,08	645	CMG-3ESPD	DM24-3M	Satellite	Kocaeli/Hereke	25.06.2008	30 s	50 Hz	Calcereous shale
IKL0	Silifke	3614,32	3341,11	120	CMG-3TD	DM24-3M	Satellite	Mersin/Silifke	24.07.2006	120 s	50 Hz	Limestone
ILIC	İliç	3927,12	3834,07	1280	CMG-ESPD	DM24-3M	Satellite	Erzincan/İliç	-	-	-	-
ISK0	Üsküdar	4103,94	2903,55	132	CMG-3TD	DM24-3M	Network	İstanbul/Üsküdar	01.01.1997	120 s	50 Hz	Graywacke,Calcerous shale
KARA	Karaisalı	3715,64	3503,28	366	CMG-3ESPD	DM24-3M	Satellite	Adana/Karaisalı	26.08.2005	30 s	50 Hz	Limestone(hard)
KARS	Kars	4036,91	4305,62	1747	CMG-3TD	DM24-3M	Satellite	Kars	13.10.2006	120 s	50 Hz	Basalt
KCTX	Karacabey	4015,93	2821,39	451	CMG-3ESPD	DM24-3M	Satellite	Bursa/Karacabey	11.07.2008	30 s	50 Hz	Sandstone
KDZE	Karadeniz Ereğli	4118,79	3126,58	410	CMG-3TD	DM24-3M	Satellite	Zonguldak/Ereğli	01.07.2006	120 s	50 Hz	Marl
KLYT	Kilyos	4115,	2902	30	CMG-3TD	DM24-	Satellite	İstanbul/Kil	18.05.2006	120	50	Clay

		18	,52			3M		yos		s	Hz	
KMRS	Kahramanmaraş	3730,32	3654	590	CMG-3TD	DM24-3M	Satellite	Kahramanmaraş	30.08.2006	120 s	50 Hz	Basalt
KONT	Tatköy (Konya)	3756,72	3221,63	550	CMG-3TD	DM24-3M	Satellite	Konya/Tatköy	20.07.2006	120 s	50 Hz	Limestone
KOZT	Kozan	3728,83	3549,61	381	CMG-3ESPD	DM24-3M	Satellite	Adana/Kozan	25.08.2005	360 s	50 Hz	Limestone(hard)
KRBG	Karabiga	4023,59	2717,86	75	CMG-3ESPD	DM24-3M	Satellite	Çanakkale/Karabiga	27.06.2008	30 s	50 Hz	Limestone
KRTS	Karataş	3634,39	3522,5	53	CMG-3ESPD	DM24-3M	Satellite	Adana/Karataş	25.08.2005	30 s	50 Hz	Metamorphosed Limestone
KTUT	Trabzon	4059,22	3946	171	CMG-3TD	DM24-3M	Satellite	Trabzon/KTÜ	17.08.2006	120 s	50 Hz	Clay
KULA	Kula	3830,87	2839,64	915	CMG-3TD	DM24-3M	Satellite	Manisa/Kula	01.03.2007	120 s	50 Hz	Basalt
KULU	Kulu	3902,56	3300,14	1121	CMG-6TD	DM24-3M	GPRS	Konya/Kulu	-	30 s	-	-
KVT0	Kavak	4104,84	3602,78	649	CMG-3TD	DM24-3M	Satellite	Samsun/Kavak	01.06.2004	120 s	50 Hz	Limestone
LADK	Ladik	3812	3221,89	1168	CMG-3TD	DM24-3M	Satellite	Konya/Ladik	19.06.2007	120 s	50 Hz	Marble

LAP0	Lapseki	4022,22	2645,56	230	CMG-3ESPD	DM24-3M	Satellite	Çanakkale/Lapseki	27.12.2007	30 s	50 Hz	Limestone
LEF0	Lefke	3506,71	3250,6	152	CMG-3TD	DM24-3M	Satellite	KKTC/Lefke	21.03.2007	120 s	50 Hz	Limestone
LFK0	Lefkoşa	3516,99	3332,02	690	CMG-3TD	DM24-3M	Satellite	KKTC/Lefkoşa	20.03.2007	120 s	50 Hz	Limestone
LOD0	Lodumlu	3953,36	3245,84	902	CMG-3TD	DM24-3M	Satellite	Ankara/Lodumlu	02.02.2007	120 s	50 Hz	Limestone
MAZI	Mazıdağı	3727,62	4026,8	1207	CMG-3TD	DM24-3M	Satellite	Mardin/Mazıdağı	29.06.2009	120 s	50 Hz	Limestone(hard)
MDUB	Mudurnu	4027,92	3112,87	1000	CMG-3TD	DM24-3M	Satellite	Bolu/Mudurnu	22.05.2008	360 s	50 Hz	Limestone(hard)
MDNY	Mudanya	4022,14	2853,04	110	CMG-3ESPD	DM24-3M	Satellite	Bursa/Mudanya	09.07.2008	30 s	50 Hz	Limestone
MERS	Mersin	3652,06	3431,33	802	CMG-3TD	DM24-3M	Satellite	Mersin	23.08.2005	120 s	50 Hz	Limestone(hard)
MLSB	Milas	3717,72	2746,59	500	CMG-40TD	DM24-3M	Satellite	Muğla/Milas	01.07.2003	30 s	50 Hz	Limestone
MRMT	Marmara Adası	4036,35	2735,02	702	CMG-3TD	DM24-3M	Satellite	Balıkesir/Marmara	09.11.2008	120 s	50 Hz	Volcanic

								Adası				
PHSR	Pınarhisar	4137,85	2731,43	263	CMG-40TD	DM24-3M	Satellite	Kırklareli/Pınarhisar	09.07.2009	30 s	-	-
PTK0	Pertek	3853,54	3923,54	1835	CMG-3TD	DM24-3M	Satellite	Tunceli/Pertek	01.09.2004	120 s	50 Hz	Marble
PZAR	Pazar	4117,8	4089,88	80	CMG-ESP	DM24-3M	Satellite	Rize/Pazar	01.03.2007	30 s	50 Hz	Basalt
RKY0	Şarköy	4041,25	2710,66	687	CMG-3ESPD	DM24-3M	Satellite	Tekirdağ/Şarköy	14.04.2006	30 s	50 Hz	Limestone
RSDY	Reşadiye	4023,83	3719,64	550	CMG-3TD	DM24-3M	Satellite	Tokat/Reşadiye	13.06.2007	120 s	50 Hz	-
SARI	Sarız	3824,43	3625,09	1673	CMG-3TD	DM24-3M	Satellite	Kayseri/Sarız	03.08.2007	100 s	50 Hz	Limestone
SERE	Şereflikoçhisar	3856,78	33.33.84	1216	CMG-6TD	DM24-3M	GPRS	Ankara/Şereflikoçhisar	-	30 s	-	-
SHUT	Şuhut	3833,18	3033,06	1215	CMG-3TD	DM24-3M	Satellite	Afyon/Şuhut	02.11.2006	120 s	50 Hz	Volcanic Anglomera
SILT	Şile	4109,18	2938,58	100	CMG-3ESPD	DM24-3M	Satellite	İstanbul/Şile	31.07.2007	30 s	50 Hz	Limestone
SIRT	Şırnak	3730,06	4226,35	1038	CMG-6TD	DM24-3M	Satellite	Şırnak/Gümüştepe	22.06.2005	120 s	50 Hz	Sandstone
SLVT	Silivri	4113,8	2812,6	180	CMG-3ESPD	DM24-3M	Satellite	İstanbul/Silivri	09.08.2007	30 s	50 Hz	Clay

SNOP	Sinop	4201,17	3512,41	180	CMG-3TD	DM24-3M	Satellite	Sinop	-	120 s	-	-
SPNC	Sapanca	4041,16	3018,5	190	CMG-3ESPD	DM24-3M	Satellite	Sakarya/Sapanca	27.06.2008	30 s	50 Hz	Weathered Limestone
SULT	Sultanhanı	3811,93	3330,94	980	CMG-3TD	DM24-3M	Satellite	Aksaray/Sultanhanı	04.01.2008	360 s	50 Hz	Limestone
SVAN	Silvan	3809,07	4111,91	650	CMG-3TD	DM24-3M	Satellite	Diyarbakır/Silvan	12.12.2009	120 s	-	-
SVRC	Sivrice	3822,65	3918,36	1680	CMG-3TD	DM24-3M	Satellite	Elazığ/Sivrice	27.04.2007	120 s	50 Hz	Graywacke
SVRH	Sivrihisar	3926,82	3131,38	1000	CMG-3TD	DM24-3M	Satellite	Eskişehir/Sivrihisar	27.12.2007	360 s	50 Hz	Granite
SVSK	Sivas	3955,05	3659,55	1630	CMG-3TD	DM24-3M	Satellite	Sivas/Karaçayır	01.08.2003	30 s	50 Hz	Volcanic(Basalt-Andesite)
SUTC	Sütçüler	3747,65	3099,97	1300	CMG-3ESP	DM24-3M	Satellite	Isparta/Sütçüler	10.11.2005	30 s	50 Hz	Limestone
TAHT	Tahtaköprü	3622,54	3611,11	266	CMG-3ESPCD	DM24-3M	Satellite	Hatay/Tahtaköprü	19.10.2009	30 s	-	Limestone
TKR0	Tekirdağ	4059,41	2732,14	140	CMG-3ESPD	DM24-3M	Satellite	Tekirdağ	18.05.2007	30 s	50 Hz	Clay
TVSB	Tavşanlı	3926,98	2927,69	1090	CMG-3ESPD	DM24-3M	Satellite	Kütahya/Tavşanlı	12.02.2009	120 s	-	Limestone
URFA	Urfa	3726,	3849	938	CMG-3ESPD	DM24-	Satellite	Urfa	02.12.2004	30 s	50	Volcanic

		46	,28			3M					Hz	
VANB	Van	3835,7	4323,33	1227	CMG-3TD	DM24-3M	Satellite	Van/Topraakkale	01.07.2003	360 s	50 Hz	Limestone
VRTB	Varto	3909,62	4127,36	1500	CMG-3ESPCD	DM24-3M	Satellite	Muş/Varto	20.11.2008	30 s	50 Hz	Limestone
YAYX	Yaylak	3856,32	3348,69	1142	CMG-6TD	DM24-3M	GPRS	Aksaray/Yaylak	-	30 s	-	-
YER0	Yerkesik	3708,17	2817,15	729	CMG-3TD	DM24-3M	Satellite	Muğla/Yerkesik	16.07.2006	120 s	50 Hz	Limestone
YESY	Yeşilyurt	3708,17	2817,15	729	CMG-6TD	DM24-3M	GPRS	Konya/Yeşilyurt	-	30 s	-	-

APPENDIX B: 2005-2010 VARIATIONS OF SEISMIC NOISE AS A FUNCTION OF PERIOD FOR VERTICAL COMPONENTS OF ALL BU-KOERI SEISMIC STATIONS

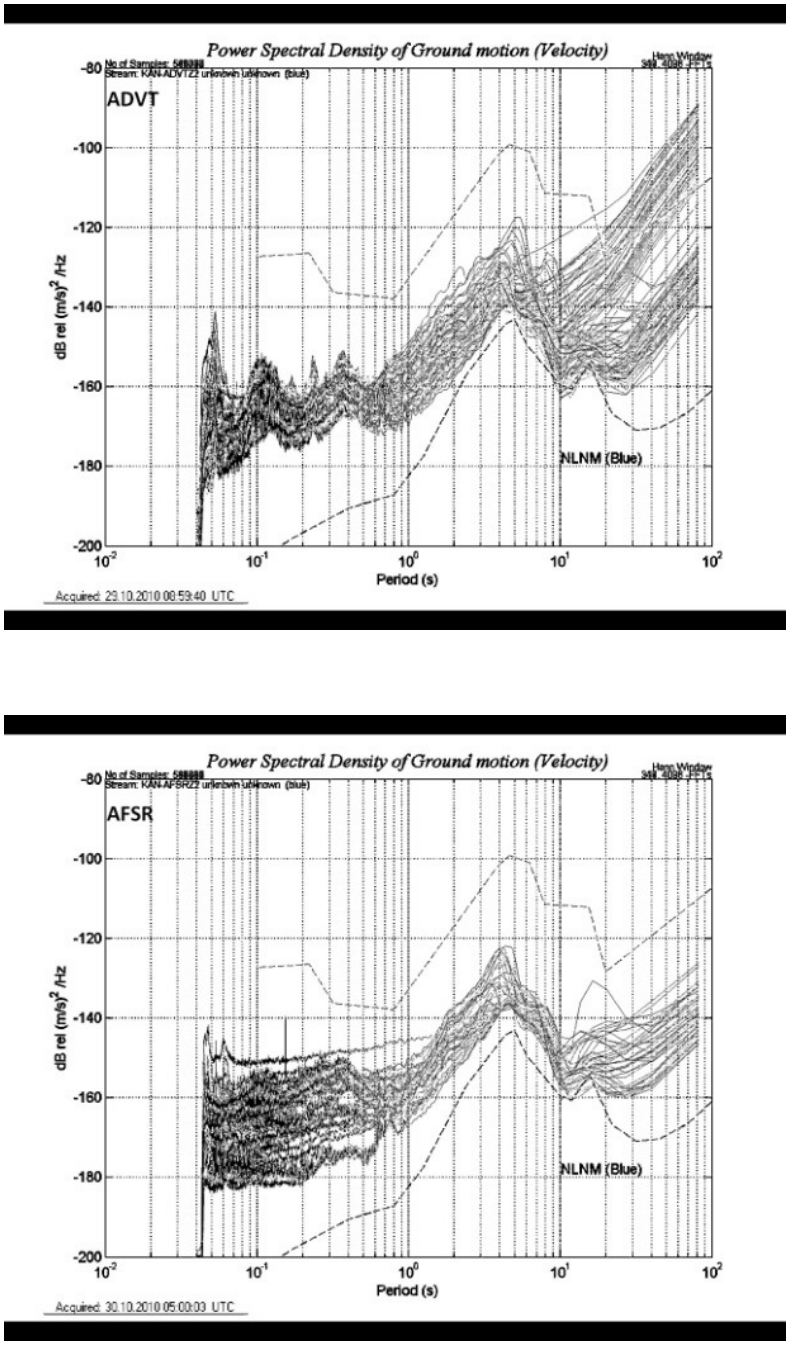

Figure B.1. PSDs of ADVT and AFSR

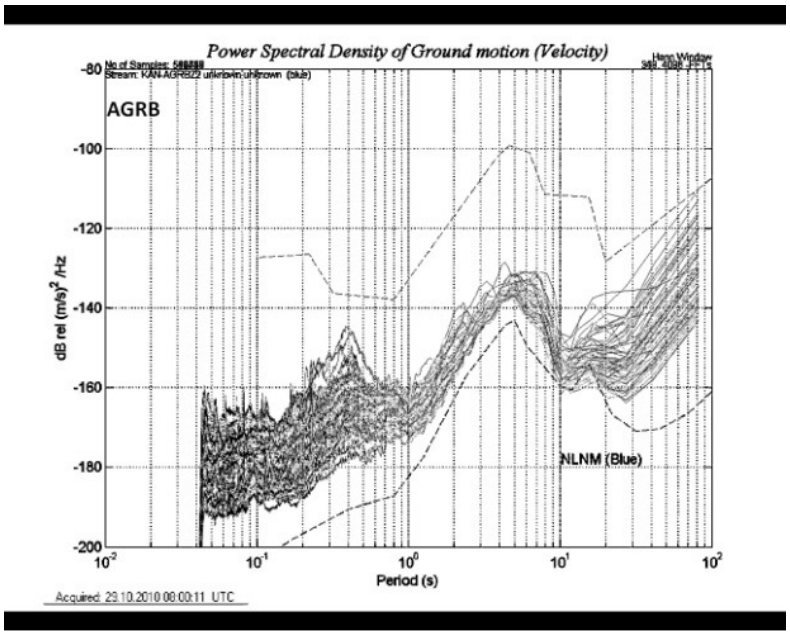

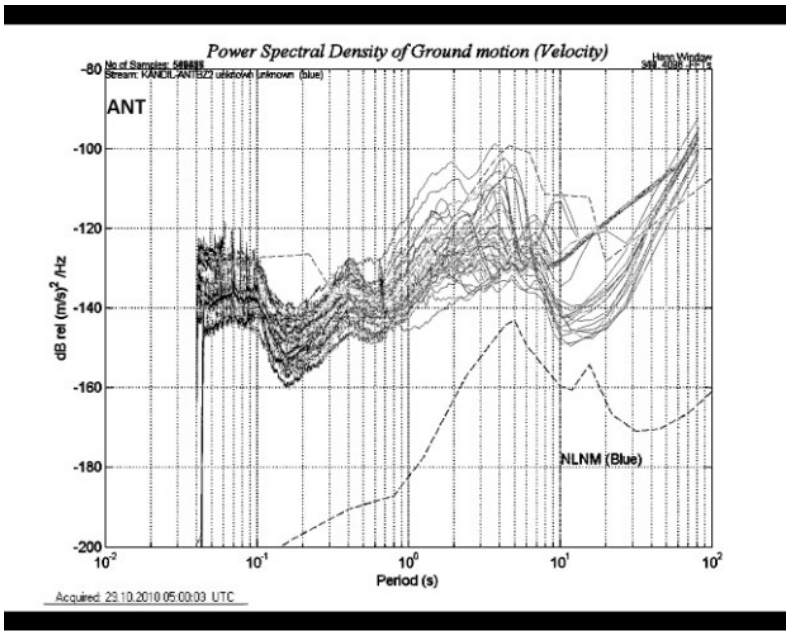

Figure B.2. PSDs of AGRB and ANT

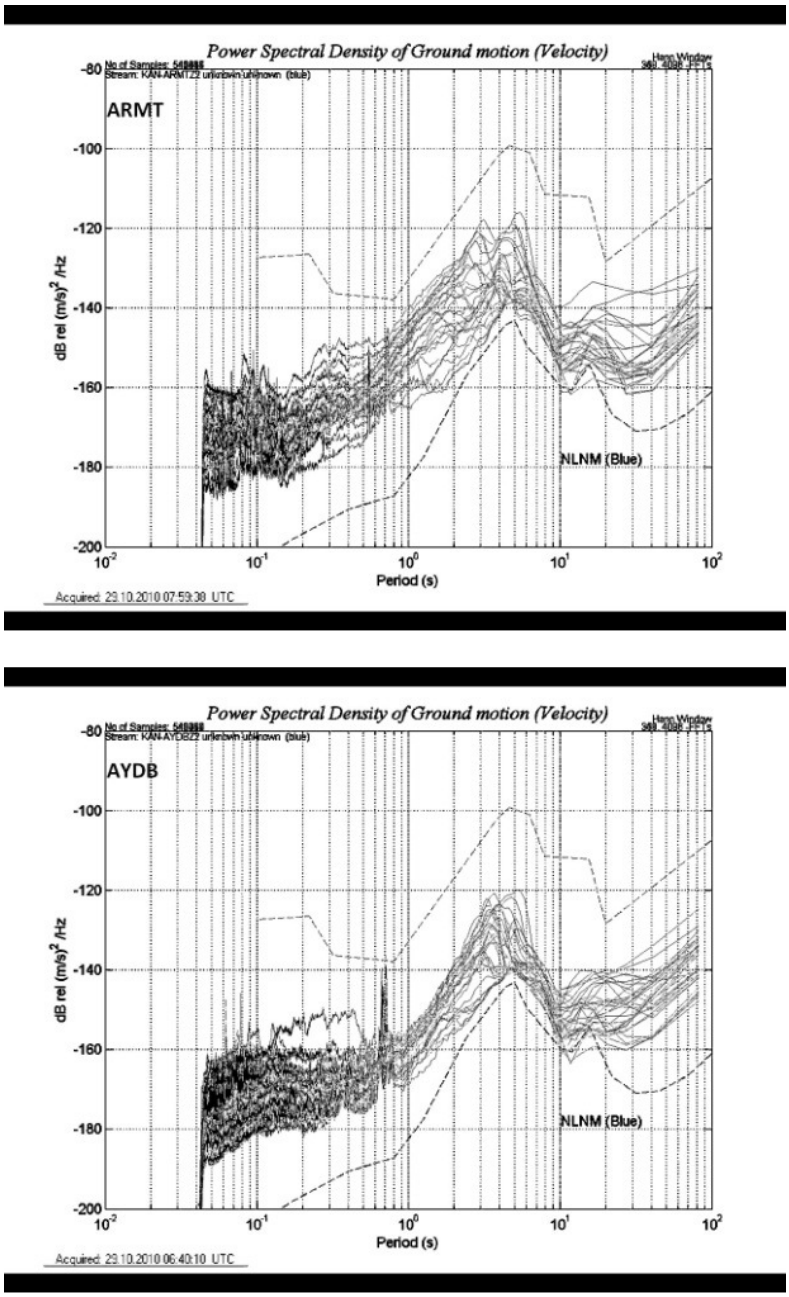

Figure B.3. PSDs of ARMT and AYDB

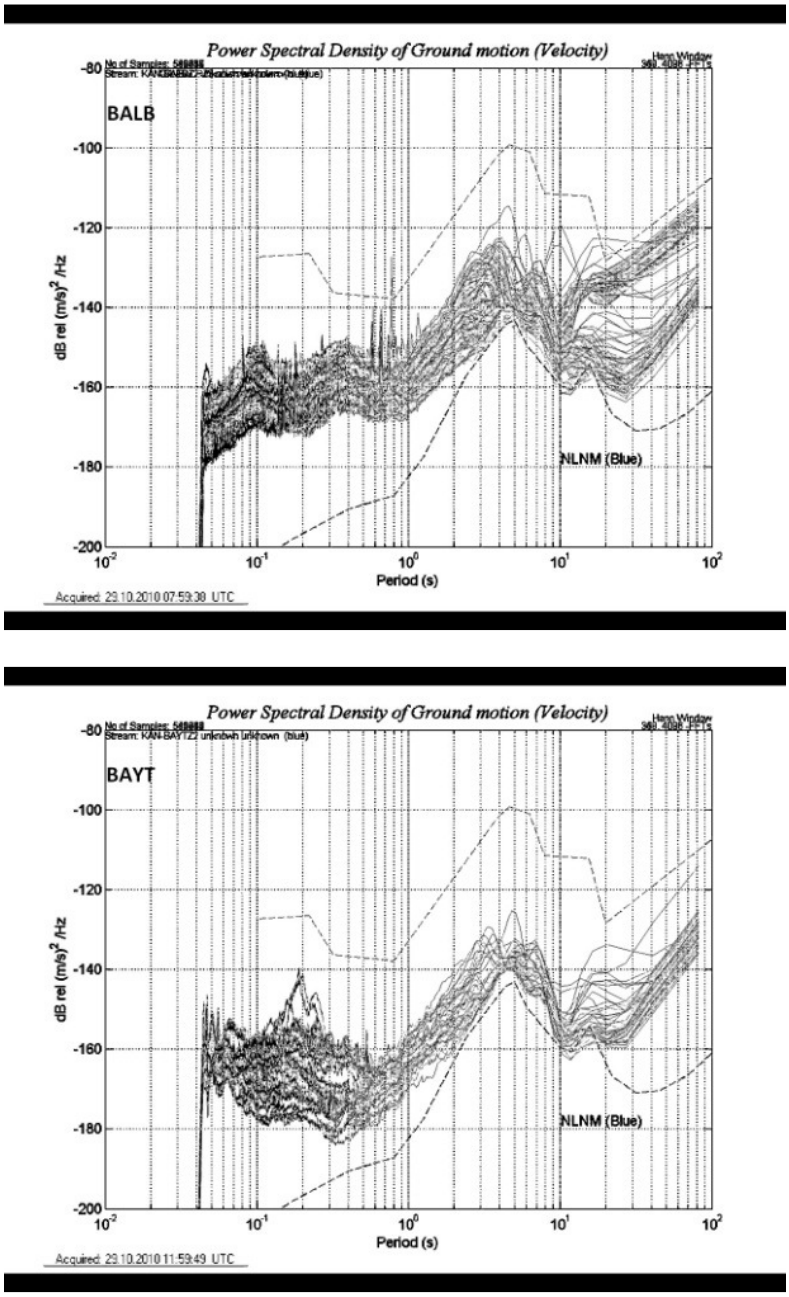

Figure B.4. PSDs of BALB and BAYT

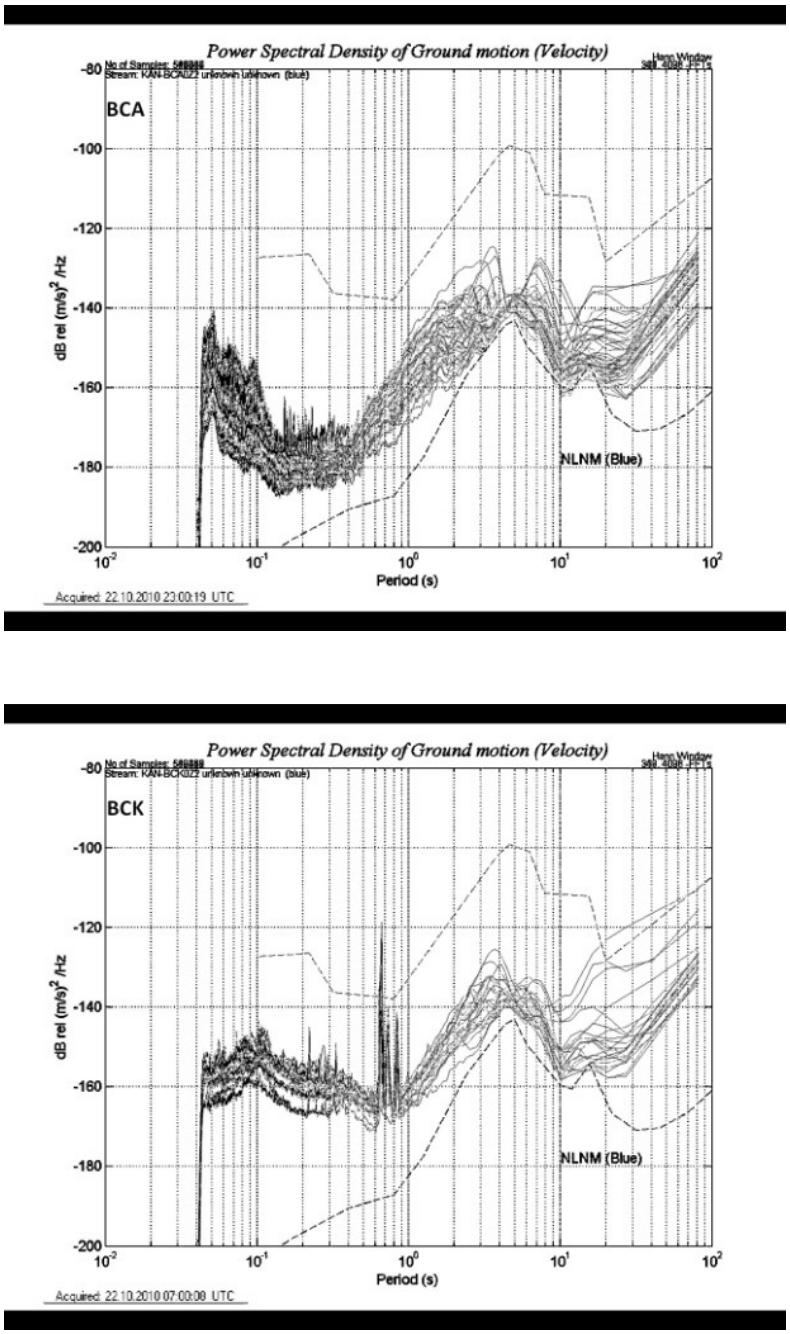

Figure B.5. PSDs of BCA and BCK

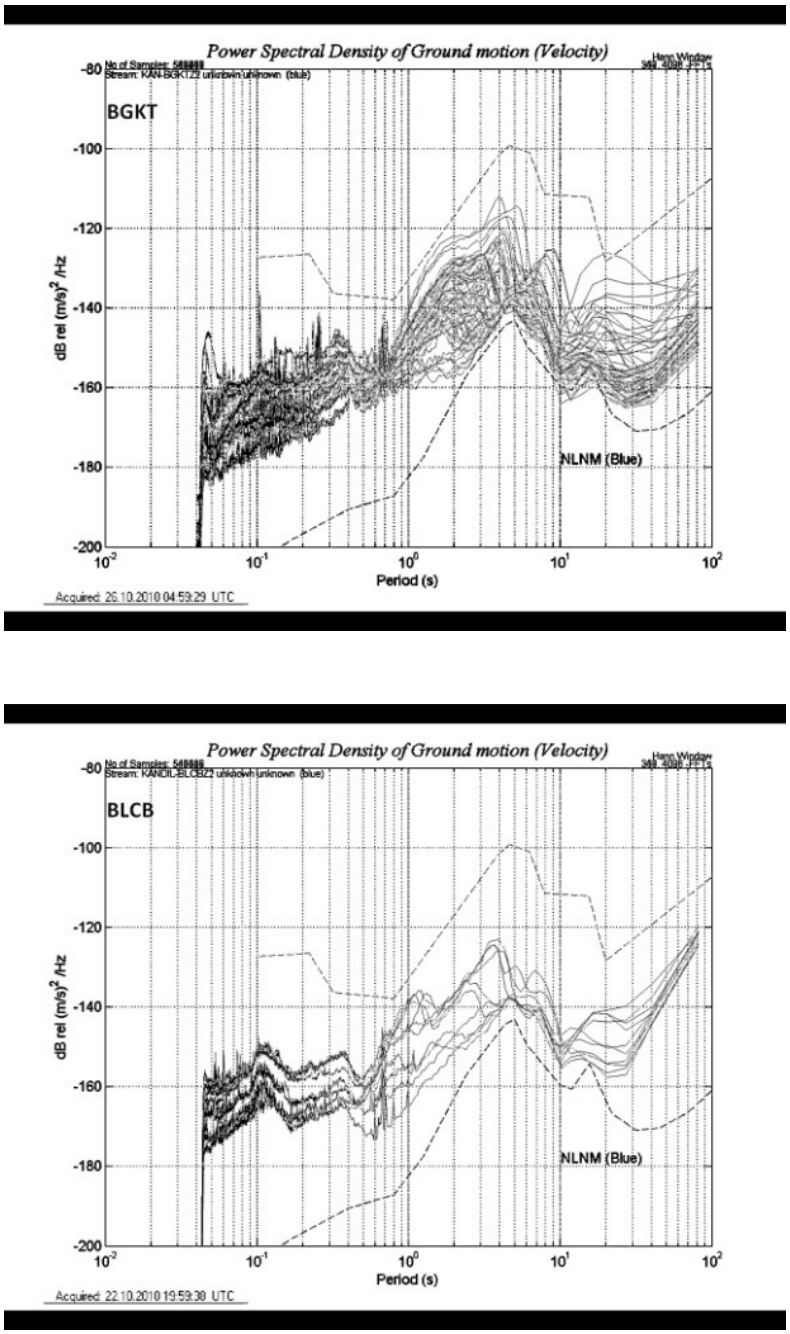

Figure B.6. PSDs of BGKT and BLCB

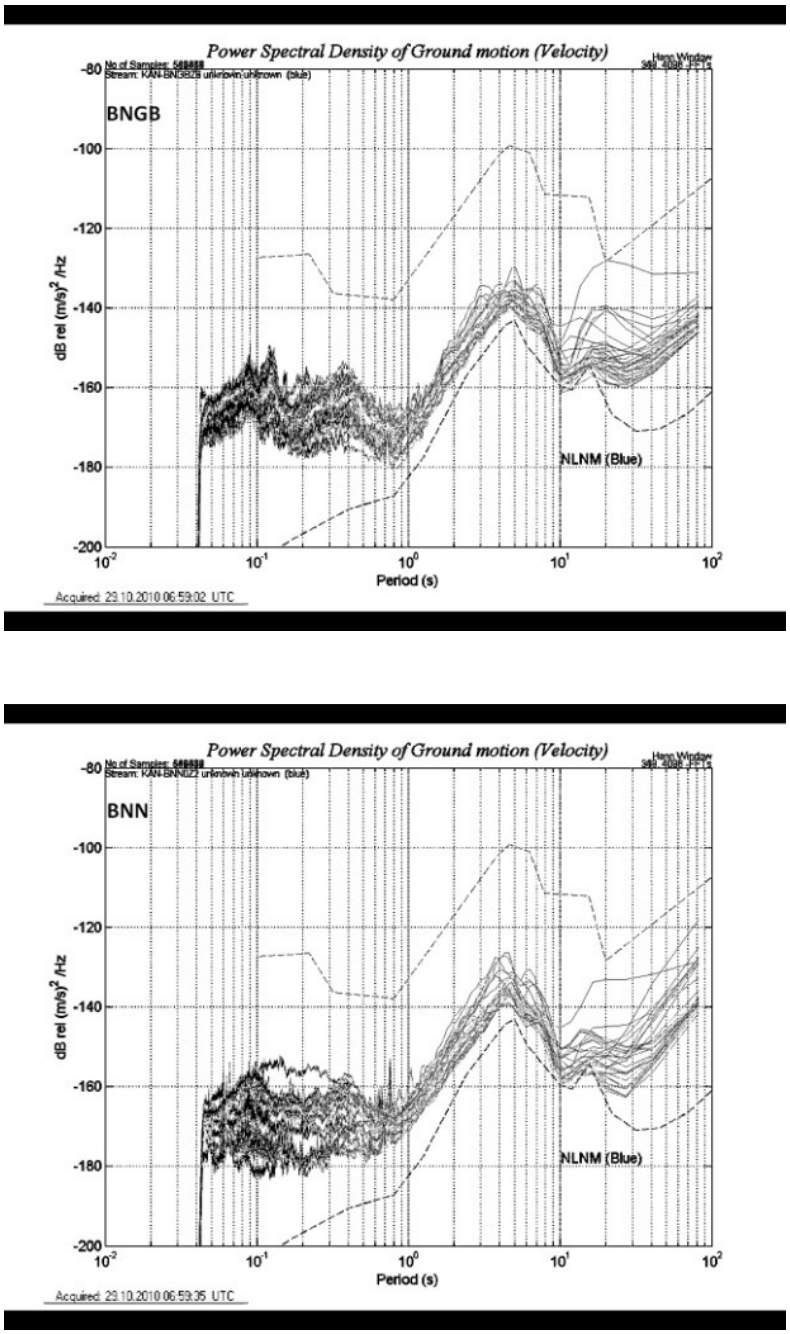

Figure B.7. PSDs of BNGB and BNN

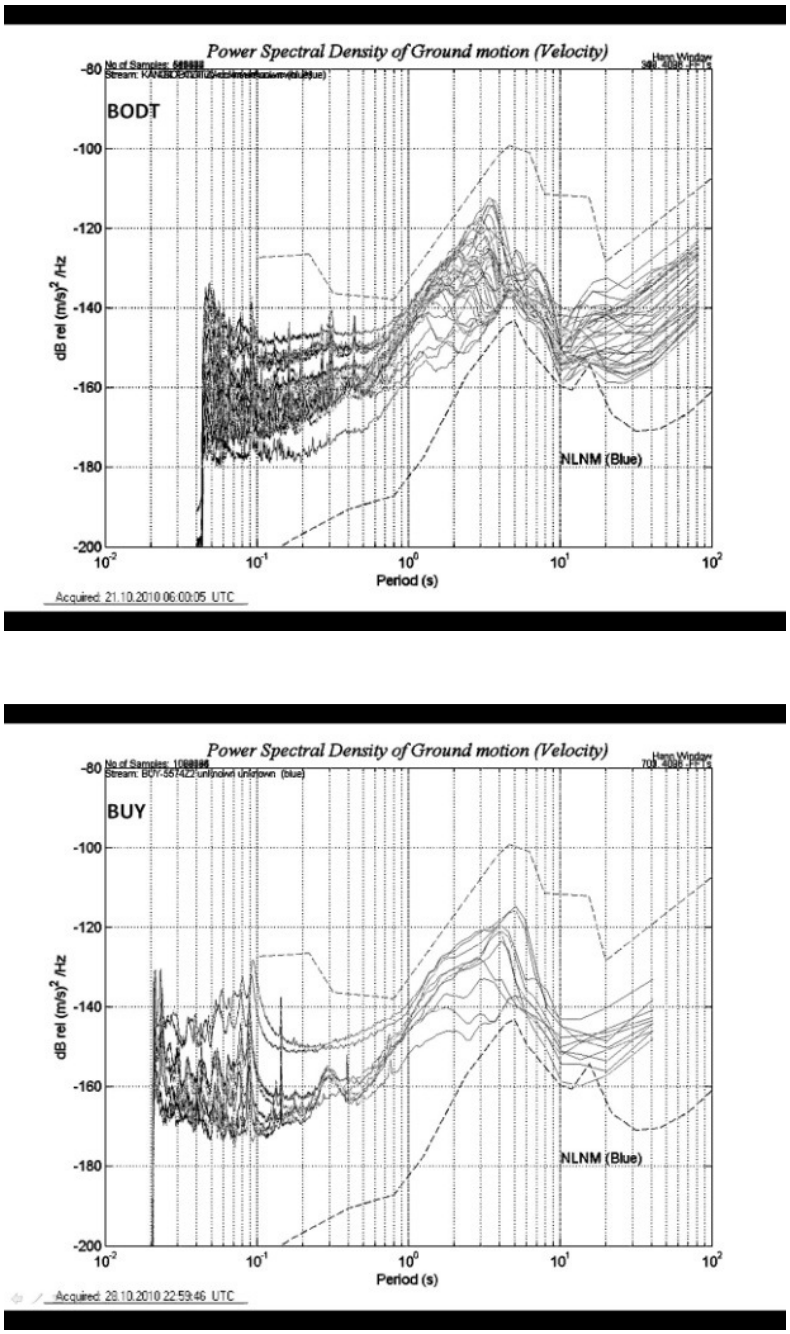

Figure B.8. PSDs of BODT and BUY

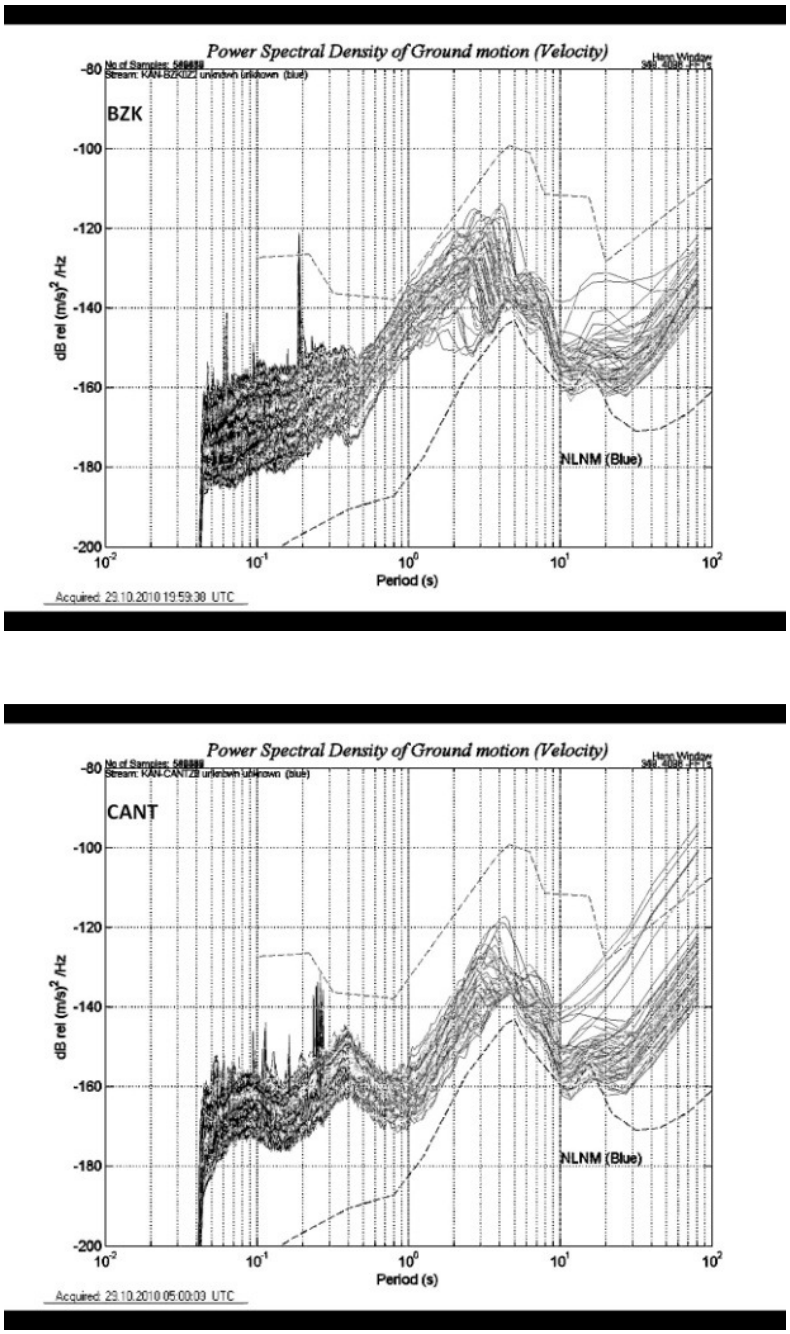

Figure B.9. PSDs of BZK and CANT

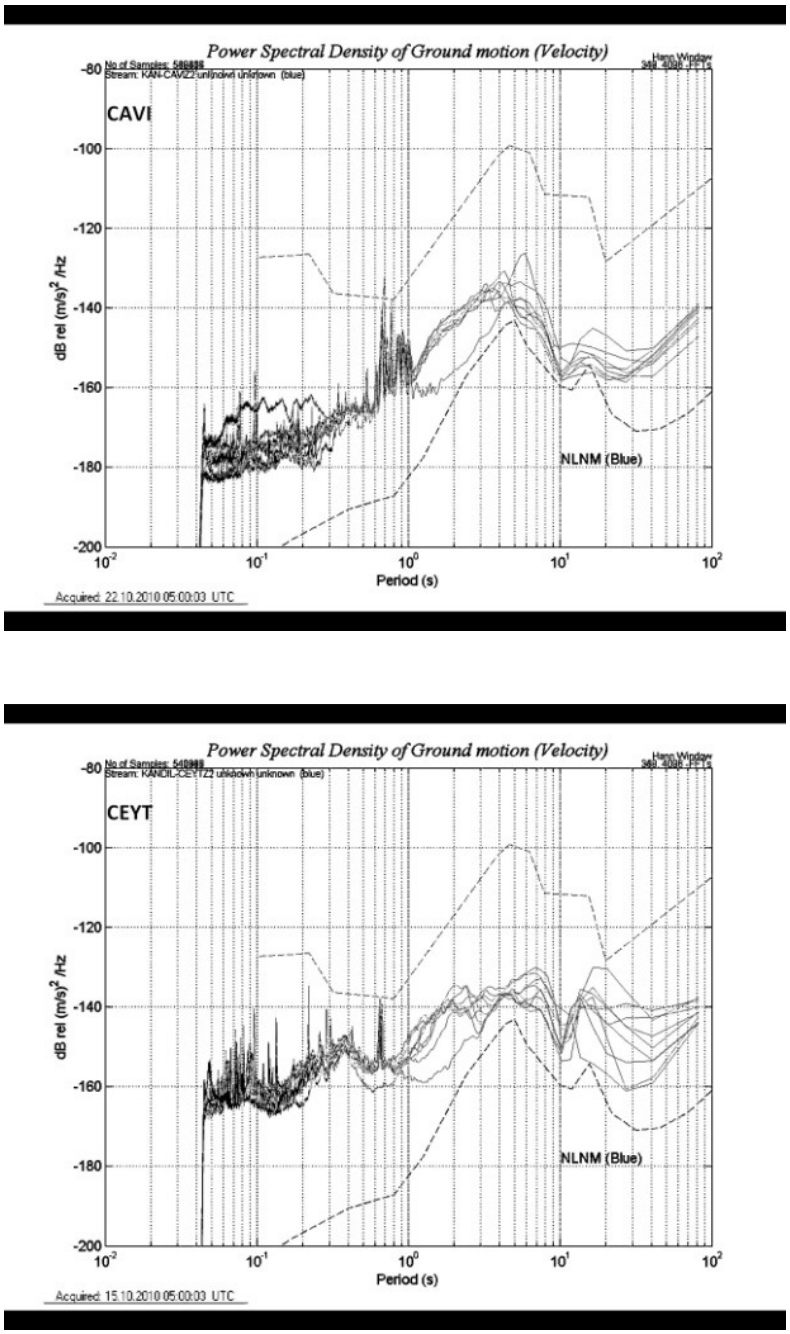

Figure B.10. PSDs of CAVI and CEYT

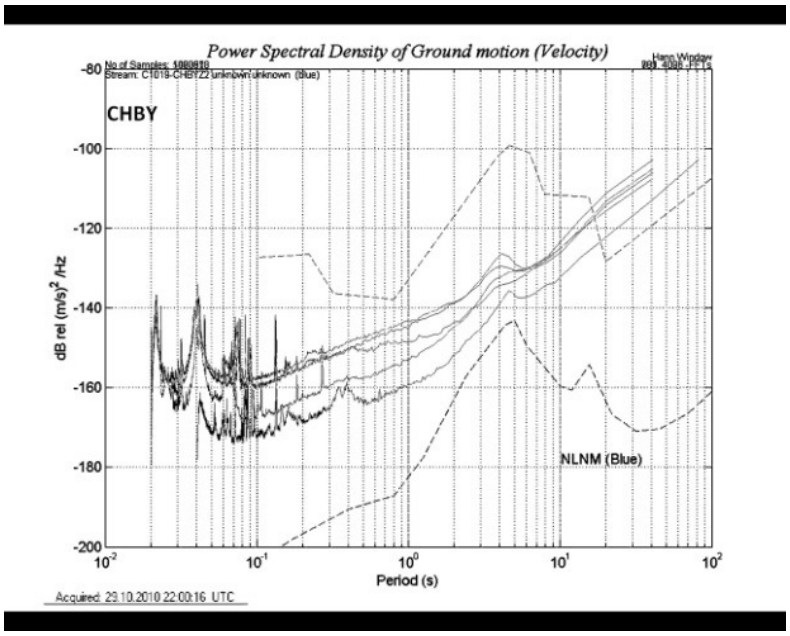

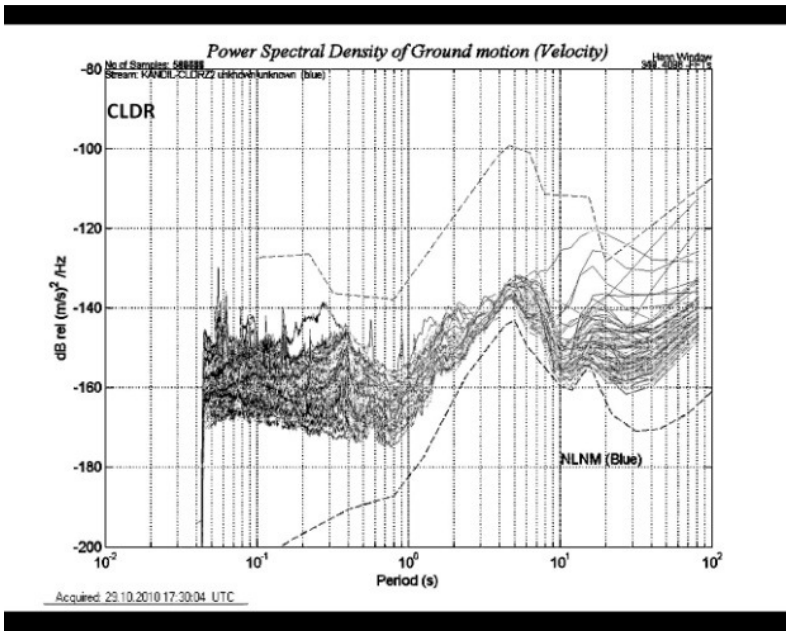

Figure B.11. PSDs of CHBY and CLDR

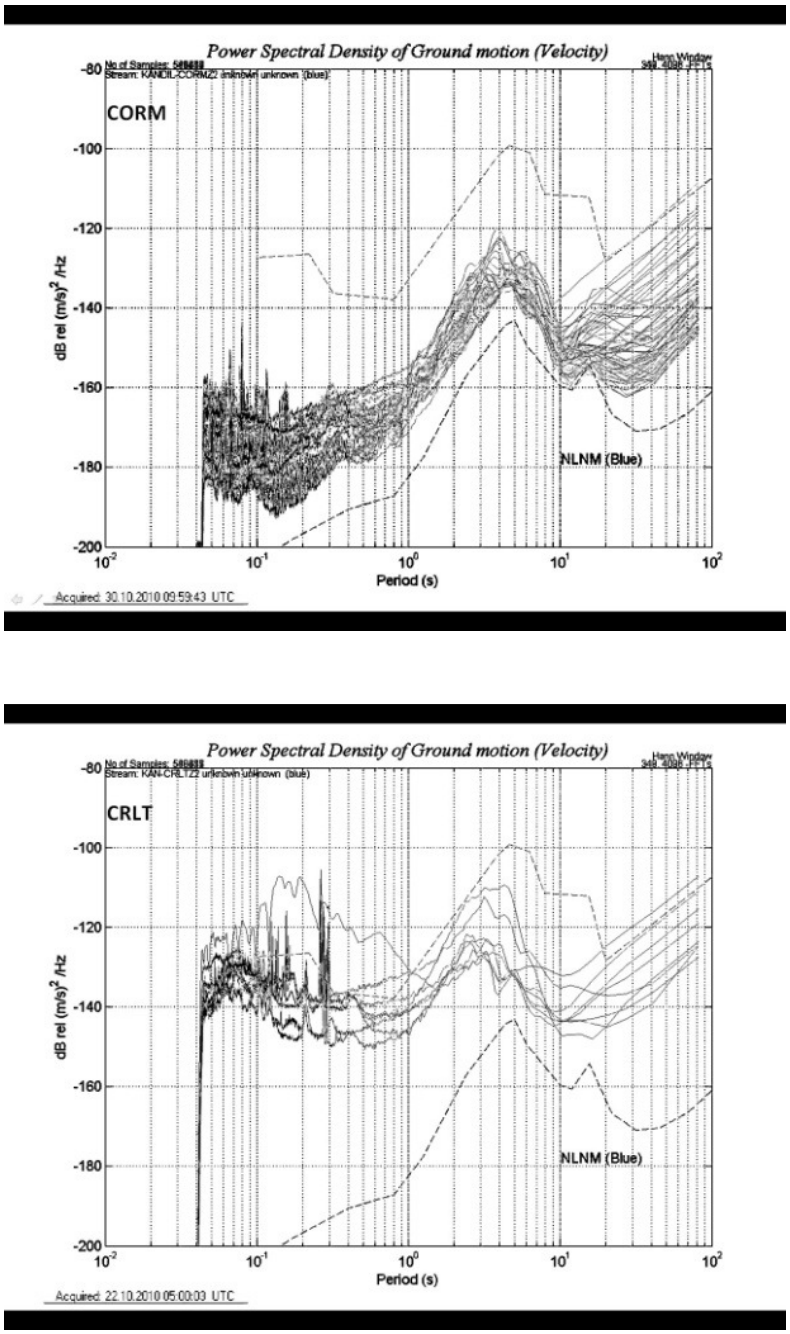

Figure B.12. PSDs of CORM and CRLT

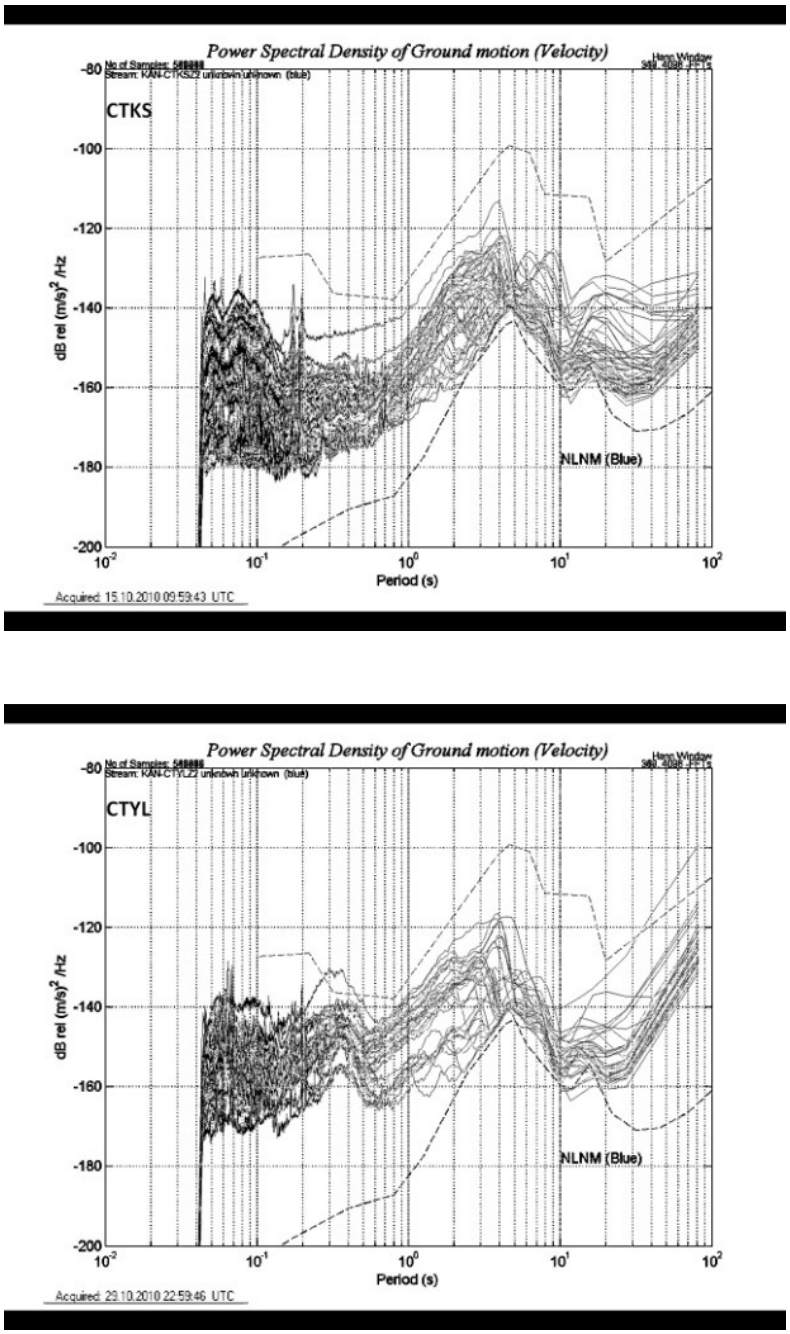

Figure B.13. PSDs of CTKS and CTYL

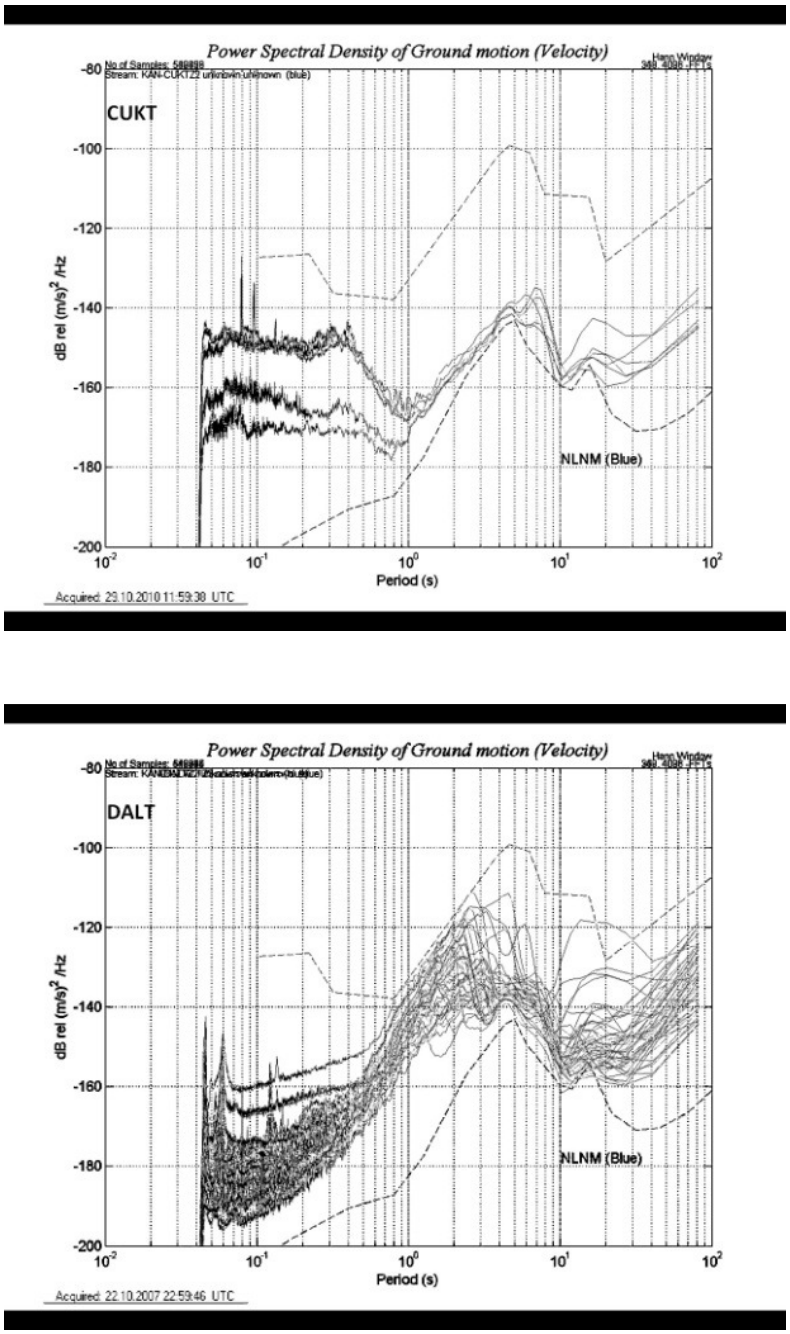

Figure B.14. PSDs of CUKT and DALT

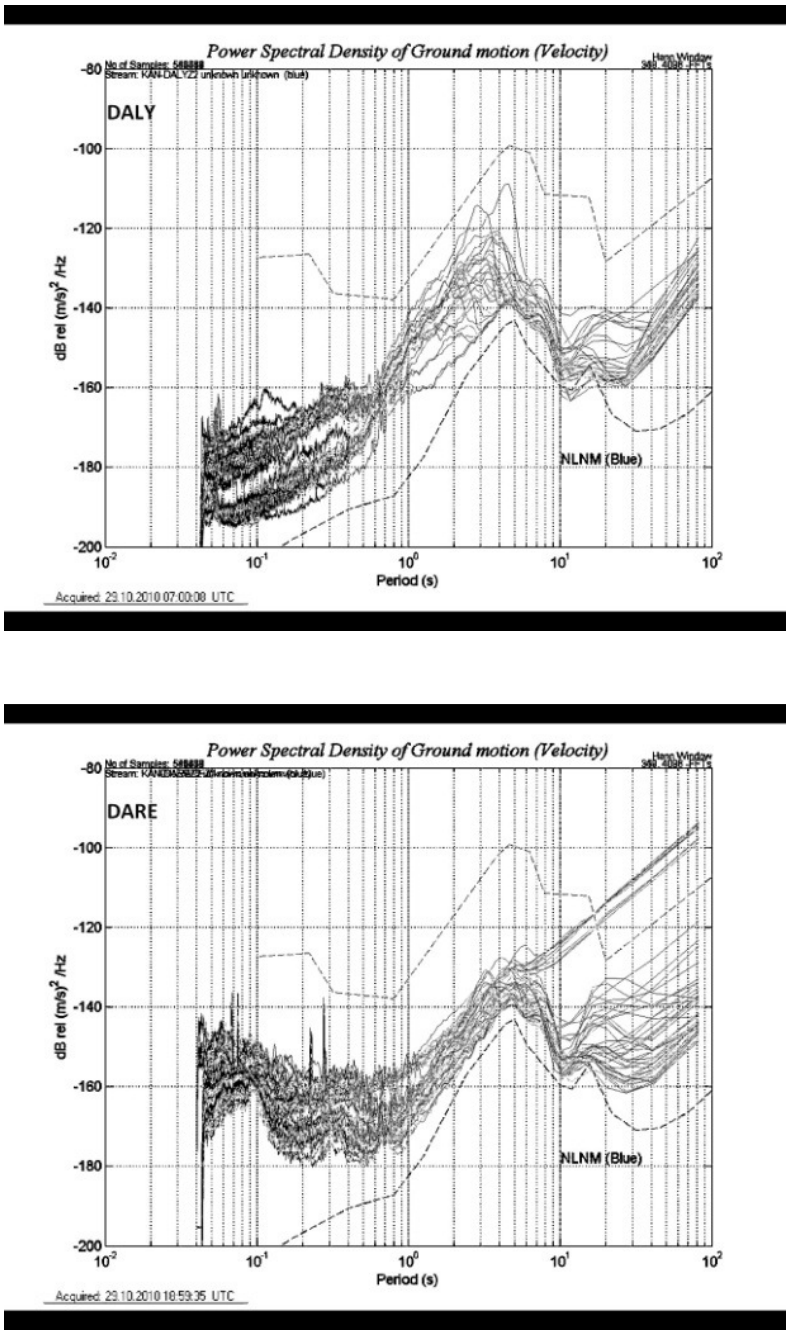

Figure B.15. PSDs of DALY and DARE

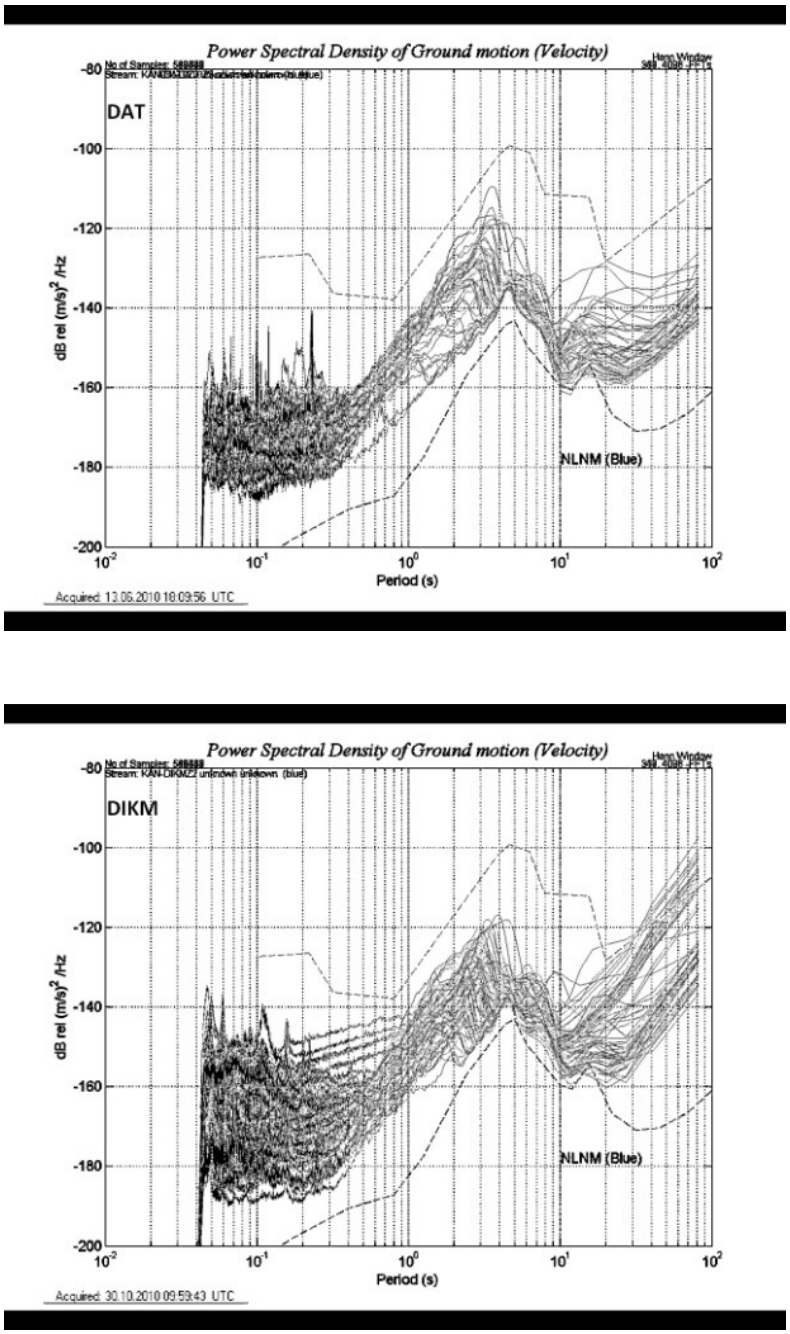

Figure B.16. PSDs of DAT and DIKM

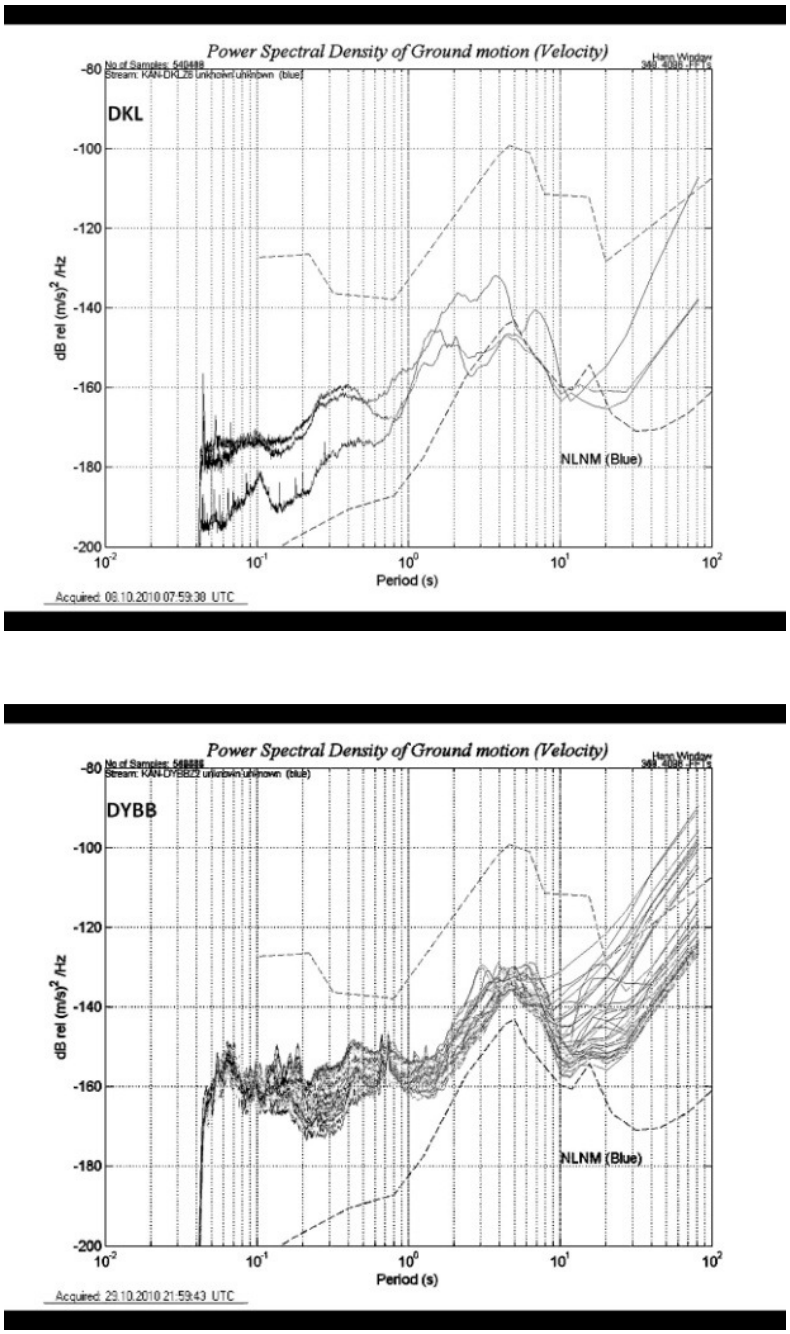

Figure B.17. PSDs of DKL and DYBB

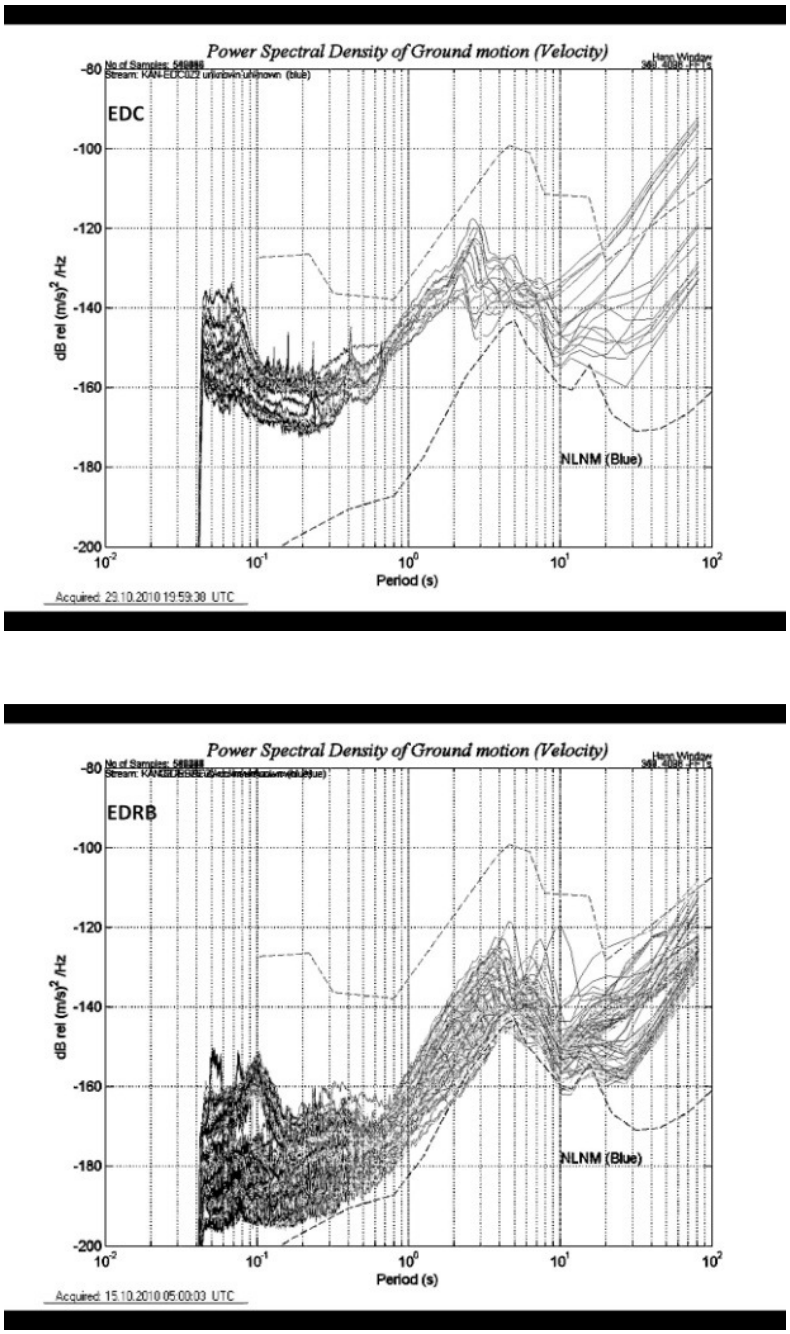

Figure B.18. PSDs of EDC and EDRB

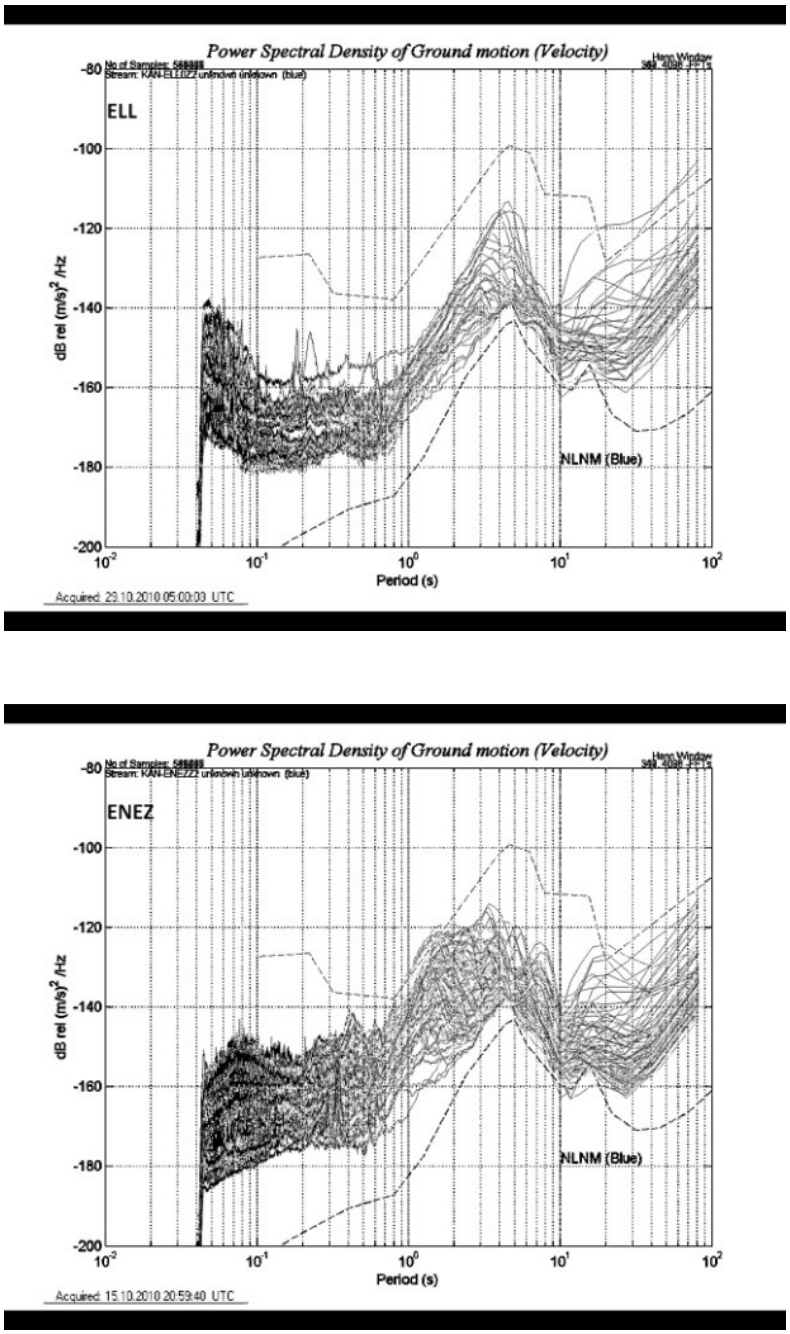

Figure B.19. PSDs of ELL and ENEZ

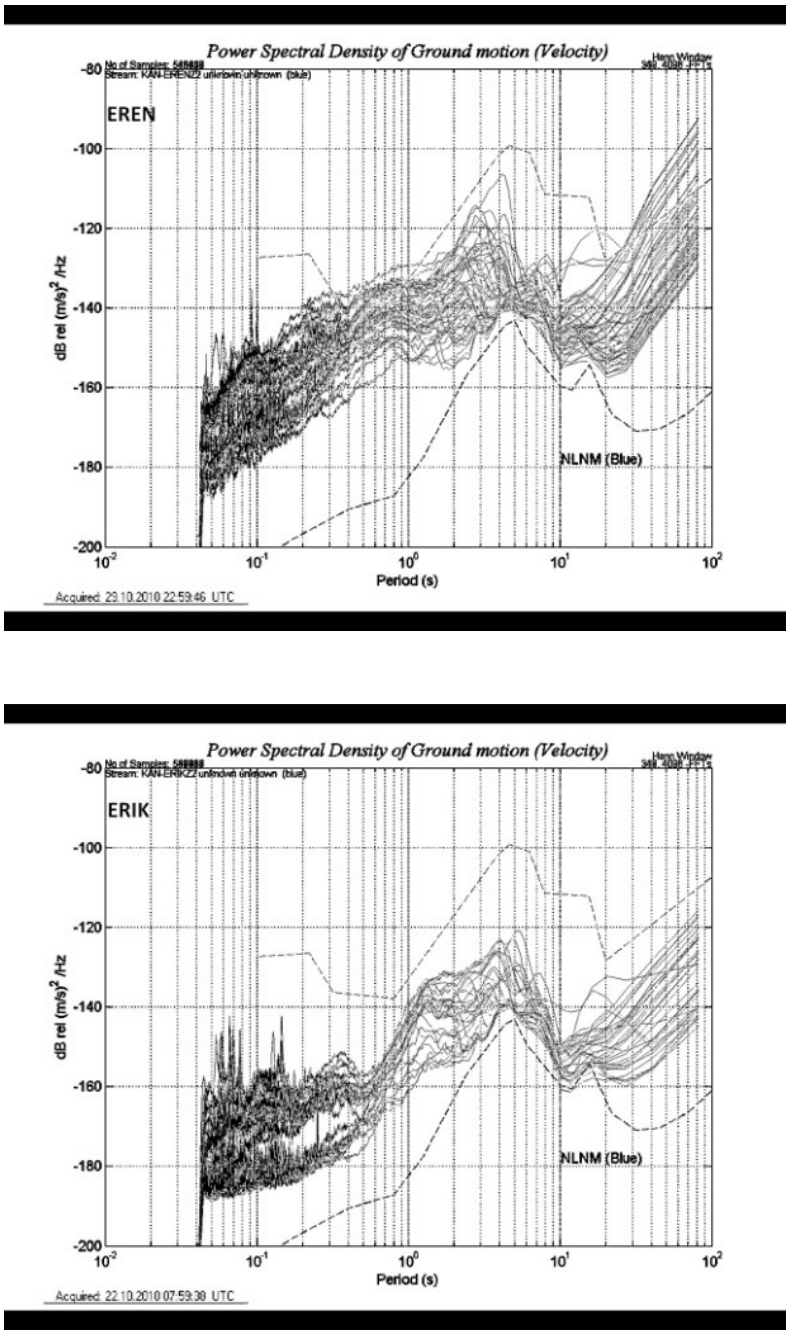

Figure B.20. PSDs of EREN and ERIK

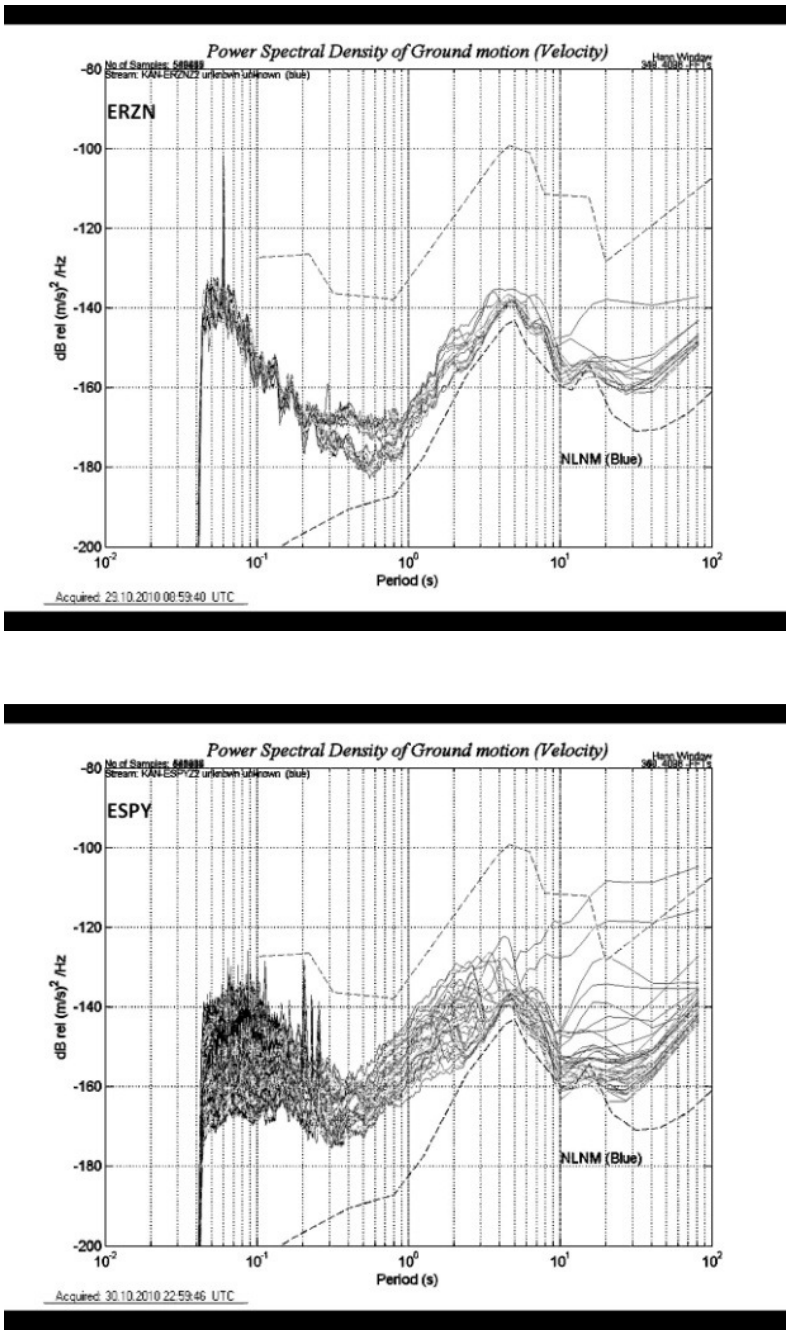

Figure B.21. PSDs of ERZN and ESPY

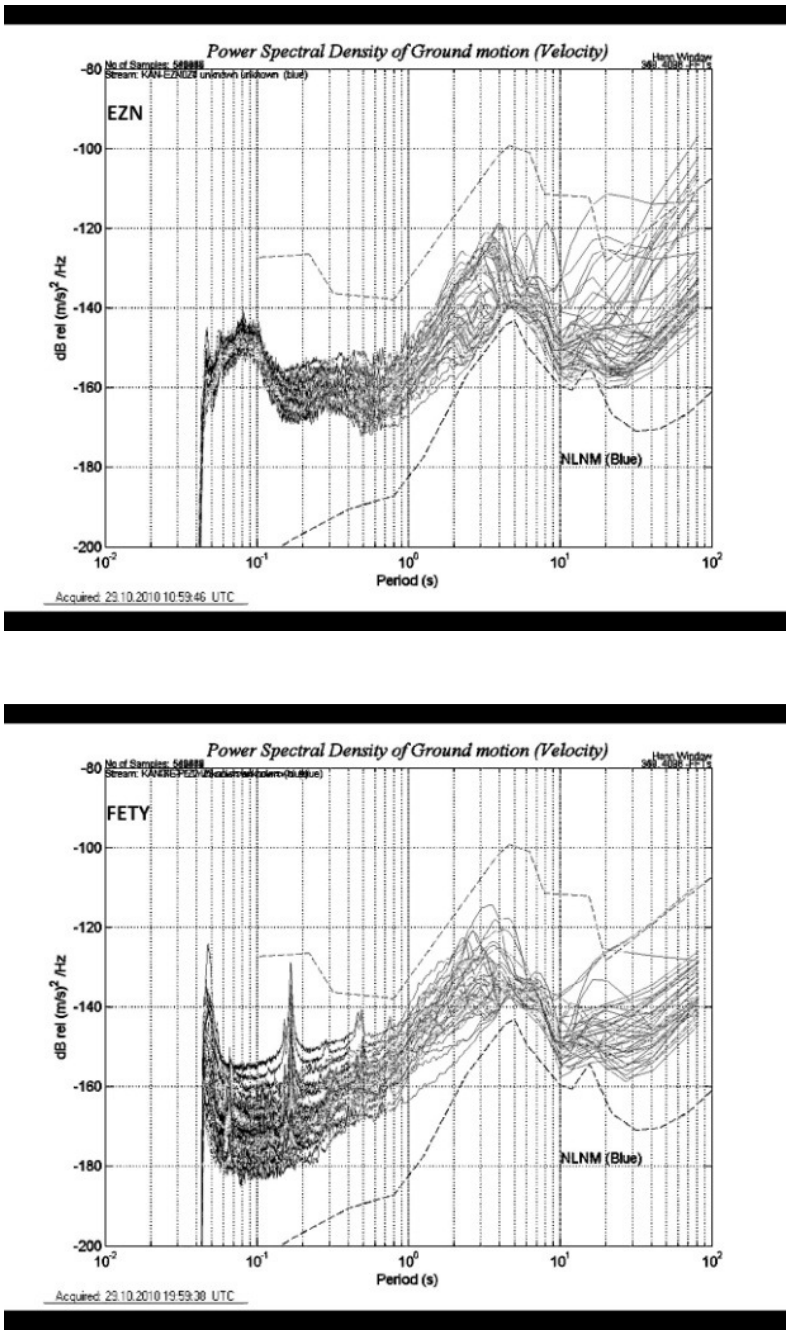

Figure B.22. PSDs of EZN and FETY

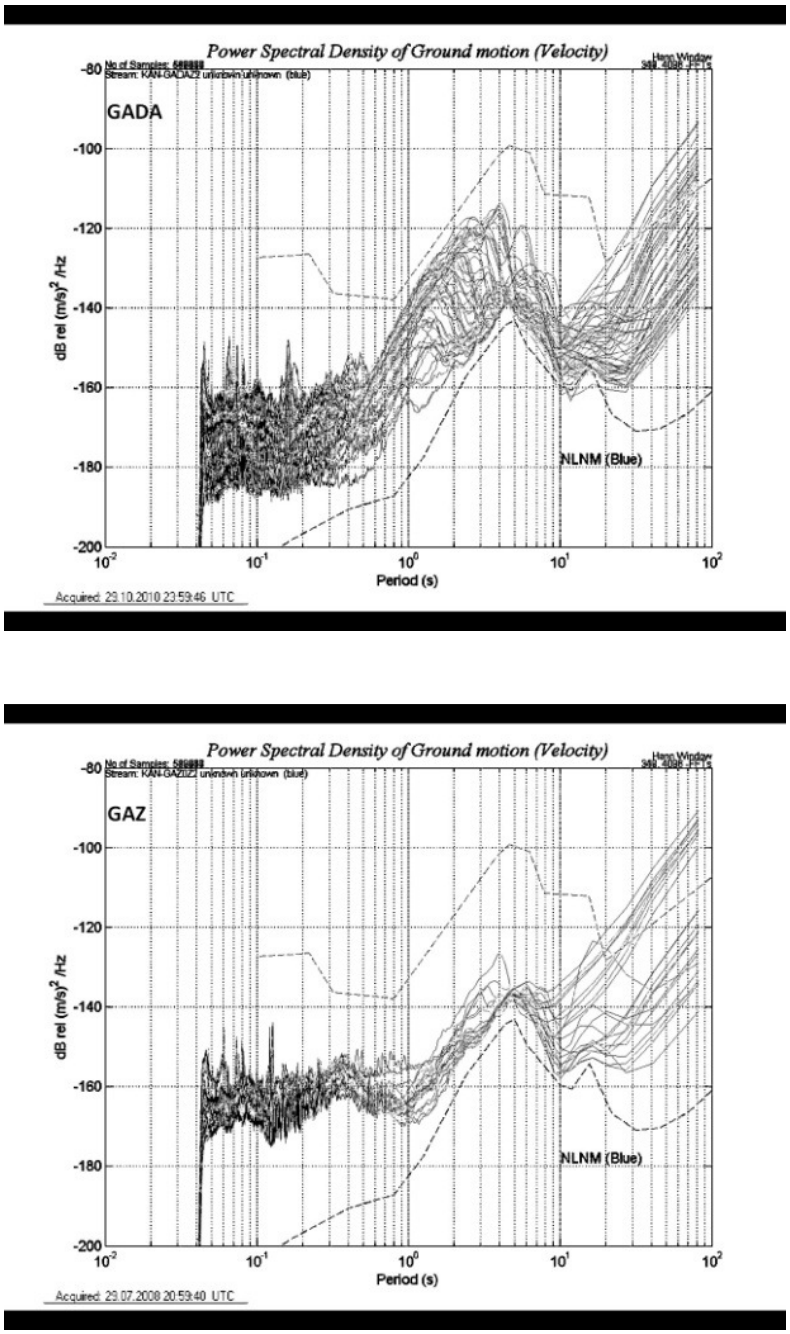

Figure B.23. PSDs of GADA and GAZ

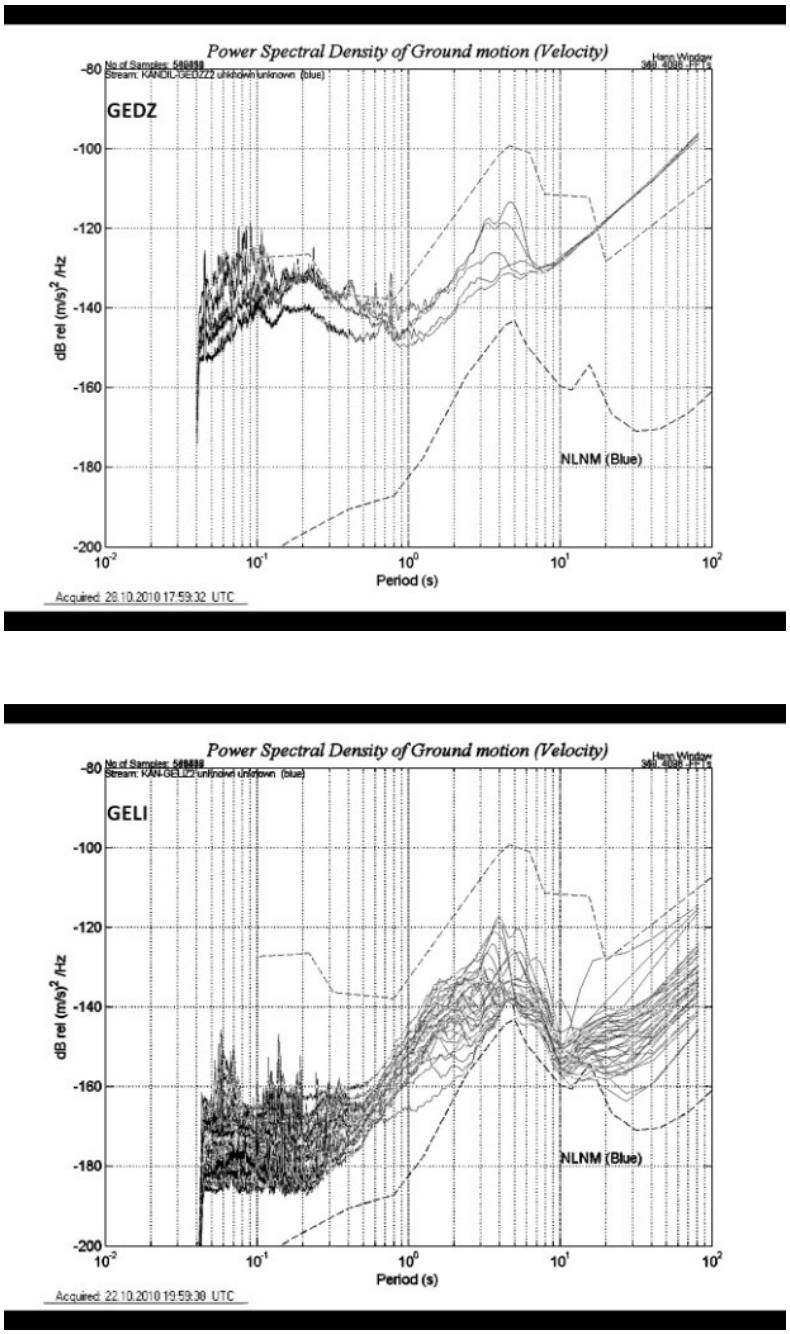

Figure B.24. PSDs of GEDZ and GELI

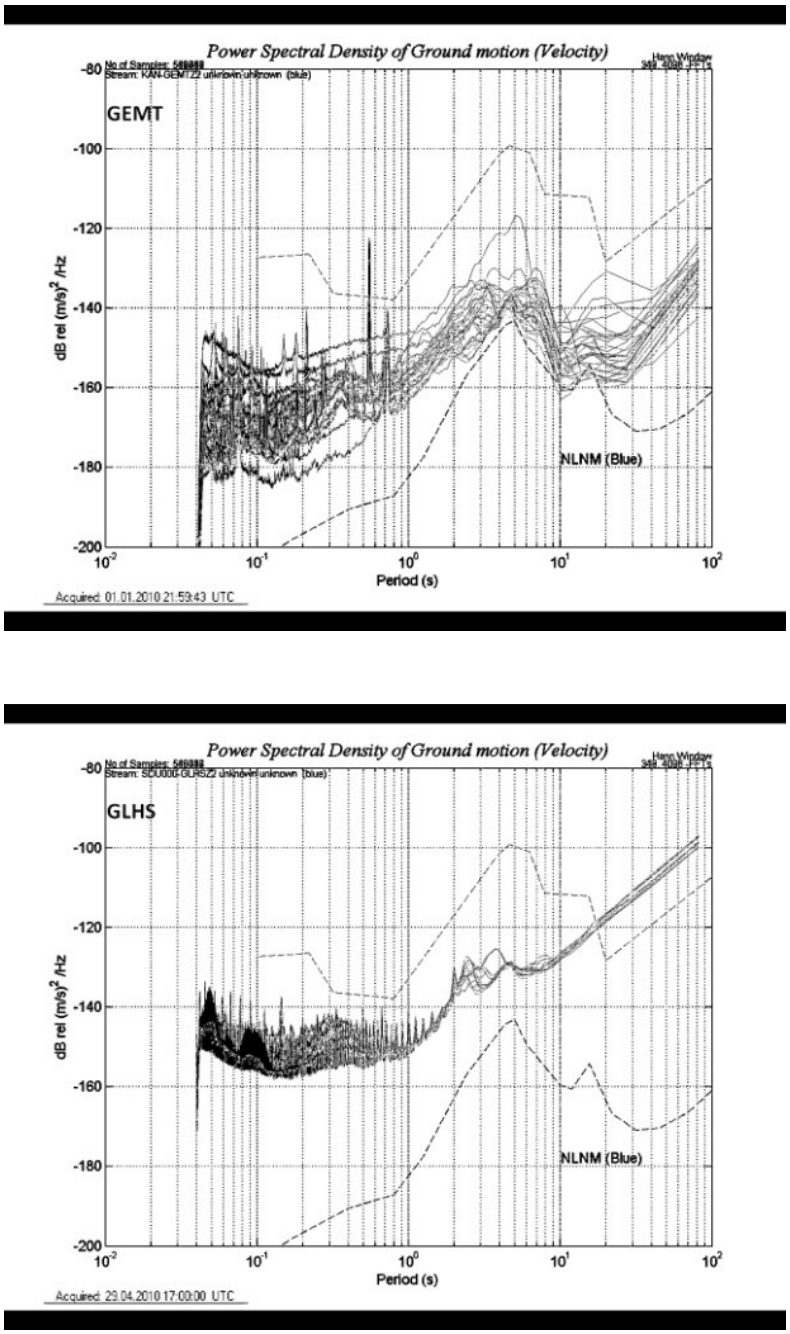

Figure B.25. PSDs of GEMT and GLHS

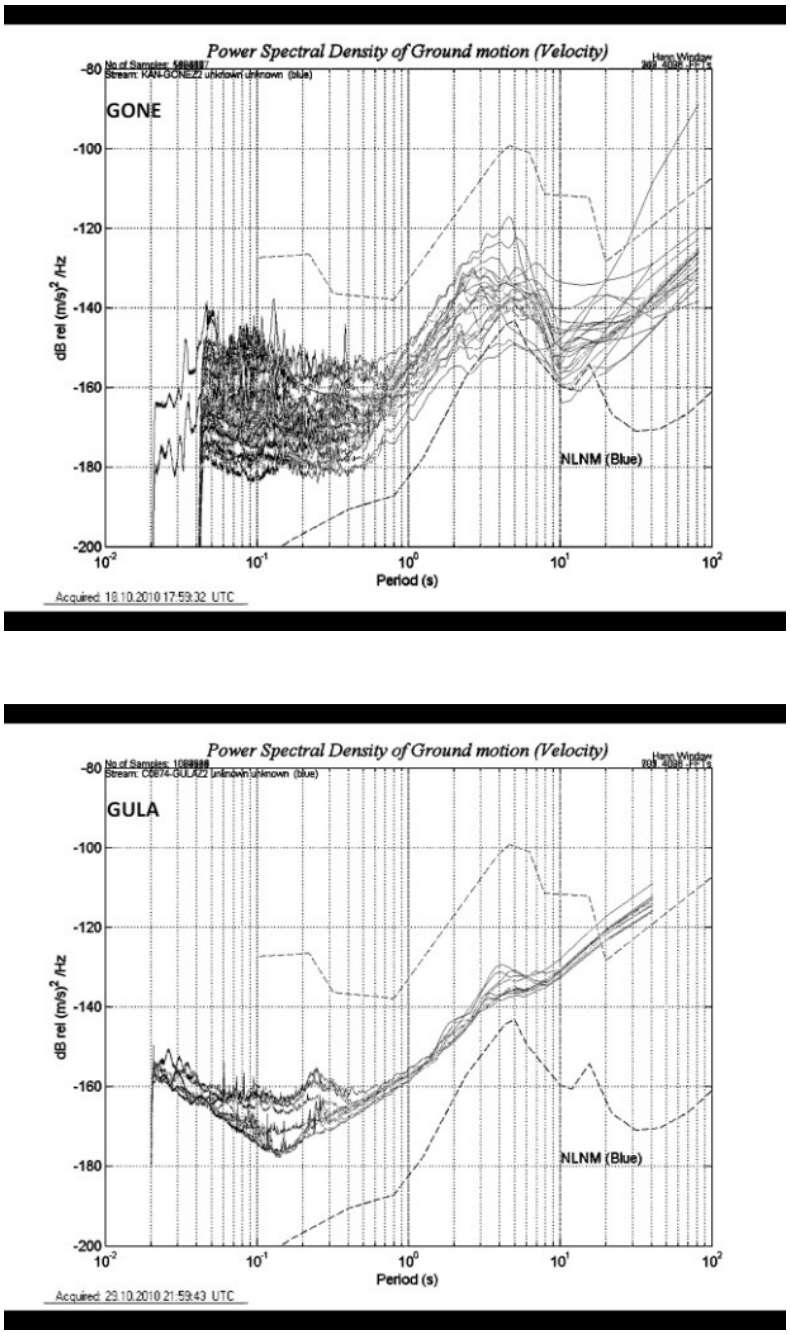

Figure B.26. PSDs of GONE and GULA

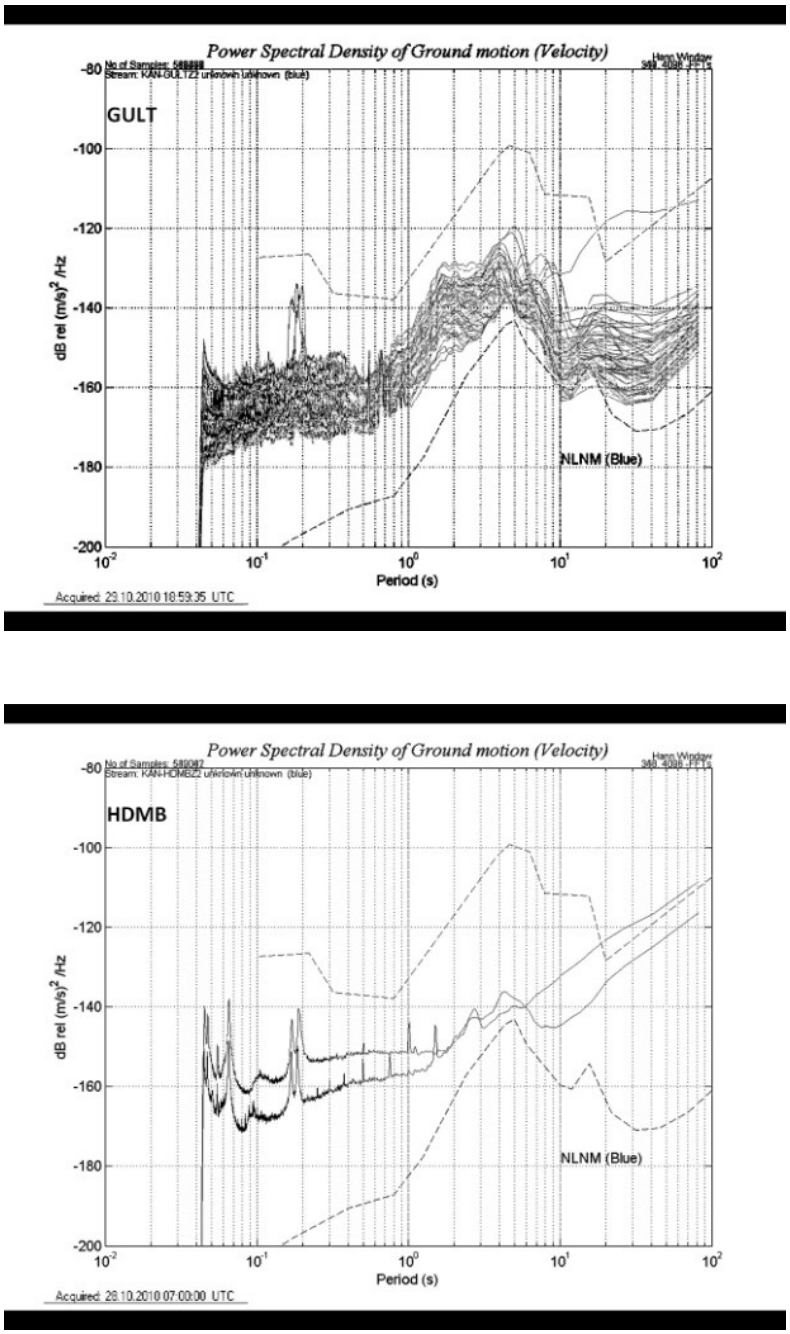

Figure B.27. PSDs of GULT and HDMB

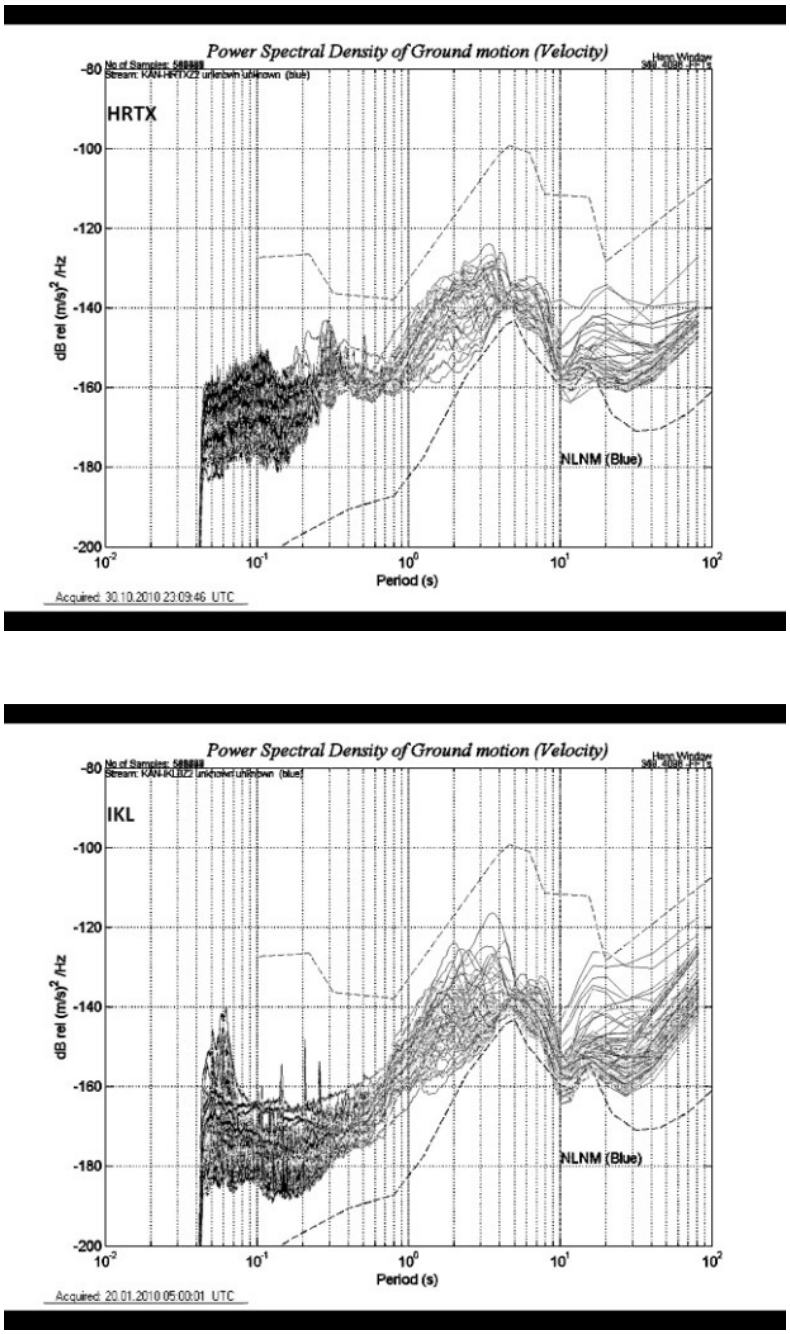

Figure B.28. PSDs of HRTX and IKL

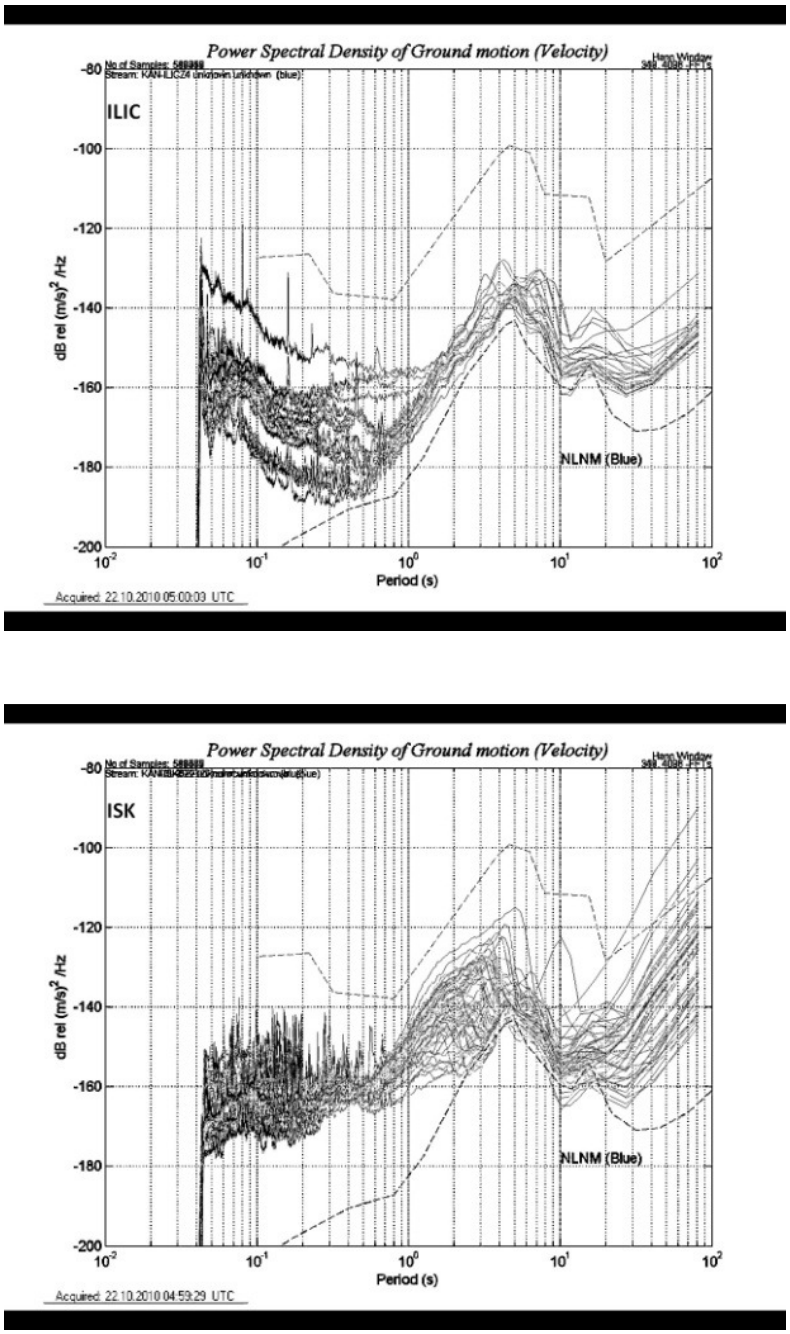

Figure B.29. PSDs of ILIC and ISK

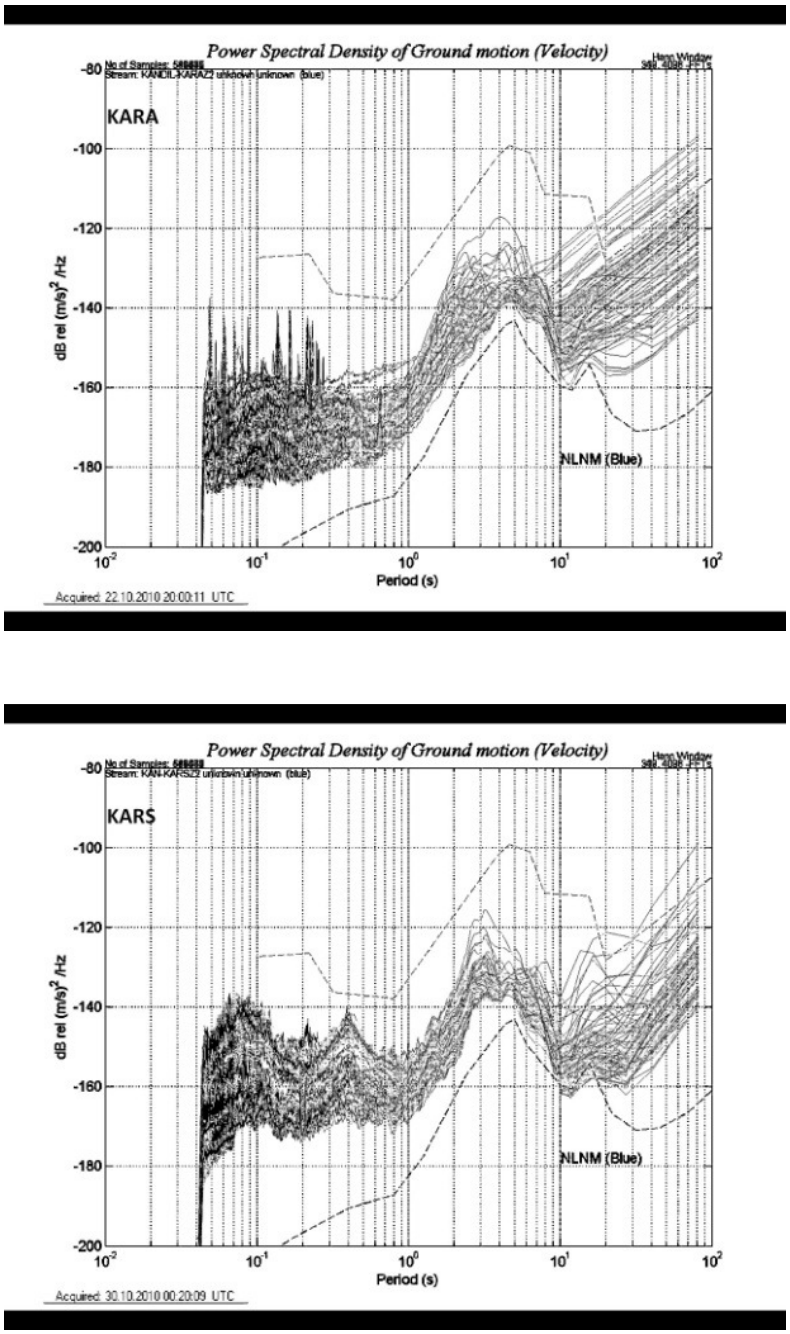

Figure B.30. PSDs of KARA and KARS

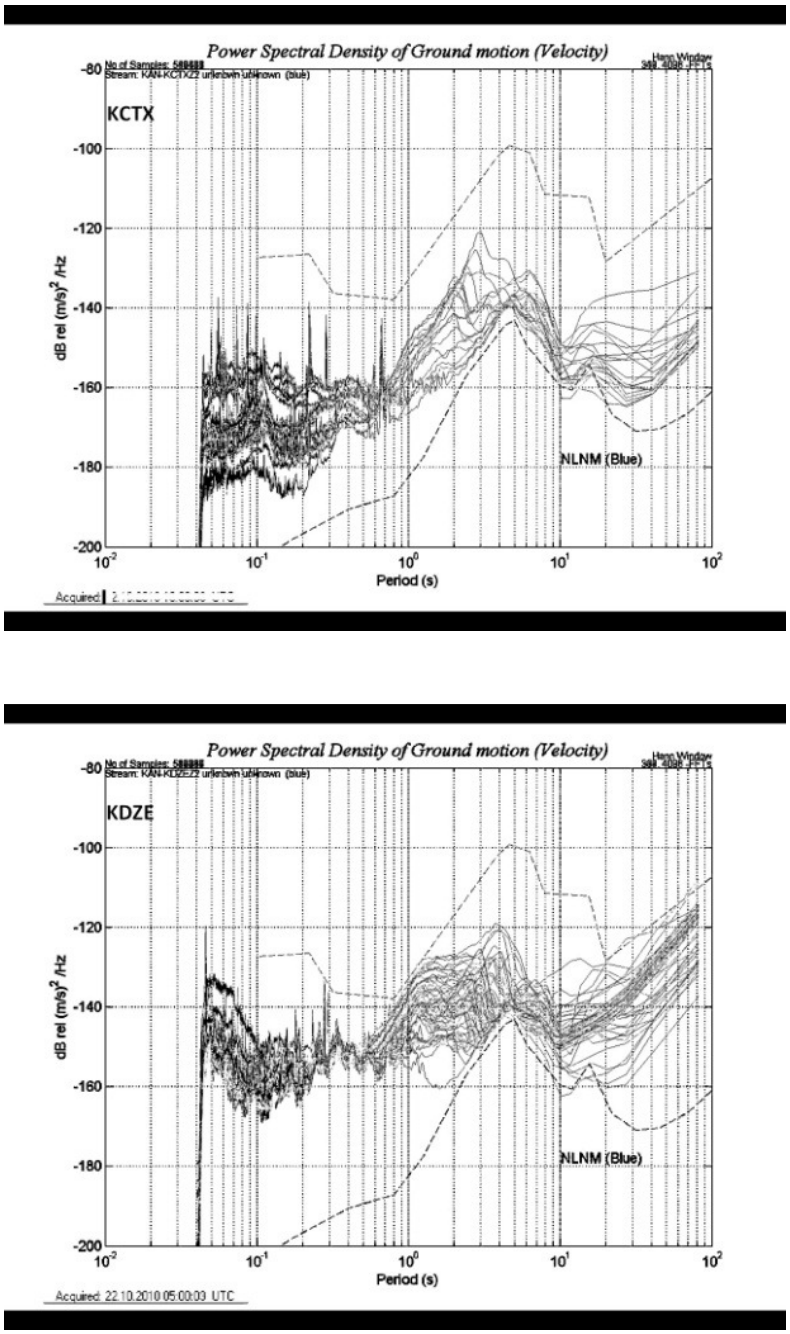

Figure B.31. PSDs of KCTX and KDZE

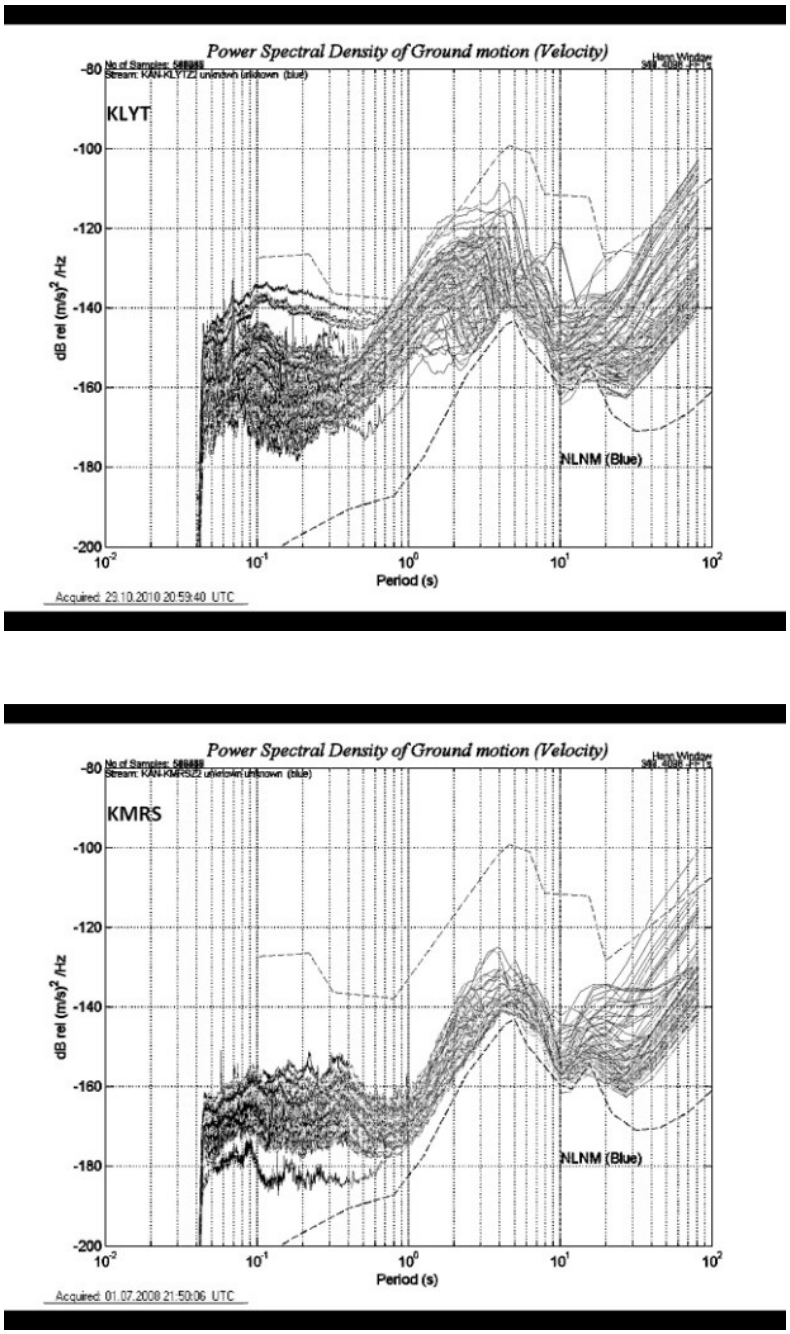

Figure B.32. PSDs of KLYT and KMRS

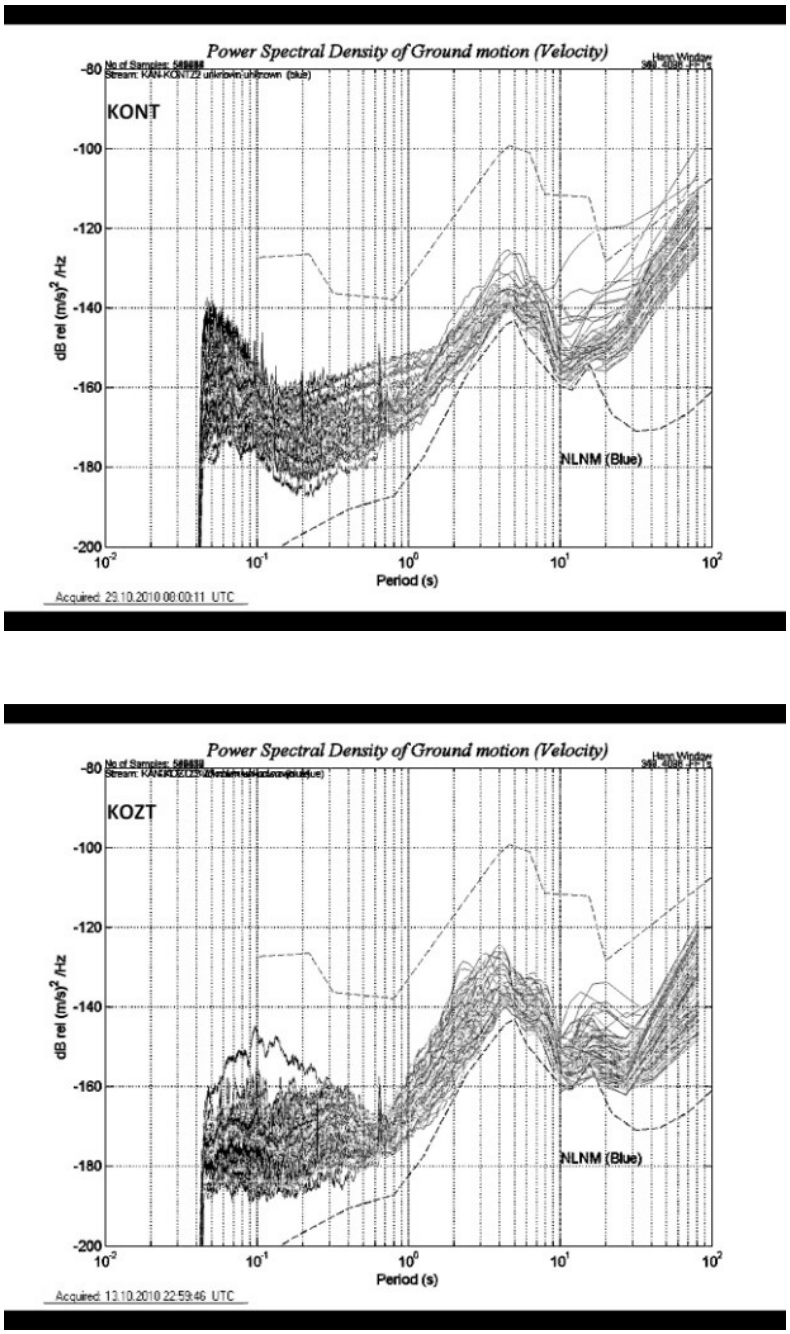

Figure B.33. PSDs of KONT and KOZT

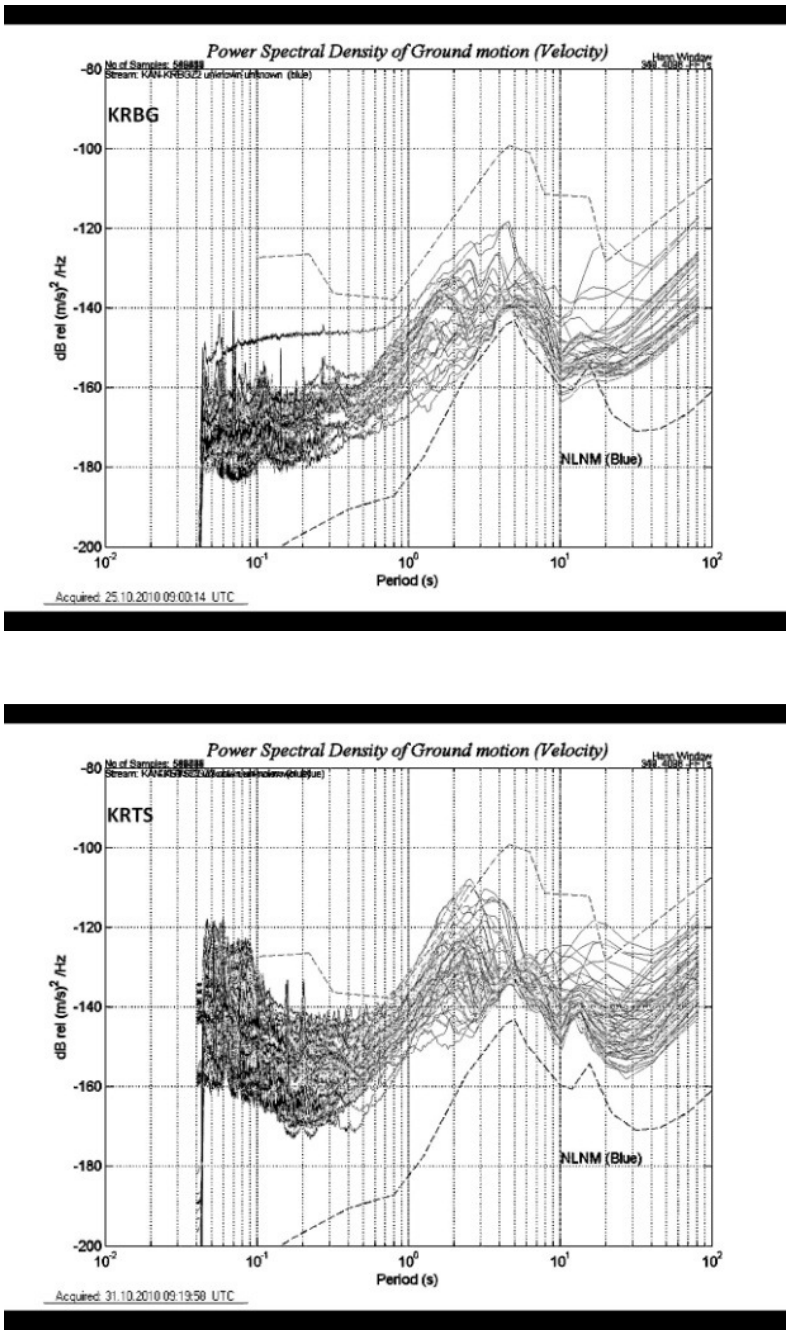

Figure B.34. PSDs of KRBG and KRTS

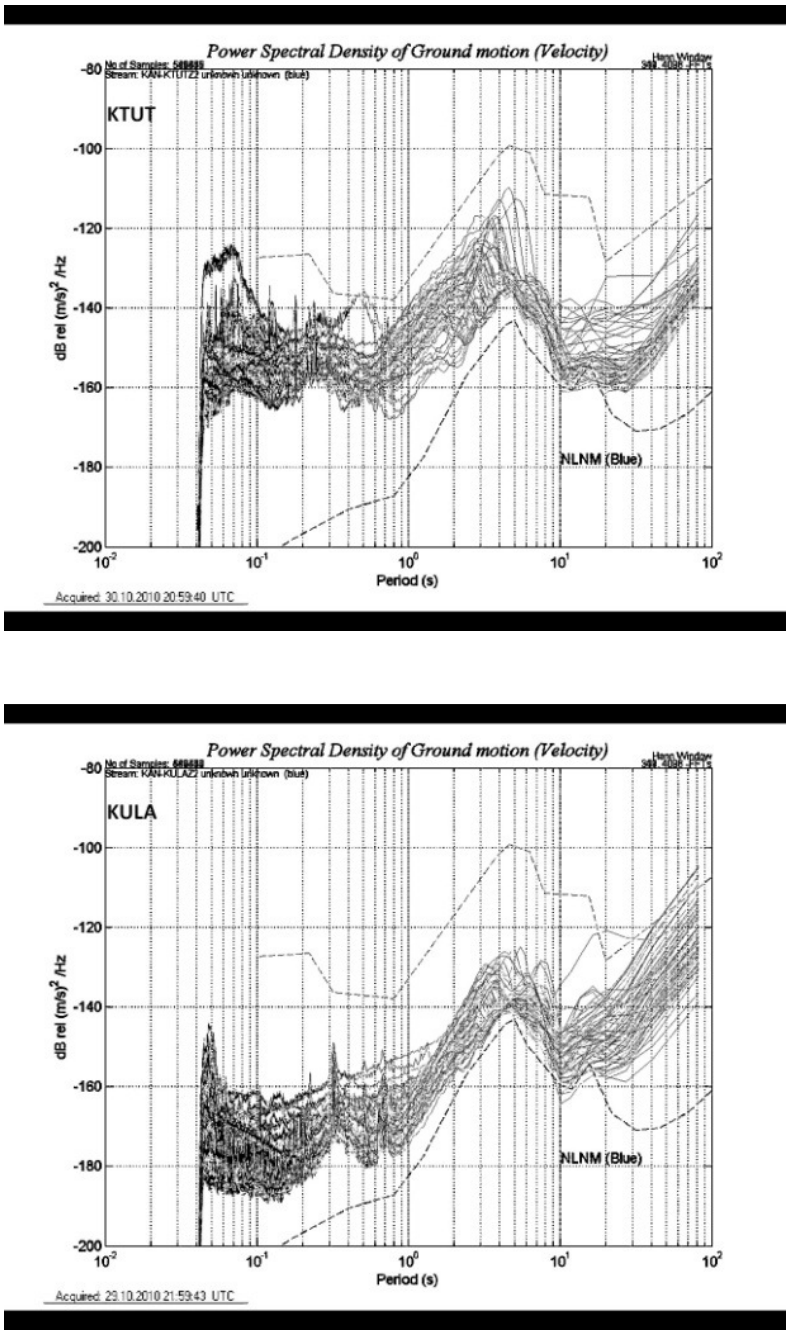

Figure B.35. PSDs of KTUT and KULA

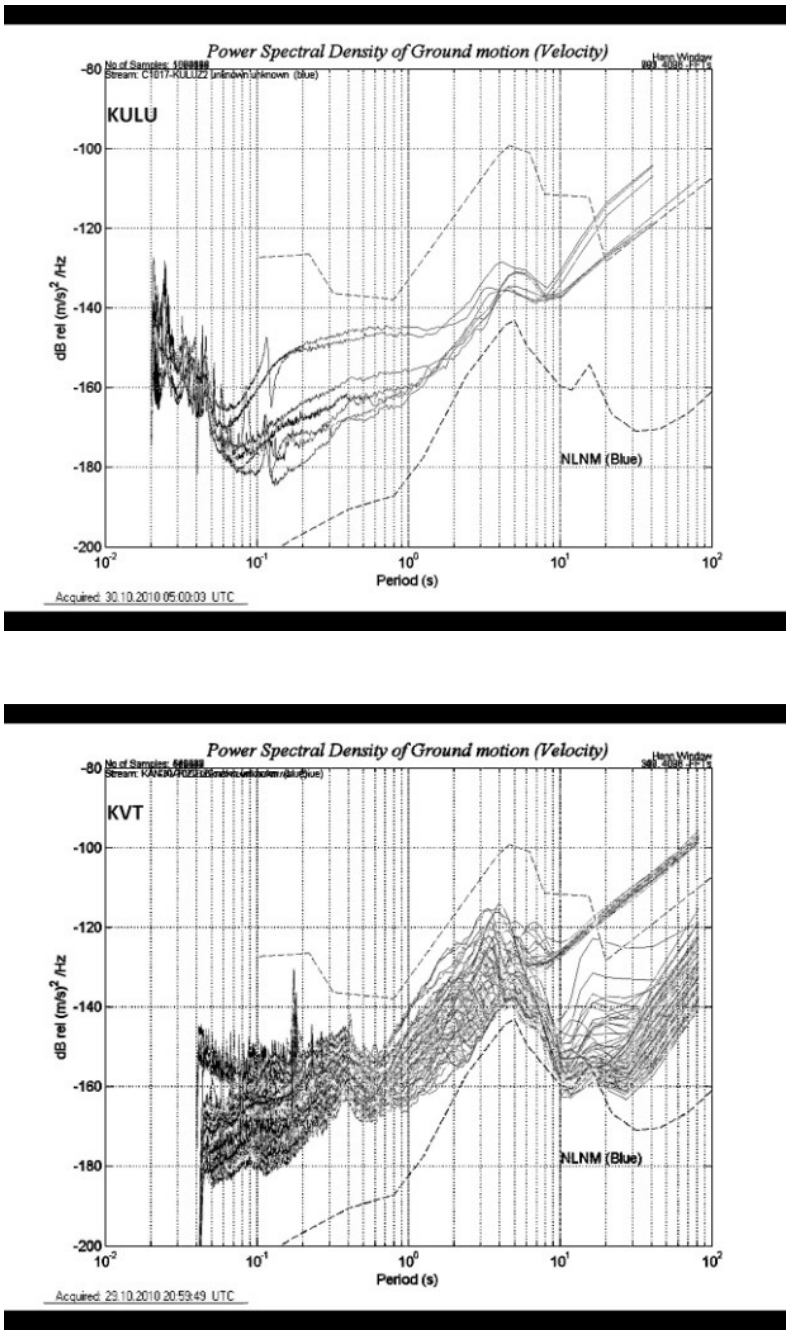

Figure B.36. PSDs of KULU and KVT

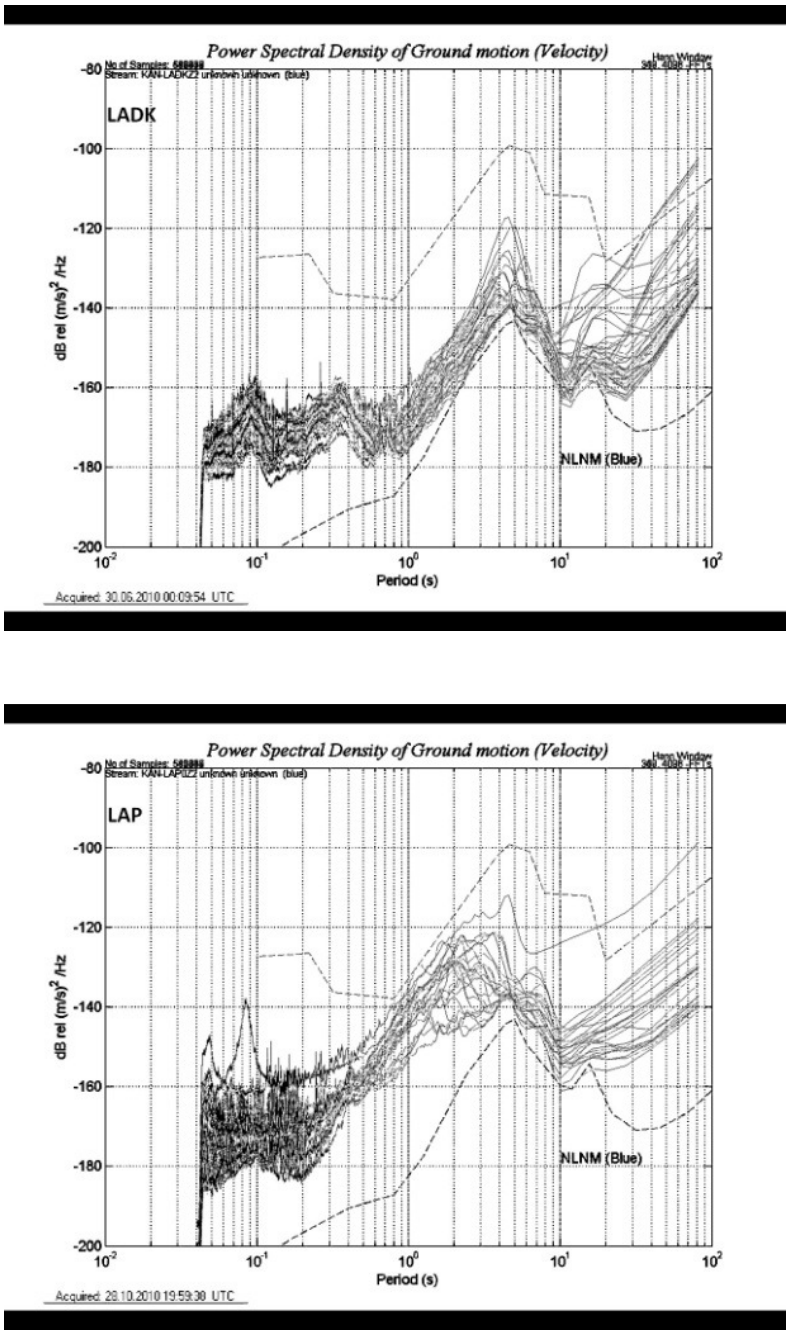

Figure B.37. PSDs of LADK and LAP

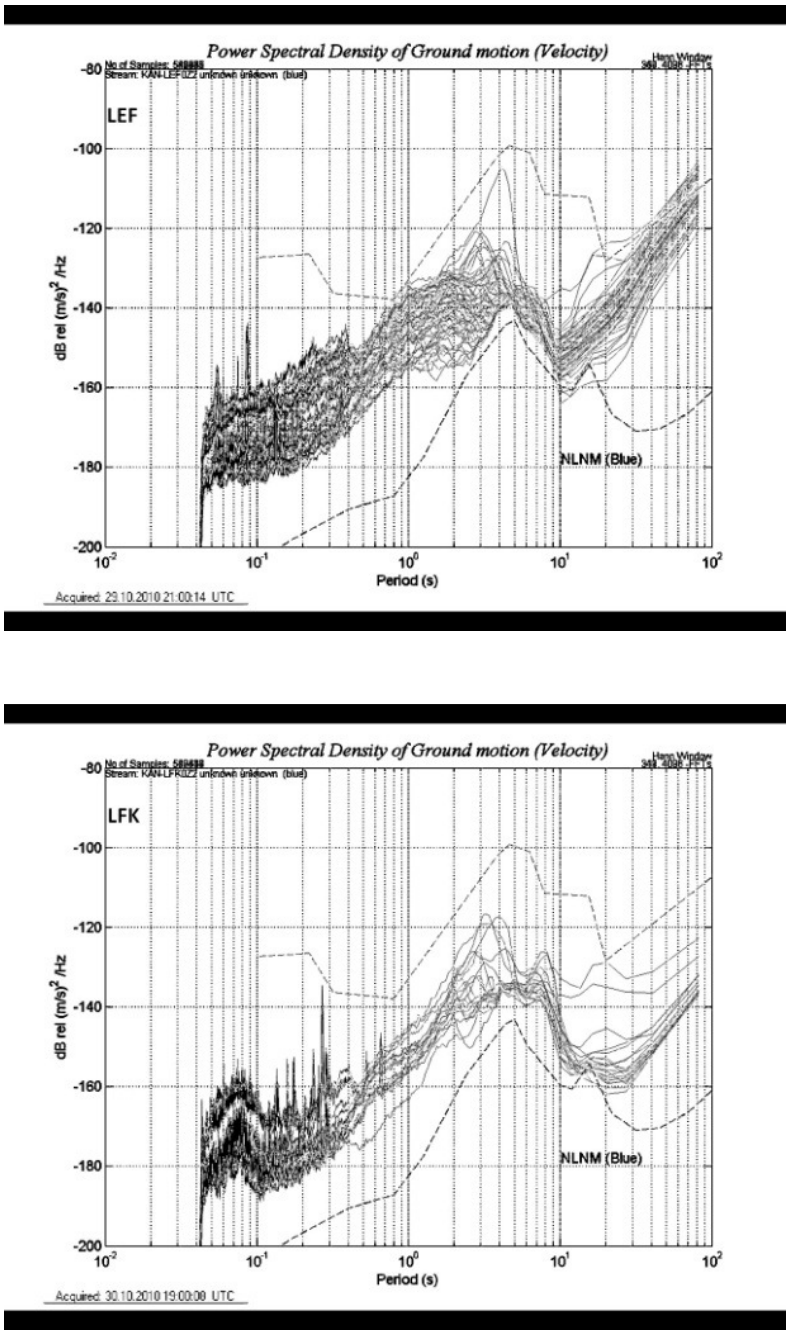

Figure B.38. PSDs of LEF and LFK

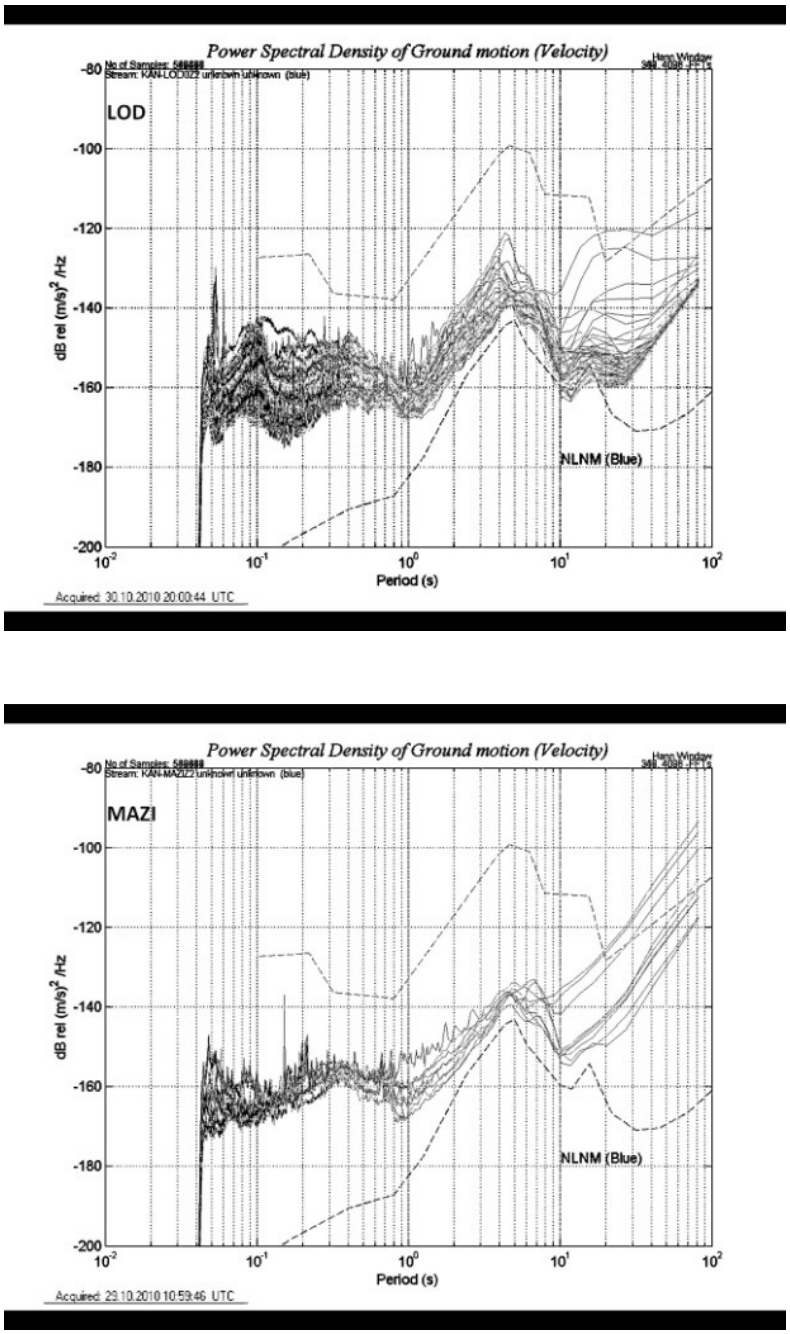

Figure B.39. PSDs of LOD and MAZI

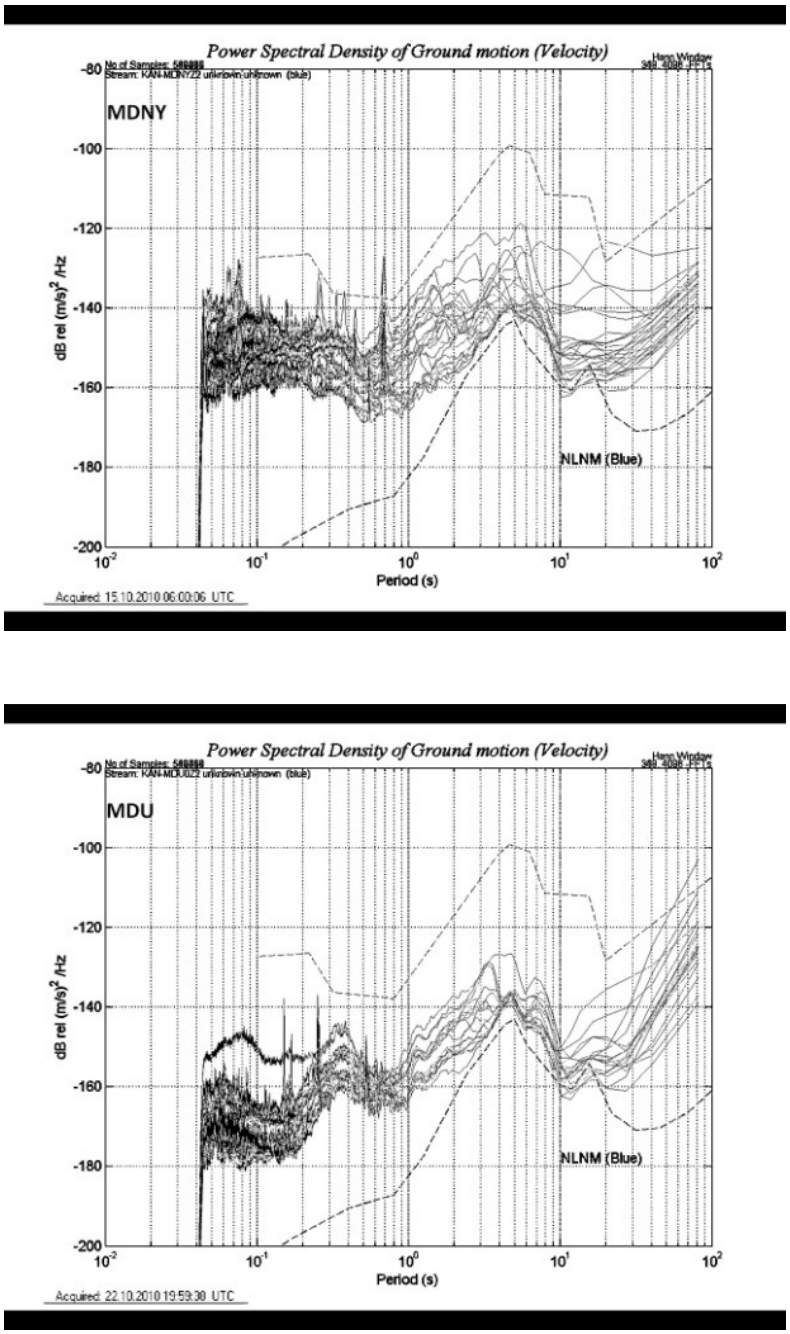

Figure B.40. PSDs of MDNY and MDU

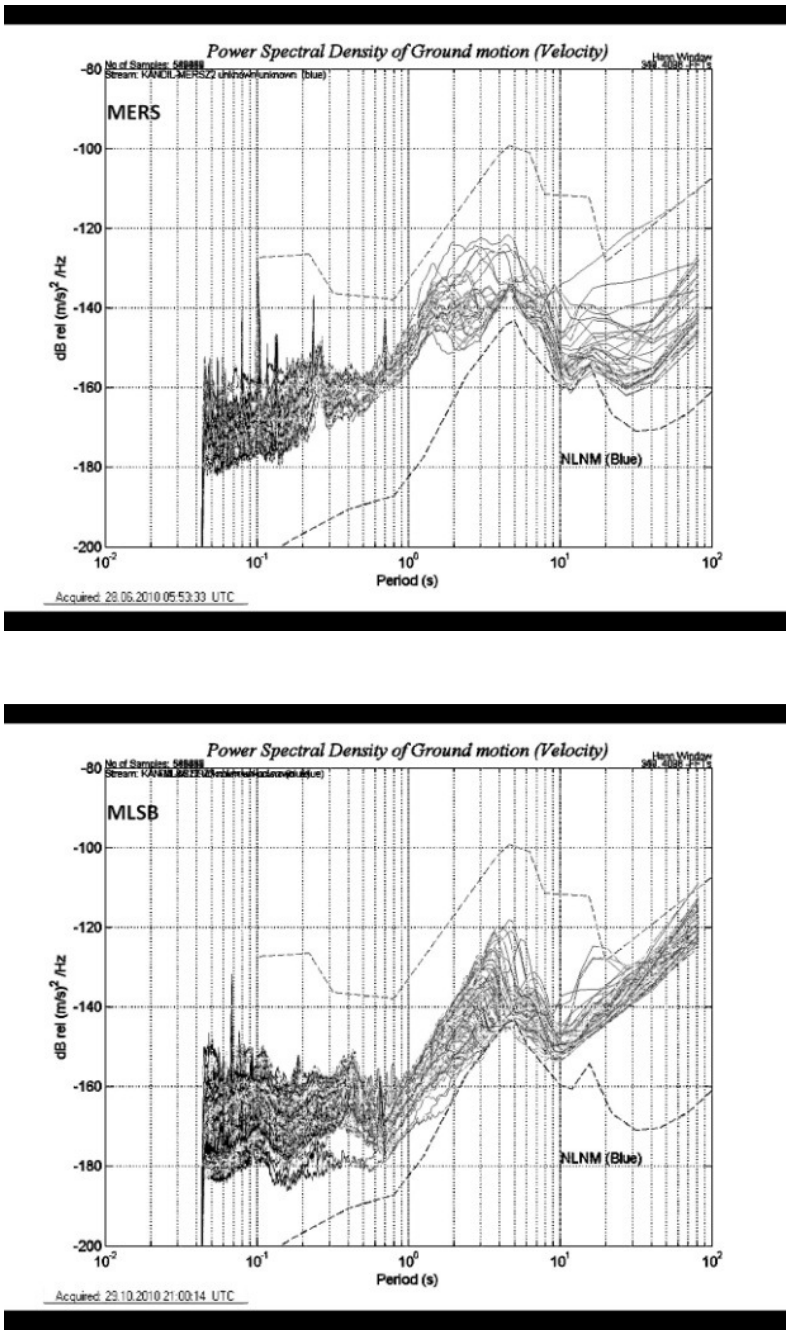

Figure B.41. PSDs of MERS and MLSB

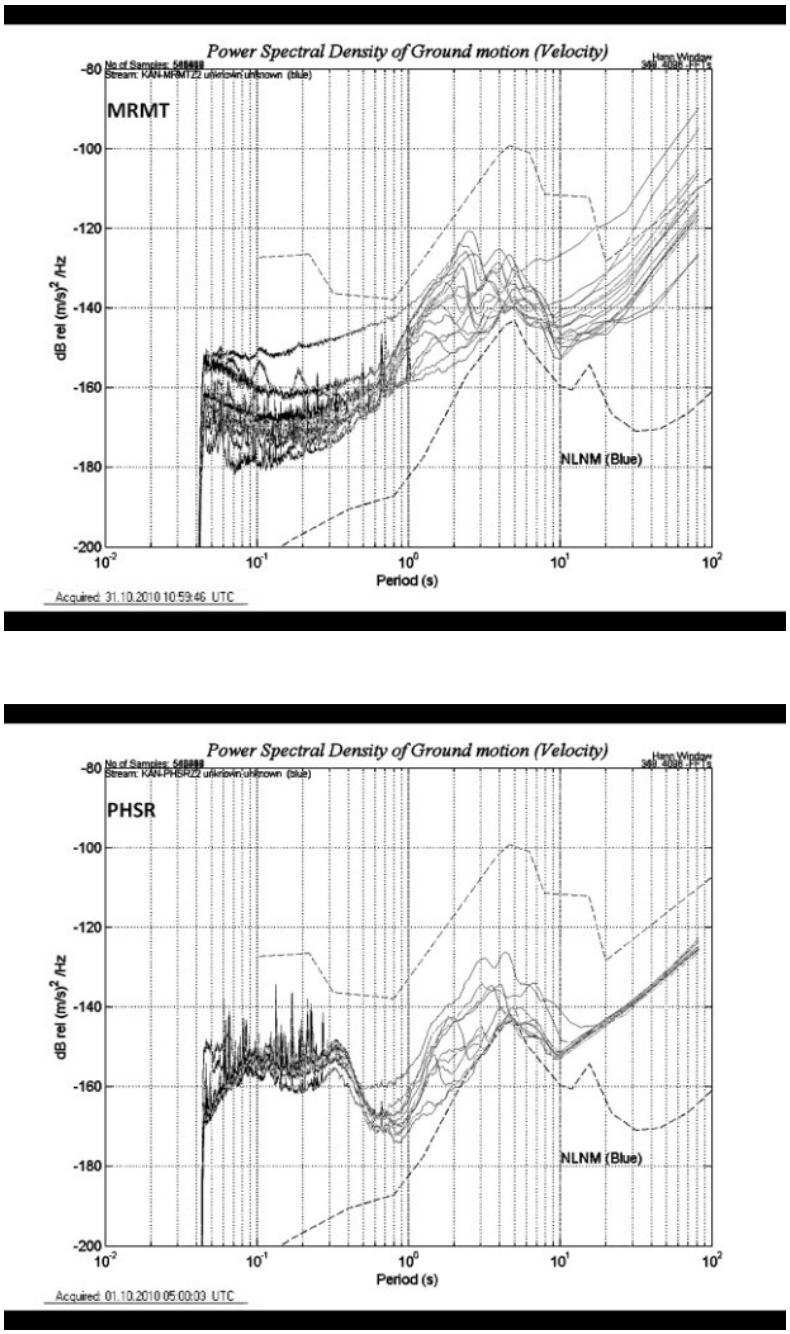

Figure B.42. PSDs of MRMT and PHSR

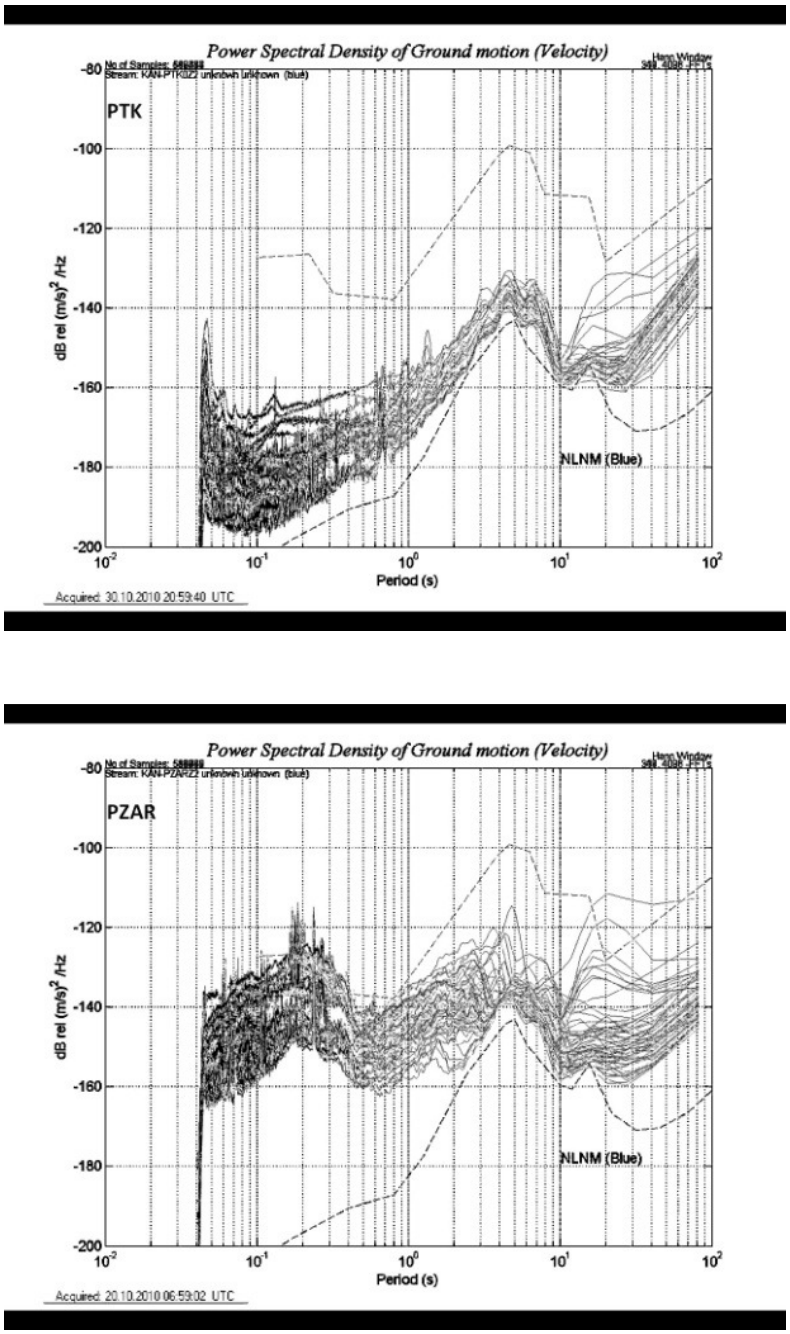

Figure B.43. PSDs of PTK and PZAR

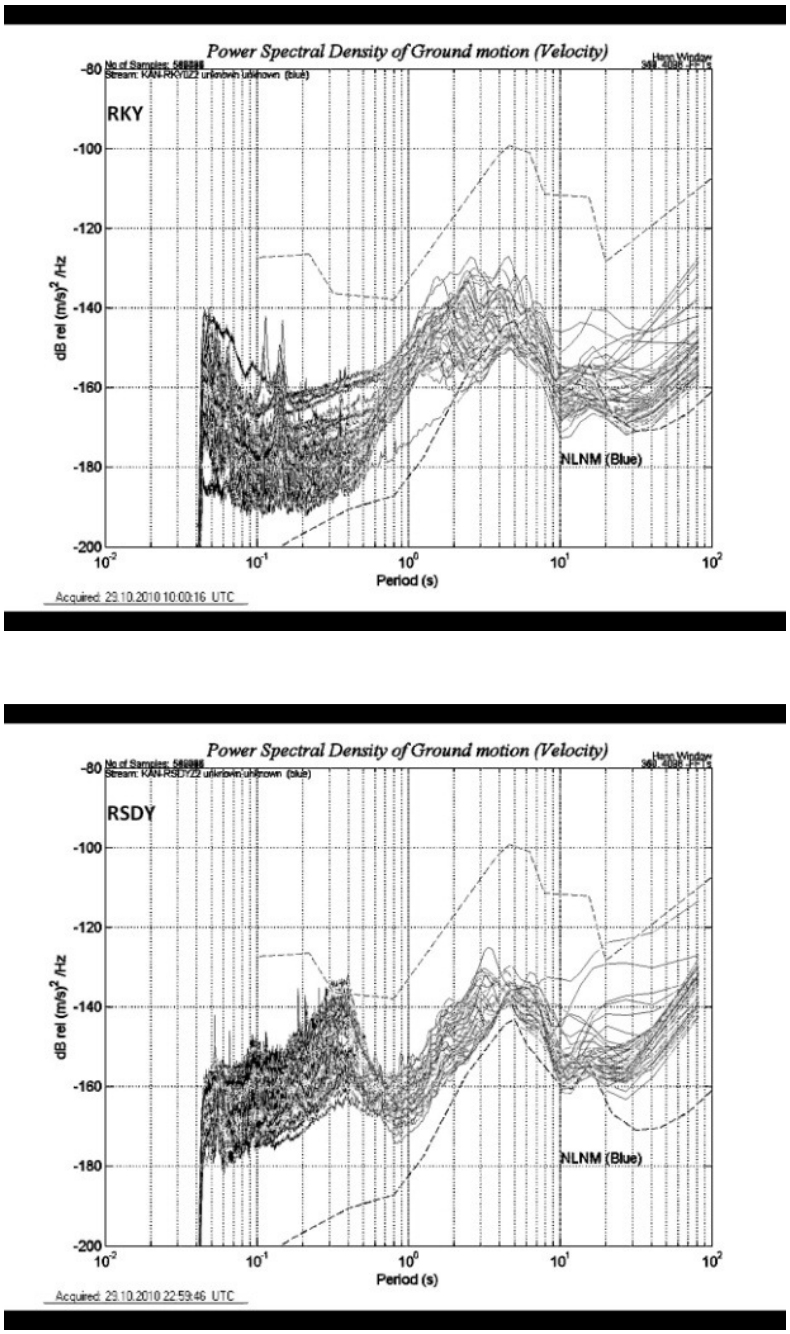

Figure B.44. PSDs of RKY and RSDY

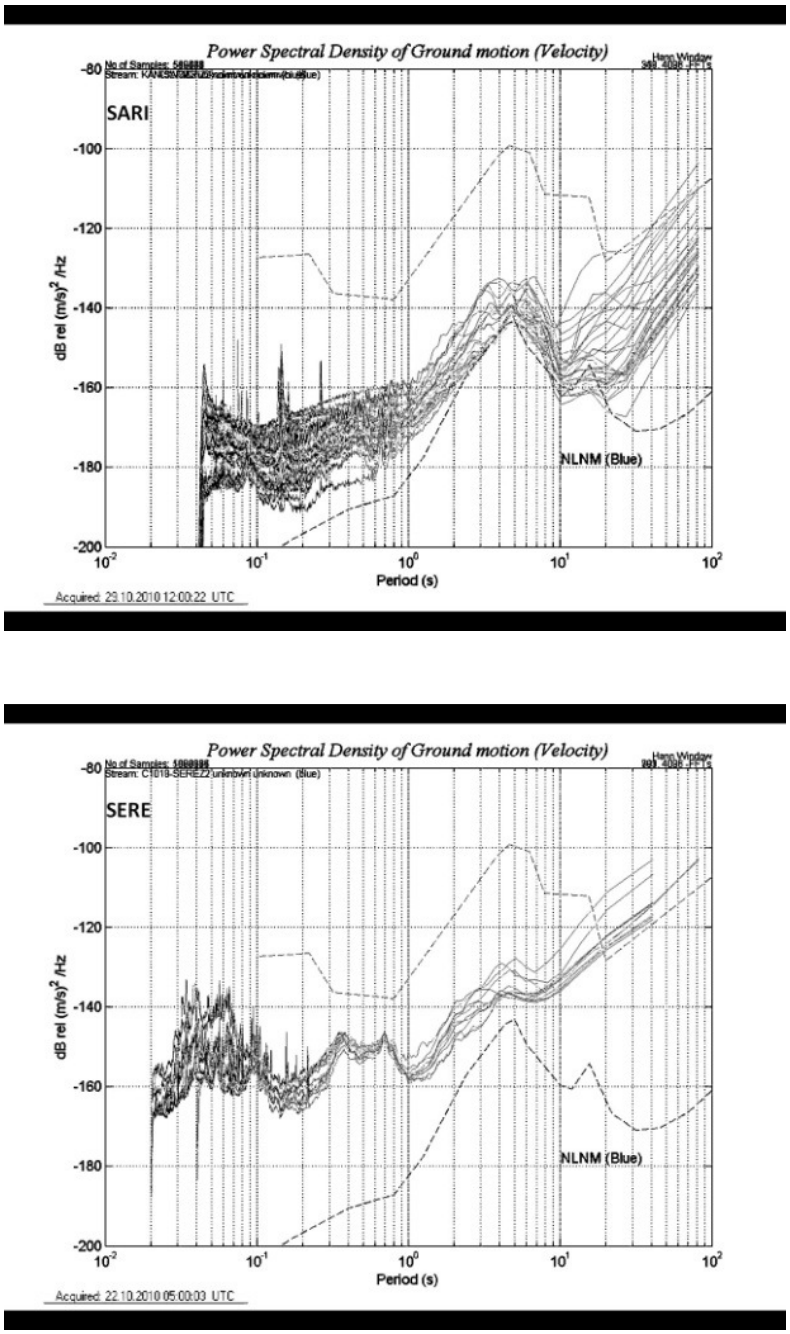

Figure B.45. PSDs of SARI and SERE

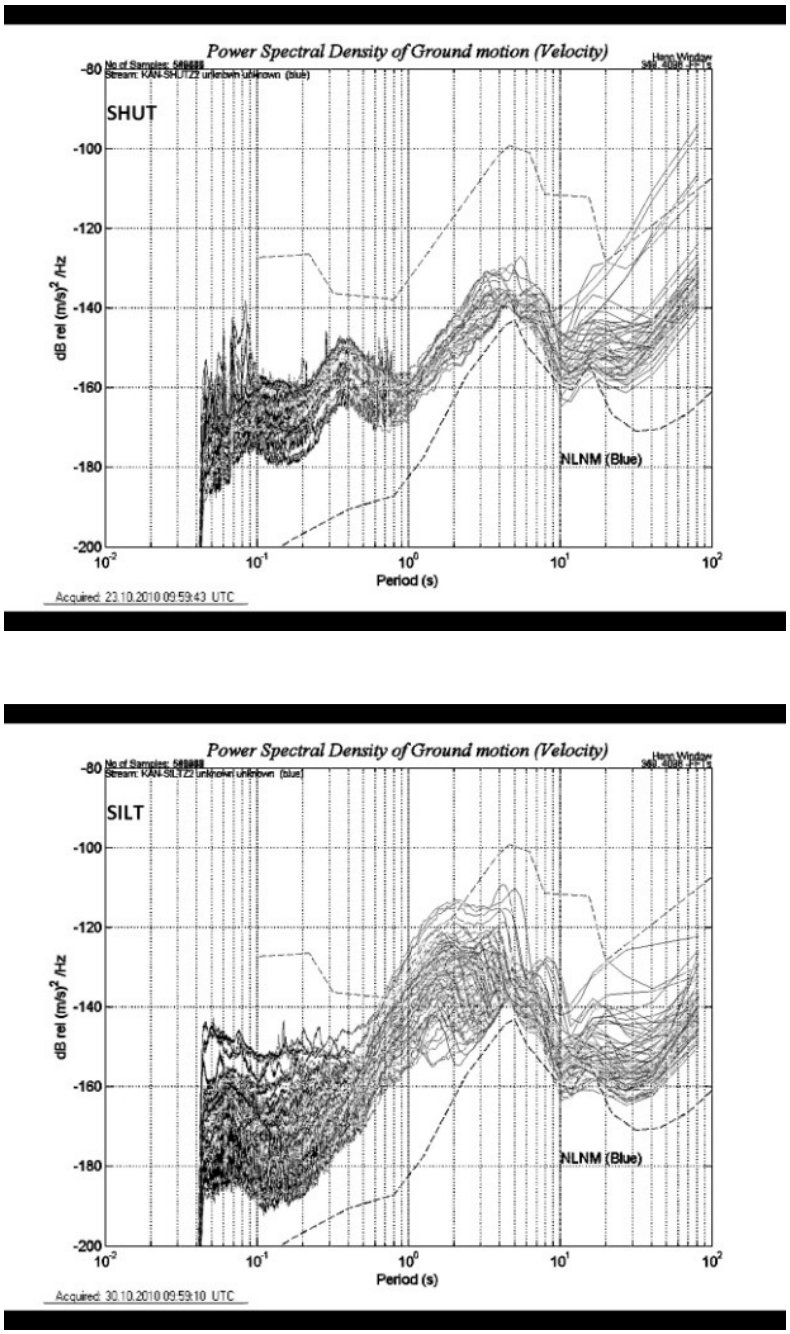

Figure B.46. PSDs of SHUT and SILT

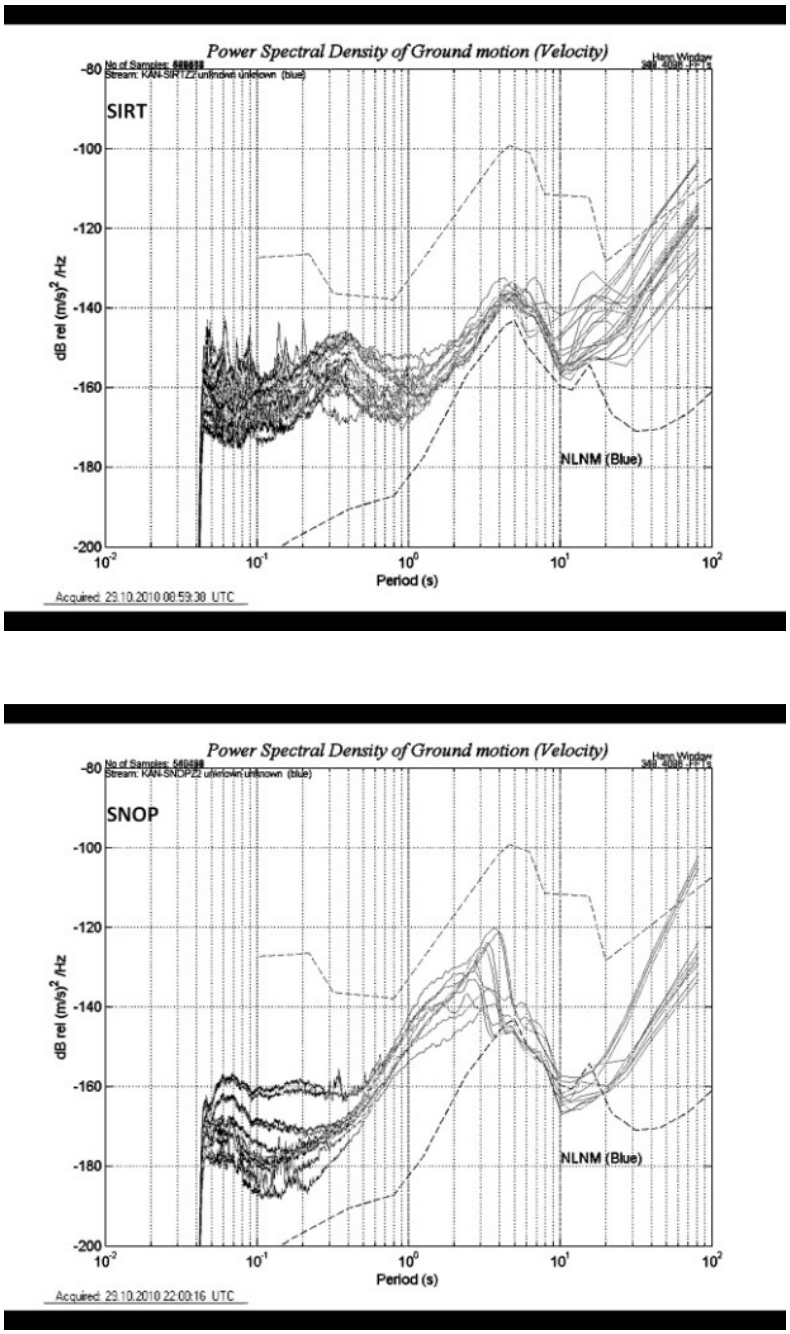

Figure B.47. PSDs of SIRT and SNOP

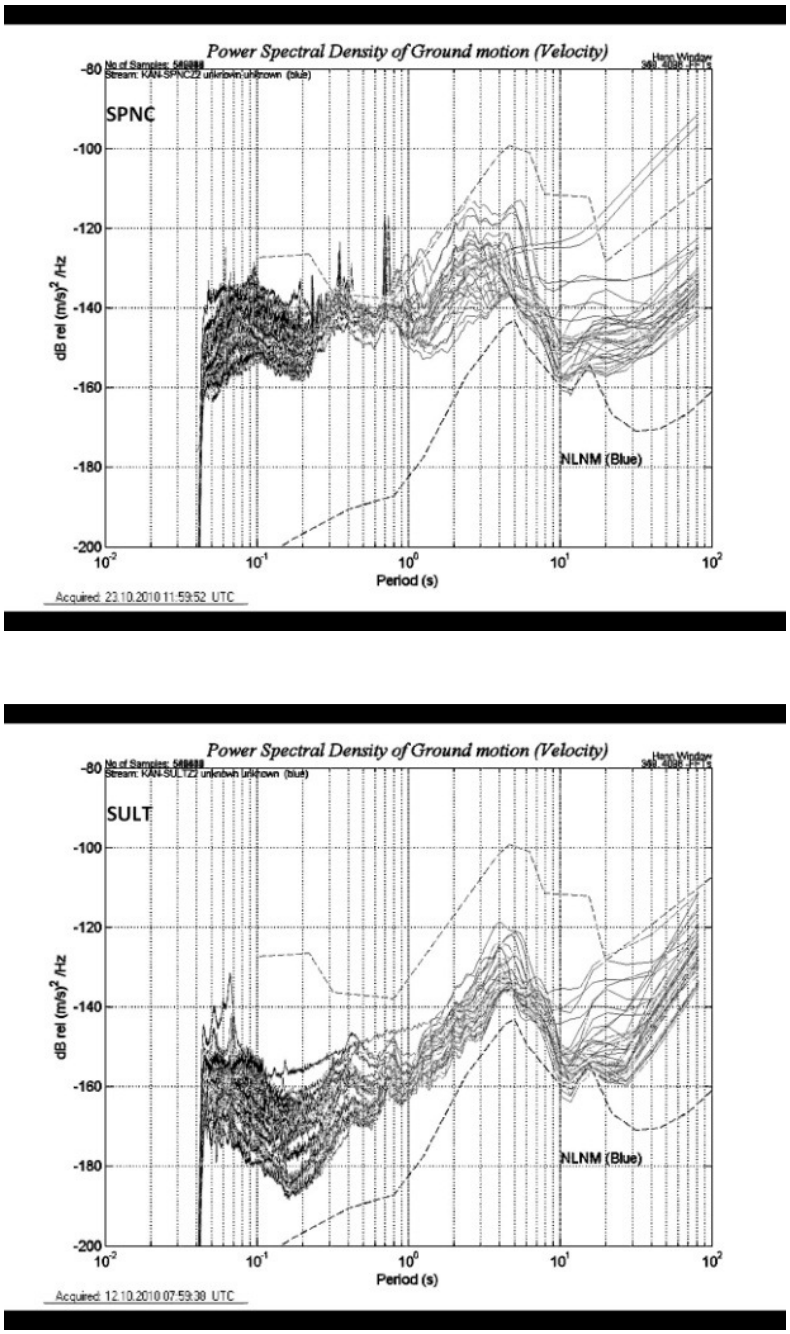

Figure B.48. PSDs of SPNC and SULT

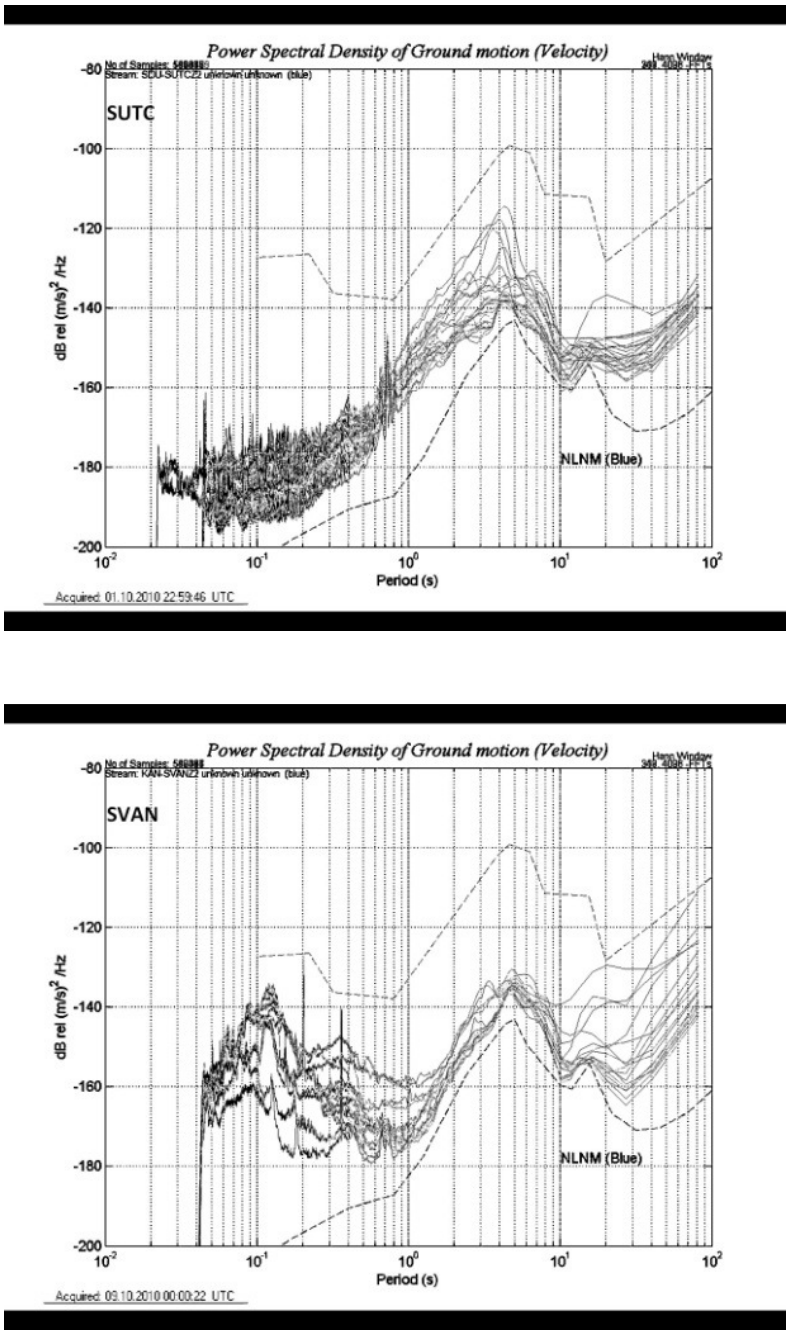

Figure B.49. PSDs of SUTC and SVAN

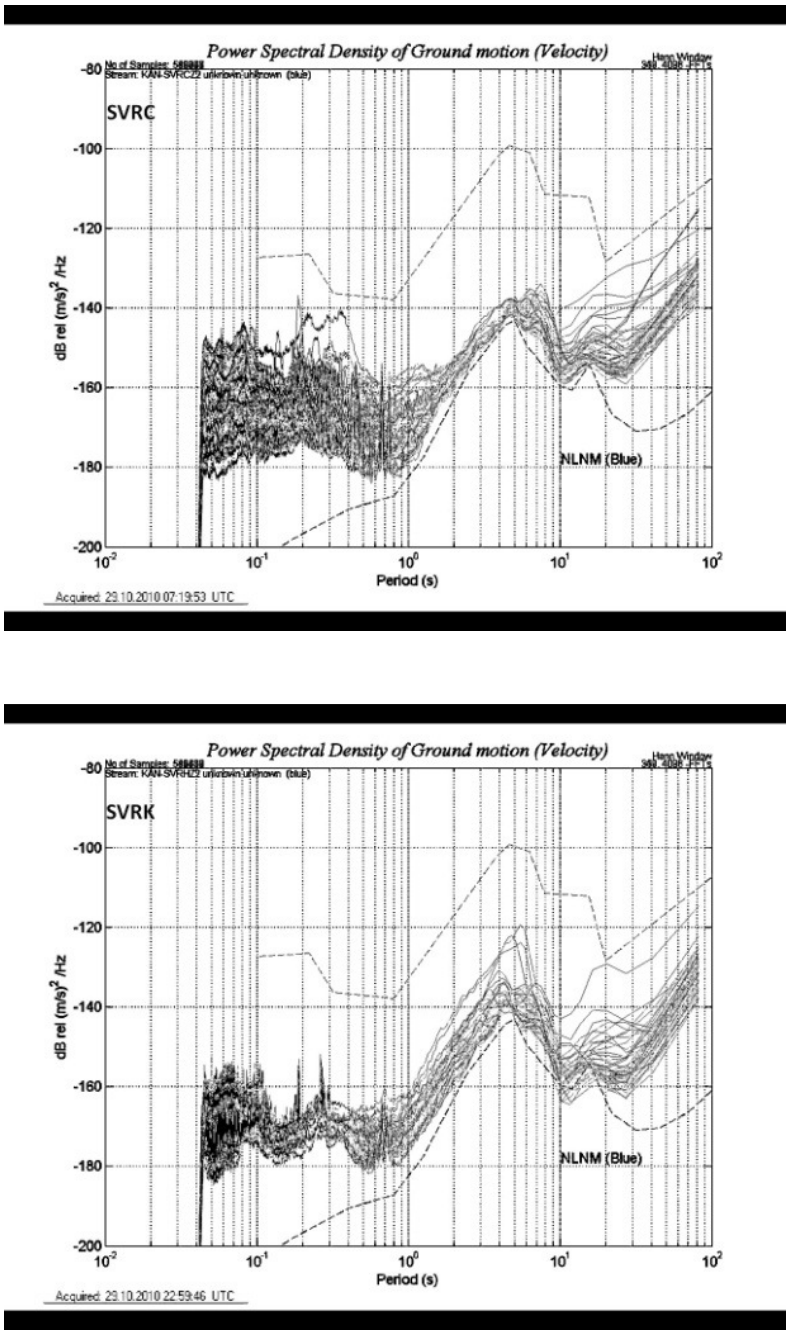

Figure B.50. PSDs of SVRC and SVRK

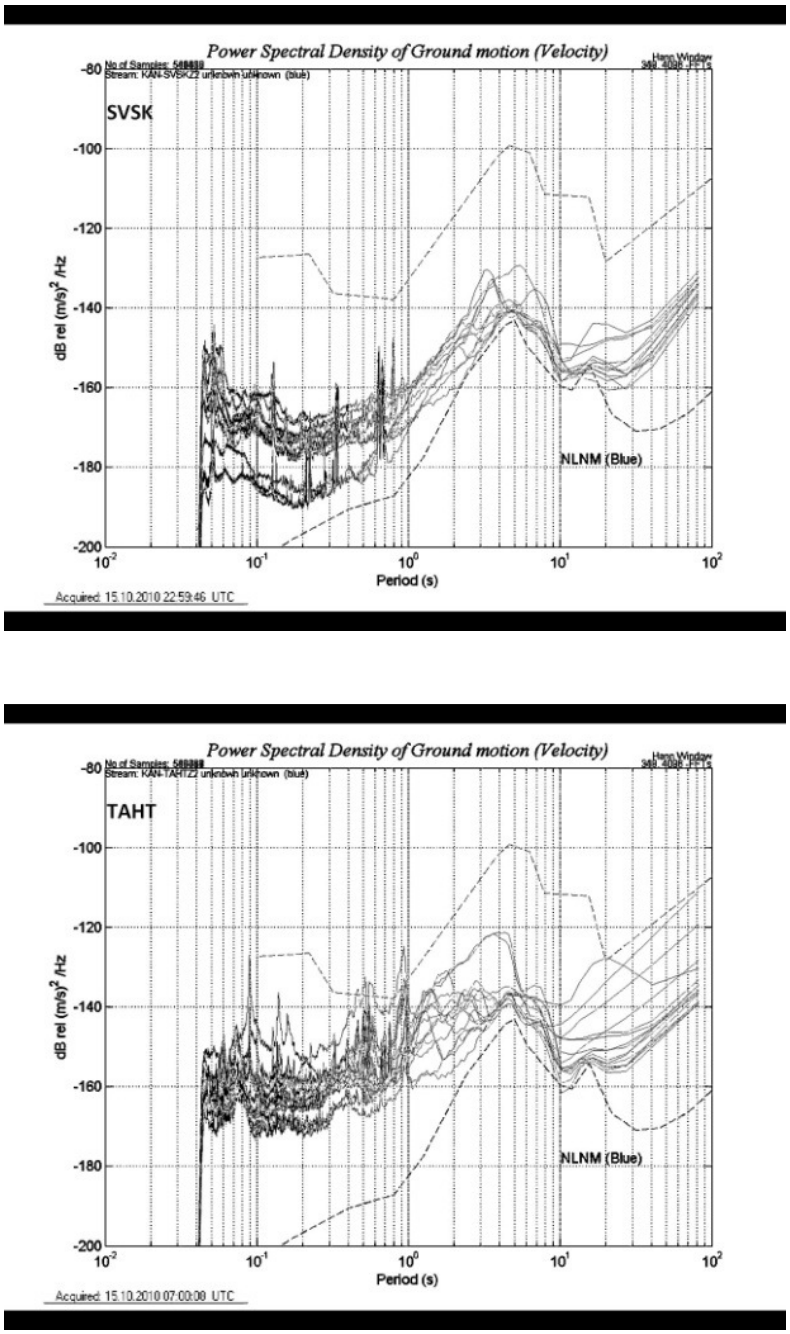

Figure B.51. PSDs of SVSK and TAHT

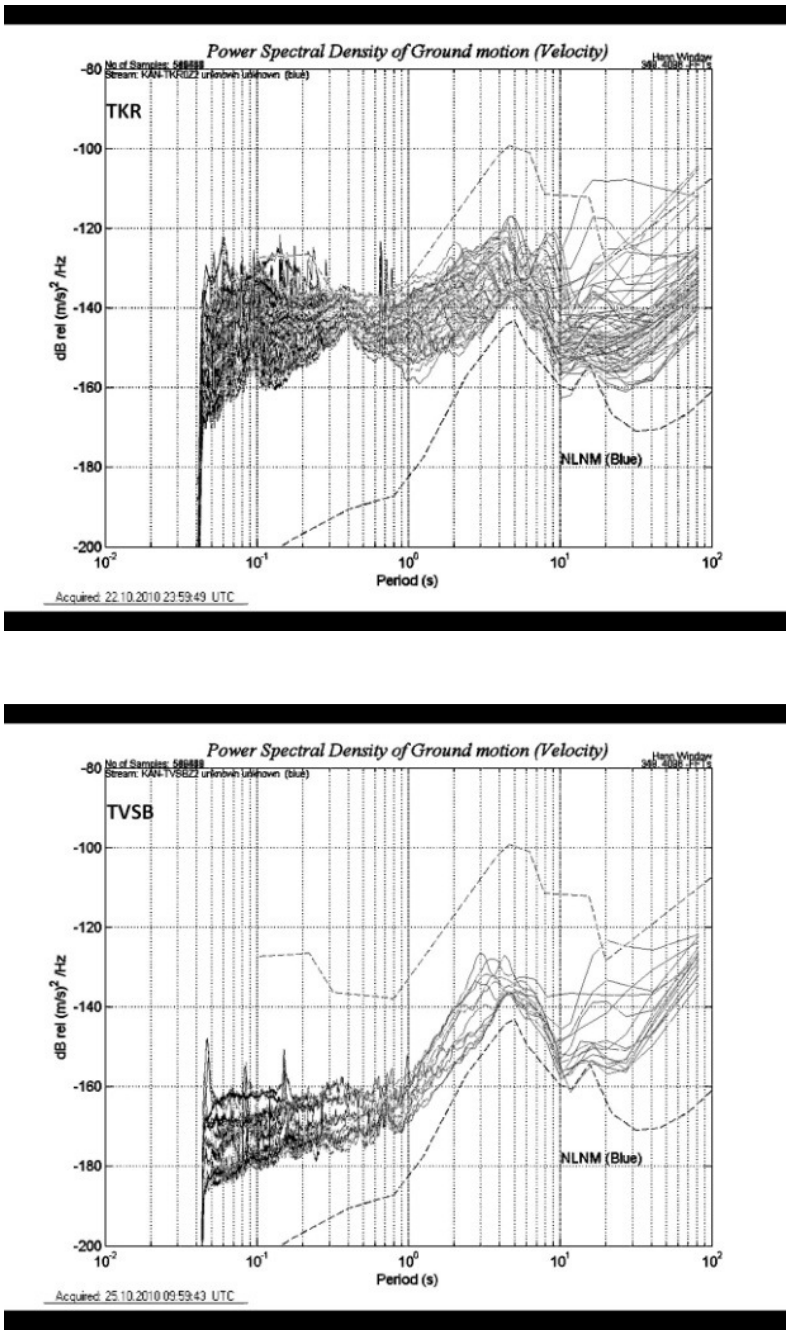

Figure B.52. PSDs of TKR and TVSB

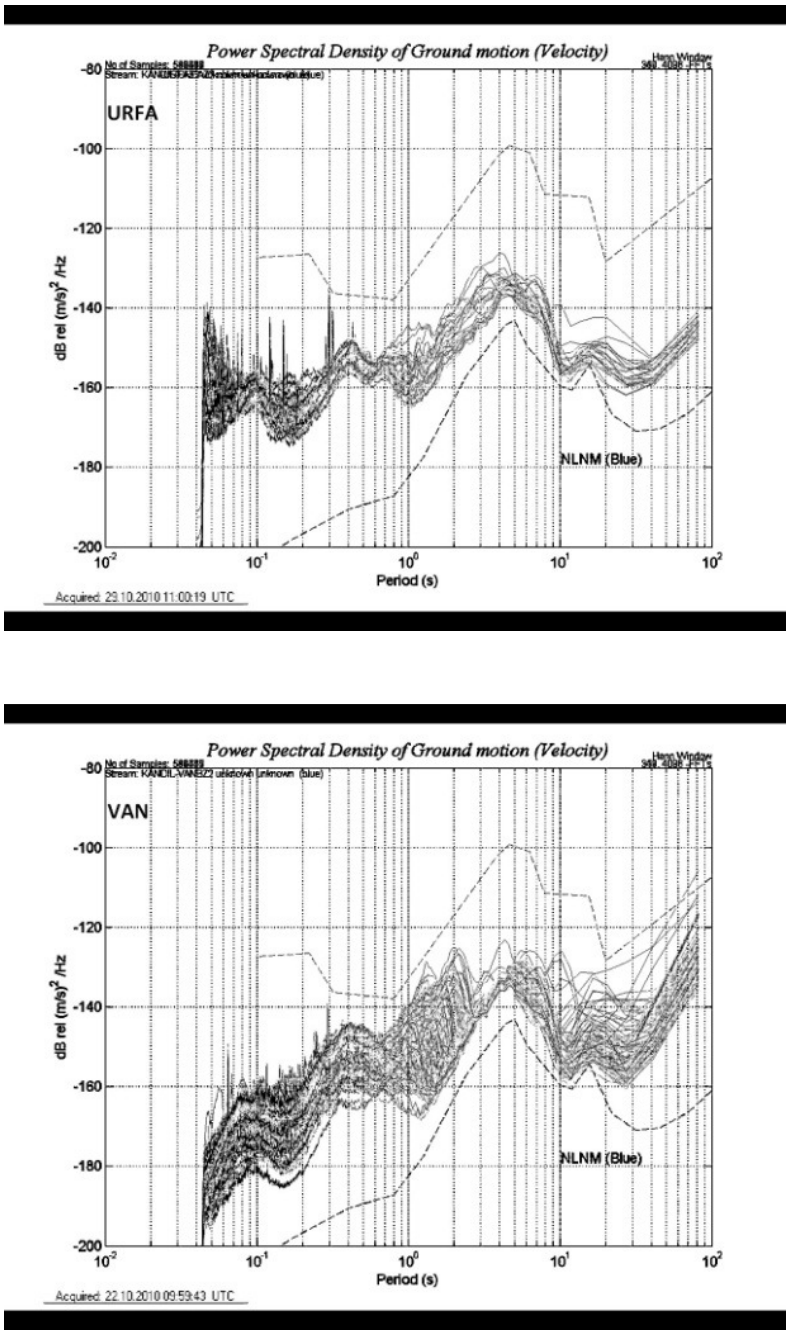

Figure B.53. PSDs of URFA and VAN

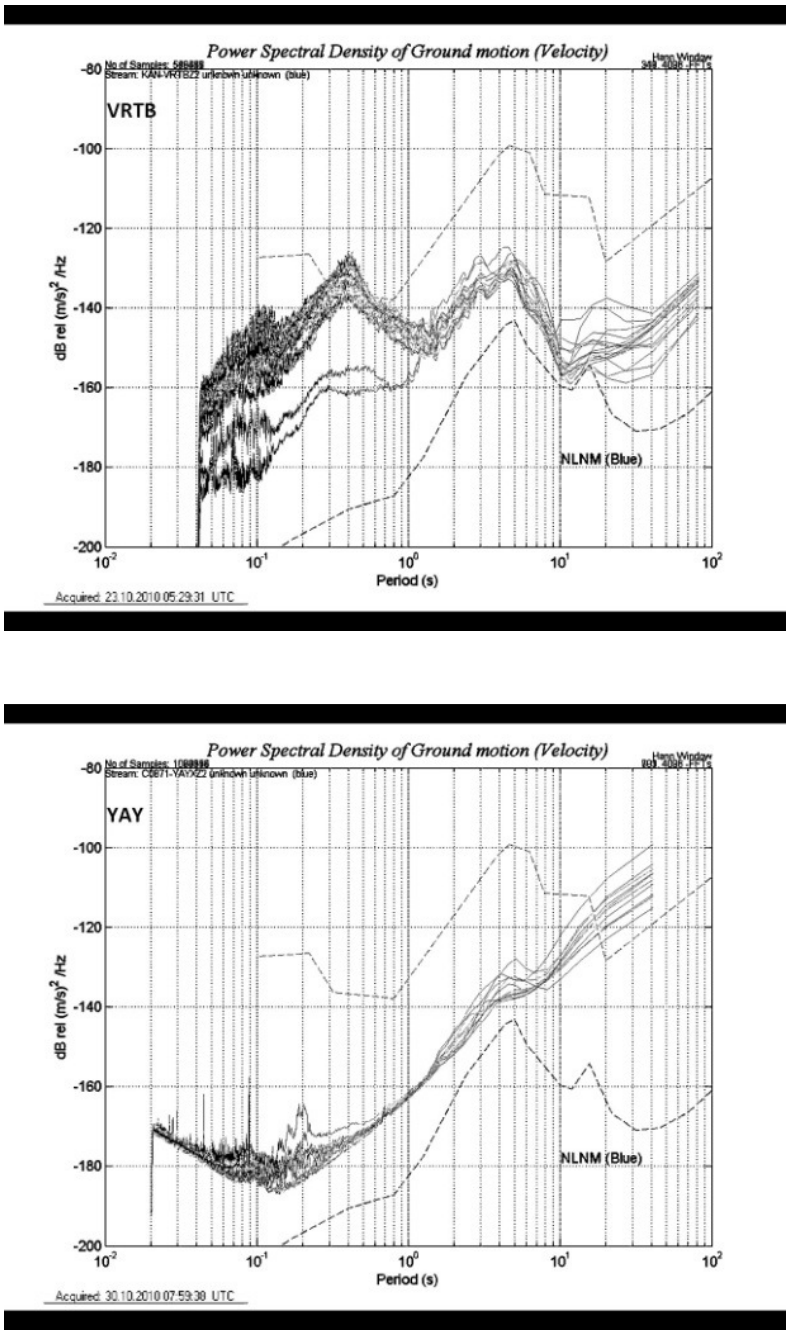

Figure B.54. PSDs of VRTB and YAY

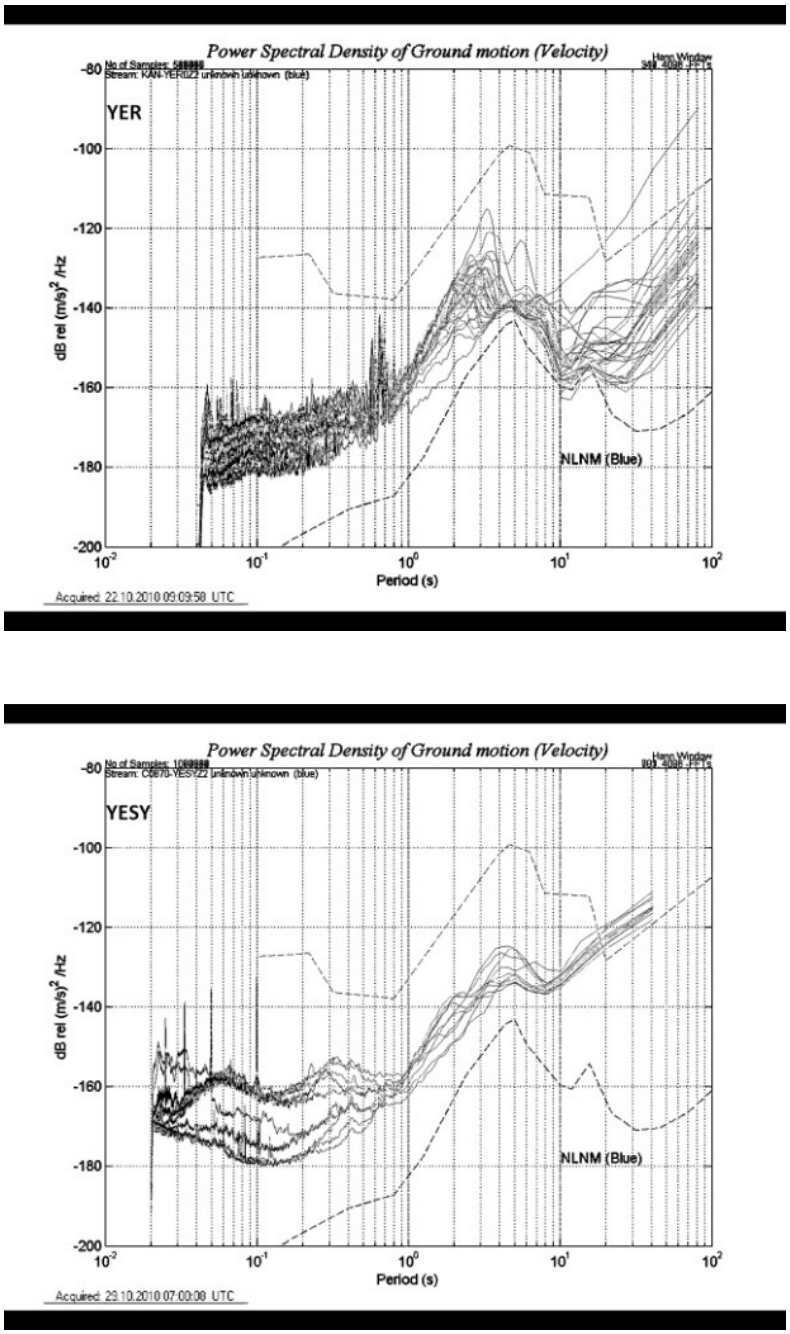

Figure B.55. PSDs of YER and YESY

APPENDIX C: STATIONS WITH MEAN PSD (1-12 Hz)

N (deg., min.)	E (deg., min.)	H (m)	mean PSD
40.2599	29.443	193	-140
39.2681	33.0422	1055	-137
39.3453	42.5952	1820	-145
39.0552	30.1103	1060	-115
36.5399	30.3923	20	-115
40.341	28.5196	320	-135
37.568	27.5345	1246	-142
39.384	27.528	120	-135
40.3935	40.141	1675	-145
41.267	41.3734	500	-150
37.2766	30.3526	859	-140
41.1086	28.4638	80	-135
38.2312	27.0252	150	-135
38.5948	40.4075	1180	-135
38.5113	35.5083	1380	-143
37.0373	27.1862	379	-133
41.576	34.0021	158	-135
40.3637	33.3718	815	-138
40.1211	29.5026	670	-142
37.0064	35.4487	100	-130
38.3494	32.5341	1086	-130
39.0864	43.5503	2094	-135
40.1071	34.3781	1292	-147
41.0774	27.4416	230	-115
41.1424	28.3043	47	-143
41.2856	28.1738	77	-125
37.1484	43.3646	1298	-135
36.4615	28.3823	548	-145
38.3427	37.2899	1080	-143
36.4374	27.3467	1100	-140
41.3898	35.1547	258	-143
39.0428	26.5432	49	-150
37.5719	40.0836	657	-132
40.2081	27.518	269	-131
41.5082	26.4462	209	-153
36.449	29.5451	1230	-145
40.4417	26.0918	100	-139

35.3175	34.1045	88	-123
40.4025	26.3079	41	-135
39.352	39.4332	1500	-147
40.9167	38.7273	430	-133
39.496	26.1955	48	-135
36.3812	29.0501	200	-137
40.1145	25.5392	130	-140
37.1033	37.1268	864	-138
40.2388	26.2845	129	-148
40.261	29.1134	220	-138
37.156	29.4983	1100	-125
40.028	27.4116	140	-142
38.2066	34.1416	1128	-140
40.2592	30.309	930	-138
36.5784	32.2916	1946	-132
40.493	29.4008	645	-135
36.1432	33.4111	120	-143
39.2712	38.3407	1280	-140
41.0394	29.0355	132	-135
37.1564	35.0328	366	-145
40.3691	43.0562	1747	-135
40.1593	28.2139	451	-140
41.1879	31.2658	410	-128
41.1518	29.0252	30	-130
37.3032	36.54	590	-143
37.5672	32.2163	550	-145
37.2883	35.4961	381	-145
40.2359	27.1786	75	-142
36.3439	35.225	53	-128
40.5922	39.46	171	-128
38.3087	28.3964	915	-145
39.0256	33.0014	1121	-133
41.0484	36.0278	649	-137
38.12	32.2189	1168	-145
40.2222	26.4556	230	-135
35.0671	32.506	152	-137
35.1699	33.3202	690	-140
39.5336	32.4584	902	-135
37.2762	40.268	1207	-135
40.2792	31.1287	1000	-138
40.2214	28.5304	110	-128
36.5206	34.3133	802	-135

37.1772	27.4659	500	-145
40.3635	27.3502	702	-138
41.3785	27.3143	263	-135
38.5354	39.2354	1835	-150
41.178	40.8988	80	-120
40.4125	27.1066	687	-147
40.2383	37.1964	550	-135
38.2443	36.2509	1673	-150
38.5678	33.33	1216	-131
38.3318	30.3306	1215	-140
41.0918	29.3858	100	-140
37.3006	42.2635	1038	-135
41.138	28.126	180	-145
42.0117	35.1241	180	-140
40.4116	30.185	190	-122
38.1193	33.3094	980	-142
38.0907	41.1191	650	-135
38.2265	39.1836	1680	-142
39.2682	31.3138	1000	-148
39.5505	36.5955	1630	-150
37.4765	30.9997	1300	-155
36.2254	36.1111	266	-135
40.5941	27.3214	140	-118
39.2698	29.2769	1090	-143
37.2646	38.4928	938	-133
38.357	43.2333	1227	-147
39.0962	41.2736	1500	-123
38.5632	33.4869	1142	-150
37.0817	28.1715	729	-145
37.0817	28.1715	729	-140
40.5114	29.0705	175	-127
36.4897	28.3919	10	-150
39.0266	29.2463	886	-115

APPENDIX D: ESTIMATION OF THE HYPOCENTRAL PARAMETERS

Travel times are the non-linear function of the stations, hypocenter coordinates and the velocity model. Hypocenter location can be defined by matrix system (D'Alessandro *et al.,* 2001).

$$\boldsymbol{d} = \boldsymbol{Gm} \tag{C1}$$

where $\boldsymbol{d}$ is the N components of data vector, $\boldsymbol{m}$ is the vector of the model parameters and $\boldsymbol{G}$ is the N x 4 matrix of the spatial derivatives of the travel times which are calculated at the hypocenter

$$\boldsymbol{G} = \begin{vmatrix} 1 & \frac{\partial T_1}{\partial x_0} & \frac{\partial T_1}{\partial y_0} & \frac{\partial T_1}{\partial z_0} \\ 1 & \frac{\partial T_2}{\partial x_0} & \frac{\partial T_2}{\partial y_0} & \frac{\partial T_2}{\partial z_0} \\ \vdots & \vdots & \vdots & \vdots \\ 1 & \frac{\partial T_N}{\partial x_0} & \frac{\partial T_N}{\partial y_0} & \frac{\partial T_N}{\partial z_0} \end{vmatrix} \tag{C2}$$

where $T_1, T_2, \ldots, T_N$ are the travel times used in the hypocenter location. The result of Equation (C1) needs the calculation of the generalized inverse matrix $\boldsymbol{G}^{-g}$. $\boldsymbol{G}$ is a Nx4 matrix and its iverse is calculated with the generalized inverse only for N=4. In general, N is greater than 4, so $\boldsymbol{G}^{-g}$ can be estimated in terms of least square through its SVD (Singular Value Decomposition) (D'Alessandro *et al.,* 2001).

$$\boldsymbol{G}^{-g} = \mathbf{V}\,\boldsymbol{\Lambda}^{-1}\,\mathbf{U}^{\mathbf{T}} \tag{C3}$$

where $\boldsymbol{\Lambda}$ is the diagonal matrix resolved by the square roots of the eigenvalues or singular values of $\boldsymbol{G}^T\,\boldsymbol{G}$, $\boldsymbol{V}$ which is the matrix resolved by the eigenvectors of $\boldsymbol{G}^T\,\boldsymbol{G}$ and $\boldsymbol{U}$ is the matrix resolved by the eigenvectors of $\boldsymbol{G}\,\boldsymbol{G}^T$. $\boldsymbol{R} = \boldsymbol{V}\,\boldsymbol{V}^T$ is the resolution matrix and its diagonal element imply the relative solutions of each of the parameters whereas the

elements of the matrix $\mathbf{D} = \mathbf{U}\ \mathbf{U}^{\mathbf{T}}$, which is the density matrix of information, indicate which of the observations have given more information about the problem. Representing finite number of digits results in unstable estimation of the generalized inverse matrix caused by small singular values. The stability solution is provided by the condition number *CN*, defined as

$$CN = \frac{\lambda_{max}}{\lambda_{min}} \qquad (C4)$$

where λ_{max} and λ_{min} are the greatest and the smallest singular values of matrix $\boldsymbol{G}$. When *CN* assumes values close to the correctness with which numbers are processed by the computer, the solution becomes unstable. If needed, TSVD (Truncated SVD) algorithm, where the smallest singular values are removed, can stabilize the solution in order to make *CN* adequately small. As soon as the inverse matrix $\boldsymbol{G}^{-g}$ has been calculated, the covariance matrix of the solution can be calculated by Equation (3.34) (D'Alessandro *et al.,* 2001).

REFERENCES

Aktar, M., H. Karabulut, 2004, Turkey National Seismic Network Design and Implementation, KOERI Report, January, http://www.koeri.boun.edu.tr/jeofizik/broadband /Turkiye_Ulusal_Sismik_Agi-Tasarim_Uygulama.pdf (in Turkish).

Anderson, J. G and S.E. Hugh, 1984, "A Model For the Shape of the Fourier Amplitude Spectrum of Acceleration at High Frequencies", *Bulletin of the Seismological Society of America,* Vol. 74, No. 5, pp. 1969-1993.

Bayrak, Y., S. Öztürk, G.C. Koravos, A. Leventakis, and T.M. Tsapanos, 2008, "Seismicity Assessment for the Different Regions in and Around Turkey", *Natural Hazards and Earth System Sciences,* pp. 109-122.

Bindi, D., S. Parolai, H. Grosser, C. Milkereit and S. Karakisa, 2006, "Crustal Attenuation Characteristics in Northwestern Turkey in the Range from 1 to 10 Hz", *Bulletin of the Seismological Society of America,* Vol. 96, No. 1, pp. 200-214.

Bormann, P., 2002, "IASPEI New Manual of Seismological Observatory Practise (NMSOP)", *GeoForschungsZentrum Potsdam,* Vol. 1, Chapter 4, pp. 1-24, ISBN 3-9808780-0-7.

Bormann, P., 2002, "IASPEI New Manual of Seismological Observatory Practise (NMSOP)", *GeoForschungsZentrum Potsdam,* Vol. 1, Chapter 8, pp. 1-9, ISBN 3-9808780-0-7.

Braile, L.W., 2009, "Seismic Monitoring", *The Geological Society of America,* pp. 229-244.

Brocher, T.M., 2005, “Empirical Relations Between Elastic Wavespeeds and Density in the Earth’s Crust”, *Bulletin of the Seismological Society of America,* Vol. 95, No. 6, pp. 2081-2092.

Brune, J.N., 1970, "Tectonic Stress and the Spectra of Seismic Shear Waves from Earthquakes", *Journal of Geophysical Research* , Vol. 75, 4997–5009.

D’Alessandro, A., D. Luzio, G. D’Anna, and G. Mangano, 2011, “Seismic Network Evaluation through Simulation: An Application to the Italian National Seismic Network”, *Bulletin of the Seismological Society of America,* Vol. 101.

Erdik, M., *History of KOERI,* http://www.koeri.boun.edu.tr/eng/topeng.htm

Gentili, S., M. Sugan, L. Peruzza, and D. Schorlemmer, 2011, “Probabilistic Completeness Assessment of the Past 30 Years of Seismic Monitoring in Northeastern Italy”, *Physics of the Earth and Platenery Interiors*, V. 186, No:1-2, pp. 81-96.

Guralp, C.M., *Guralp Seismological Systems*, http://www.guralp.com/products/3T/

Hanks, T.C., and H. Kanamori, 1979, “A Moment Magnitude Scale”, *Journal of Geophysics Research,* Vol. 84, pp. 2348-2350.

Hastie, T., R. Tibshirani, and J. Friedman, 2008, “The Elements of Statistical Learning: Data Mining, Inference, and Prediction”, *Second Edition, Series in Statistics, Springer, New York,* 764 pp.

Havskov, J., and G. Alguacil, 2004, *Instrumentation in Earthquake Seismology*, Springer Publisher, Vol. 22, pp. 77-85, ISBN-10 1-4020-2968-3.

Havskov, J., and L. Ottemöller, 2010, “Routine Data Processing in Earthquake Seismology”, *Springer, New York,* pp. 245-268, ISBN 978-90-481-8696-9.

Hempton, M.R., 1985, “Structure and Deformation History of Bitlis Suture Near Lake Hazar, Southeastern Turkey” *Bulletin of the Seismological Society of America,* Vol. 96, pp. 233-243.

Kalafat, D., C. Gürbüz, S.B. Üçer, 1987, “Batı Türkiye' de Kabuk ve Üst Manto Yapısının Araştırılması”, *Earthquake Research Bulletin*, No. 59, 43-64 (in Turkish).

Kalafat, D., “*Major Erathquakes Caused Loss and Damage between 1900-2004 in Turkey*”, http://www.koeri.boun.edu.tr/sismo/default.htm

Kalafat, D., “*Map of NEMC Earthquake Recording Stations*”, http://www.koeri.boun.edu .tr/sismo/default.htm

Kanamori, H., and D.L. Anderson, 1975, “Theoretical Basis of Some Empirical Relations in Seismology”, *Bulletin of the Seismological Society of America,* Vol. 65, pp. 1073-1095.

Karabulut, H., A. Kömeç Mutlu, D. Childs, D. Aksarı, M. Aktar, R. Yalgın, 2003, *The Broadband Digital Seismic Network Project,* KOERI Report, http://www.koeri.boun.edu. tr/jeofizik/broadband/index.htm

Kekovalı, K., S. Altuncu, *“Map of Seismic Activity of Turkey and Surrounding (2005-2011)”*, NEMC.

Kristekova, M., and I. Skacikova, 1997, “Detection Capability of Selected Seismic Stations in Central Europe”, *StudiaGeo s.r.o.,* 41, pp. 149-163.

Ludwig, W. J., J. E. Nafe, and C. L. Drake, 1970, *Seismic Refraction, in The Sea,* A. E. Maxwell (Editor), Vol. 4, Wiley-Interscience, New York, pp. 53–84.

Lay, T., and T.C. Wallace, 1995, *Modern Global Seismology,* Academic Press., pp. 521, ISBN 0-12-732870-X.

McCreery, C.S., F.K. Duennebier, and G.H. Sutton, 1993, "Correlation of Deep Ocean Noise (0.4-20 Hz) with Wind, and the Holu Spectrum a Worldwide Constant", *J. Acoust. Soc. Am.,* 93, pp. 2639-2648.

McKenzie, D.P., 1978, "Active Tectonics of the Alpine-Himalayan Belt: the Aegean Sea and Surrounding Regions", *Geophys. J. Royal Astron. Soc.*, 55, pp. 217–254.

McNamara, D.E., and R.P. Buland, 2003, "Ambient Noise Levels in the Continental United States", *USGS, Golden, CO*, http://geohazards.cr.usgs.gov/staffweb/mcnamara/PDFweb/McNamaraBuland.pdf

Özmen, B., M. Nurlu, 1997, "Some Information on Earthquake Zones Map", *UCTEA The Chamber of Geological Engineers Newsletters,* No. 99/2-3, pp. 32-35 (in Turkish).

Özmen, B., M. Nurlu, H. Güler, 1997, "Investigation of Earthquake Zones with Geographic Information System", http://www.deprem.gov.tr/sarbis/Shared/DepremHaritaLarı.aspx (in Turkish).

Papazachos, B. C. and P.E. Comninakis, 1971, "Geophysical and Tectonic Features of the Aegean arc", *J. Geophys. Res.,* 76, pp. 8517–8533.

Peterson, J., 1993, *Observations and Modeling of Seismic Background Noise,* USGS Open File Report, 93, 322.

Pinsky, V., Y. Gitterman, A. Shapira, M. Ergin, and C. Gürbüz, 2003, "Improvements in Monitoring of Small Regional Events Based On Ground Truth Data in Turkey and Israel", *25th Seismic Research Review - Nuclear Explosion Monitoring: Building the Knowledge Base,* No. DTRA01-00-C-0119, https://www.nemre.nnsa.doe.gov/prod/researchreview/2003/papers/03-09.pdf

Proakis, J.G. and D.G. Monalakis, 1996, "Digital Signal Processing", pp. 910-913, http://en.wikipedia.org/ wiki/Welch's_method

Rabinowitz, N., and D.M. Steinberg, 1990, "Optimal Configuration of A Seismographic Network: A Statistical Approach", *Bulletin of the Seismological Society of America,* Vol. 80, No. 1, pp. 187-196.

Rothman, R.L., R.J. Greenfield, and H.H. Hardy, 1974, "Errors in Hypocenter Location due to Velocity Anisotropy", *Bulletin of the Seismological Society of America,* Vol. 64, pp. 1993-1996.

Rydelek, P.A., I.S. Sacks, 1989, "Seismic Parameters for Engineering Applications Help", *Nature,* 337, pp. 251-253.

Satake, K., 1985, "Effects of Station Coverage on Moment Tensor Inversion", *Bulletin of the Seismological Society of America,* Vol. 75, No. 6, pp. 1657-1667.

Stutzmann, E., G. Roult and L. Astiz, 2000, "GEOSCOPE Station Noise Levels", *Bulletin of the Seismological Society of America,* Vol. 90, No. 3, pp. 690-701.

Sato, H., M. Fehler, and R. Wu, 2002, "Scattering and Attenuation in of Seismic Wave in the Litosphere", *in International Handbook of Earthquake & Seismology, Part A,* Lee, Kanamori, Jennings, and Kisslinger, ISBN 0124406521.

Schorlemmer, D., and J. Woessner, 2008, "Probability of Detecting an Earthquake", *Bulletin of the Seismological Society of America,* Vol. 98, No. 5, pp. 2103-2117.

Seggern, D.H., 2004, "Seismic Background Noise and Detection Threshold in the Southern Great Basin Digital Seismic Network", *Bulletin of the Seismological Society of America,* Vol. 94, No. 6, pp. 2280-2298.

Shepard, D., 1986, "A two-dimensional Interpolation Function for Irregularly-spaced Data", *In Proc. 1968 ACM National Conference,* pp. 517-524.

Şengör, A.M.C., 1979, "The North Anatolian Transform Fault: its Age, Offset and Tectonic Significance", *J. Geol. Soc., London*, 136, pp. 269–282.

Şengör, A.M.C., N. Görür, and F. Şaroğlu, 1985, "Strike-slip Faulting and Related Basin formation in zones of tectonic escape: Turkey as a case study, in: Strike-slip Faulting and Basin Formation", *edited by: Biddle K. T., Christie-Blick, N., Soc. Econ. Paleontol. Mineral. Sp. Pub.,* 37, pp. 227–264.

Tüysüz, O., 2005, "Neotectonics and Seismicity of Turkey", *ITU Eurasia Institute of Earth Sciences,* http://www.eies.itu.edu.tr/seminerler/Neotectonic.pdf

Uhrhammer, R.A., 1980, "Analysis of Small Seismographic Station Networks", *Bulletin of the Seismological Society of America,* Vol. 70, No. 4, pp. 1369-1379.

Webb, S.C., 2002, "Seismic Noise on Land and on the Sea Floor", *International Handbook of Earthquake and Engineering Seismology,* Vol. 81A, pp. 305-318, ISBN 0-12-440652-1.

Wilmore, P.L., 1979, "Manual of Seismological Observatory Practice", *World Data Center, Report SE-20.*

Wüster, J., F. Riviere, R. Crusem, J.L. Plantet, B. Massinon, and Y. Caristan, 2000, "GSETT-3: Evaluation of the Detection and Location Capabililties of an Experimental Global Seismic Monitoring System", *Bulletin of the Seismological Society of America,* Vol. 90, No. 1, pp. 166-186.

Zeiler, C., and A.A. Velasco, 2009, "Seismogram Picking Error from Analyst Review (SPEAR): Single-analyst and Institution Analysis, *Bulletin of the Seismological Society of America,* Vol. 99, No. 5, pp. 2759-2770.

Zoeppritz, K., 1919, "Erdbebenwellen VIII B, On the Reflection and Penetration of Seismic Waves Through Unstable Layers", *Goettinger Nachr.,* pp. 66-84.

REFERENCES NOT CITED

D'Alessandro, A., V. Karakostas, *Location performance of the Greek National Seismic Network: an evaluation by the SNES method,* Istituto Nazionale di Geofisica e Vulcanologia and Aristotle Universit of Thessaloniki, http://www.earth-prints.org/ bitstream/2122/6177/1/d0222_0251.pdf

Kutanis, M., *Seismicity of the world and Seismicity of Turkey,* http://www.kutanis. sakarya.edu.tr/lectures/eqe/PDF/6%20Seismicity%20of%20Turkey_general.pdf

McNamara, D., and R.I. Boaz, *Seismic Noise Analysis System: A Stand-Alone Software Package,* USGS Open File Report, pp. 1-16, 2005.

Oppenheim, A.V., Schafer, W. Ronald, *Digital Signal processing*, pp. 548-554, ISBN 0-13-214635-5, 1975.

Torre, T., and A.F. Sheehan, *Broadband Seismic Noise Analysis of the Himalayan Nepal Tibet Seismic Experiment,* Bulletin of the Seismological Society of America, Vol. 95, No. 3, pp. 1202-1208, 2005.

Welch, P.D., *The Use of Fast Fourier Transform for the Estimation of Power Spectra: A Method Based on Time Averaging Over Short, Modified Periodograms,* IEEE Transactions on Audio Electroacoustics, Vol. AU-15, pp. 70-73, 1967.

Wilson, D., J. Leon, R. Aster, J. Ni, J. Schlue, S. Grand, S. Semken, S. Baldridge, and W. Gao, *Broadband Seismic Background Noise ar Temporary Seismic Stations Observed on a Regional Scale in the Southwestern United States,* Bulletin of the Seismological Society of America, Vol. 92, No. 8, pp. 3335-3341, 2002.

Yalçınkaya, E., A. Pınar, M. Utkucu, A.İ. Kanlı, and Ö. Alptekin, *Site Selection For Istanbul University Broad-Band Seismic Station,* Istanbul University The Faculty of Engineering Department of Geophysical Engineering, Vol. 16, No. 1, pp. 11-21, 2003.